

Thomas Browder

UNIVERSITY OF CALIFORNIA
Santa Barbara

A Study of $D^0 - \overline{D^0}$ Mixing

A dissertation submitted in partial satisfaction
of the requirements for the degree of

Doctor of Philosophy

in

Physics

by

Thomas Earl Browder

Committee in charge:

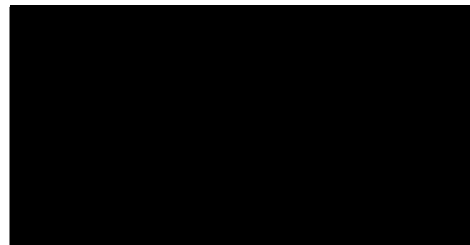
Professor Michael Witherell, Chairman

Professor Rollin Morrison

Professor Mark Srednicki

March 1988

The dissertation of
Thomas Earl Browder is approved:



Committee Chairman

March 1988

DEDICATION

To Maria
For her love and encouragement

ACKNOWLEDGEMENTS

I thank the members of the E691 collaboration:

from— University of California, Santa Barbara, California, USA
A. Bean, J.Duboscq, D.Hale, P.Karchin, S.McHugh, R.Morrison,
G.Punkar, J. Raab, M.Witherell

from— Carleton University, Ottawa, Ontario, Canada
P.Estabrooks, J.Pinfole, J.Sidhu

from— Centro Brasileiro de Pesquisas Fisicas, Rio de Janeiro, Brazil
J.Anjos, A.Santoro, M.Souza

from— University of Colorado, Boulder, Colorado, USA
L.Cremaldi, J.Elliott, M.Gibney, U.Nauenberg

from— Fermi National Accelerator Laboratory, Batavia, Illinois, USA
J.Appel, L.Chen, P.Mantsch, T.Nash, M.Purohit, K.Sliwa,
M.Sokoloff, W.Spalding, M.Streetman

from— National Research Council, Ottawa, Ontario, Canada
M.Losty

from— Universidade de São Paulo, São Paulo, Brazil
C.Escobar

from— University of Toronto, Toronto, Ontario, Canada
S.Bracker, G.Hartner, B.Kumar, G.Luste, J.Martin, S.Menary,

DEDICATION

Rollin Morrison—for his assistance in hardware work, his careful reading of early drafts of this thesis and his patient help in many other practical matters.

I am grateful to Dr. Chris Sliwa for his friendship and instruction during the grueling ACP conversion.

I also wish to thank Lucien Cremaldi, Jean Duboscq, Paul Karchin, and Greg Punkar for reading drafts of this thesis.

I apologize to those who I have not mentioned explicitly, but who have nevertheless contributed to this thesis.

CURRICULUM VITAE

Thomas E. Browder

Department of Physics
University of California
Santa Barbara, California 93106EDUCATION

1978 - 1982	University of Chicago
1982	Bachelor of Arts in Physics (with honors)
1982 - 1988	University of California (Santa Barbara)
1988	Ph. D. in Physics

PUBLICATIONS

- (1) Photoproduction of J/ψ Mesons on H, Be, Fe and Pb Targets
(M.D.Sokoloff et al., *Phys. Rev. Lett.* 57, (1986), 3003.)
- (2) Measurement of the D^+ and D^0 Lifetimes
(J.C.Anjos et al., *Phys. Rev. Lett.* 58, (1987), 311.)
- (3) Measurement of the D_s Lifetime
(J.C.Anjos et al., *Phys. Rev. Lett.* 58, (1987), 1818.)
- (4) Measurement of the Λ_c Lifetime
(J.C.Anjos et al., to appear in *Phys. Rev. Lett.*)
- (5) Measurement of D_s^+ Decays and Cabibbo-Suppressed D^+ decays
(J.C.Anjos et al., *Phys. Rev. Lett.* 60, (1988), 897.)
- (6) A Study of $D^0 - \bar{D}^0$ Mixing
(J.C.Anjos et al., to appear in *Phys. Rev. Lett.*)
- (7) Measurement of the $D^0, D^+,$ and D_s Lifetimes
(J.R.Raab et al., to appear in *Phys. Rev. D.*)

A Study of $D^0 - \overline{D^0}$ Mixing

by

Thomas Earl Browder

ABSTRACT

We present a study of D^0 mixing from Fermilab experiment E691, using events of the type $D^{*+} \rightarrow \pi^+ D^0$, with $D^0 \rightarrow K^+ \pi^-$ and $D^0 \rightarrow K^+ \pi^- \pi^+ \pi^-$. The charge of the bachelor pion tags the charm quantum number of the D^0 meson at production. The decay time is used to separate mixing from doubly Cabibbo-suppressed decays. We observe no evidence for mixing in either mode. Combining the results from the two decay modes, we find $r_M = 0.0005 \pm .0020$ or $r_M < .0037$ at the 90% confidence level, where r_M is the ratio of wrong sign decays from mixing to right sign decays. We also present limits on doubly Cabibbo suppressed decays and consider the effect of possible interference.

Contents

	page
List of Figures	x
List of Tables	xiii
1	1
1.1.1 On the Discovery of Charm	2
1.1.2 On Charmed Mesons	5
1.2 Theoretical Aspects of Mixing	9
1.2.1 General Formalism	9
1.2.2 The Time Dependence of Mixing	12
1.2.3 Standard Model Predictions	19
1.2.4 Predictions in Nonstandard Models	25
1.3 Experimental Limits and Hints	27
1.3.1 The Mark III Events	32
1.3.2 Same Sign Dimuons	38
1.4 On Charm Production and Detection	38
1.5 On Experiment E691	41
2	44
2.1 The Proton Beam and the Accelerator	45
2.2 The Electron and Photon Beams	47
2.3 The Target	51
3	53
3.1 Introduction	53
3.2.1 The Silicon Microstrip Detectors	53
3.2.2 Principle of Operation	54
3.2.3 Fabrication of Detectors	59
3.2.4 Characteristics of the E691 detectors	60
3.2.5 SMD Readout	64
3.2.6 SMD Monitoring	69
3.2.7 Leakage Currents, Radiation Damage, and Other Problems	73

3.2.8	Resolution and Other Figures of Merit	76
3.2.9	Additional Uses of the Vertex Detector	78
3.3	Magnets	79
3.4	Drift Chambers	81
3.5	Cerenkov counters	87
3.6	The SLIC and the Pair Plane	95
3.7	The Hadrometer	101
3.8	Muon Detection	102
3.9	The Trigger	104
3.10	Properties of Typical Events	109
4	The Reconstruction	111
4.1	Overview	111
4.2	The Problem	112
4.3	Solutions	112
4.4	Code Preparation	117
4.5	Conclusion	127
5	Analysis	129
5.1	Introduction	129
5.2	Stripping and Substripping	129
5.3	Final Selection Criteria	132
5.4	Backgrounds	135
5.5	Maximum Likelihood Fits	141
5.6	Determination of Upper Limits	162
5.7	Fits with Interference	165
5.8	Summary	169
6	Conclusions	171
6.1	Prospects for Future Experiments	175
Appendix I		177
Appendix II		182
References		186

List of Figures

Figure	page
1.1 Box diagrams for $K^0 - \overline{K^0}$ mixing	4
1.2 The SU(4) meson multiplets	6
1.3 The SU(4) baryon multiplets	7
1.4 Q value distribution for the decay $D^{*+} \rightarrow D^0\pi^+ \rightarrow (K^-\pi^+)\pi^+$	10
1.5 (a) Feynman graph for the Cabibbo favored decay $D^0 \rightarrow K^-\pi^+$	15
(b) Feynman graph for the doubly Cabibbo suppressed decay $D^0 \rightarrow K^+\pi^-$.	
1.6 Box diagrams for $D^0 - \overline{D^0}$ mixing	21
1.7 Long distance contributions to $D^0 - \overline{D^0}$ mixing	24
1.8 Higgs induced mixing	28
1.9 Illustration to accompany the intuitive argument for the suppression of DCSD in a p wave state.	35
1.10 (a) Opposite sign muons from neutrino induced charm production	39
(b) Same sign dimuons from gluon bremsstrahlung	
1.11 The spatial separation of the charm vertex from the point of production is used to measure the decay time in E691	42
2.1 Schematic of the Fermilab Tevatron	46
2.3 The Proton East beamline	49
3.1 The Tagged Photon Spectrometer	55
3.2 Charge distribution in a p-i-n junction	58
3.3 A cross section of a microstrip plane	61
3.4 The vertex detector and target configuration	70
3.5 A block diagram of the SMD readout system	71
3.6 Typical SMD beam profiles	74
3.7 The Cerenkov counters C1 and C2	92
3.8 (a) Mirror segmentation in C1 and C2	93
(b) Light paths in C1 and C2	
3.9 The SLIC	96
3.10 The Hadrometer	103
3.11 The Back Muon Wall	105

3.12	(a) A schematic of the E_T trigger (b) The gate for the E_T trigger	107
3.13	A typical online event display	110
4.1	Block diagram of an ACP system	116
4.2	The trivial parallelism of the high energy physics reconstruction problem.	118
4.3	Schematic of the code preparation procedure	123
4.4	Block diagram of the production system	126
4.5	Physical layout of the production environment	128
5.1	The SDZ cut and DIP cut	136
5.2	The isolation cut and RAT cut	137
5.3	Scatter plot of $M(K\pi)$ versus Q value with the selection $t > 0.22$ psec for (a) the right sign sample and (b) the wrong sign sample.	142
5.4	Scatter plot of $M(K\pi)$ versus Q value with the selection $t > 0.88$ psec for (a) the right sign sample and (b) the wrong sign sample.	143
5.5	Scatter plot of $M(K\pi\pi\pi)$ versus Q value with the selection $t > 0.22$ psec for (a) the right sign sample and (b) the wrong sign sample.	144
5.6	Scatter plot of $M(K\pi\pi\pi)$ versus Q value with the selection $t > 0.88$ psec for (a) the right sign sample and (b) the wrong sign sample.	145
5.7	Projections of figures 5.3(a) and 5.3(b) onto $K\pi$ mass with the restriction $4.3 \leq Q \leq 7.3$ MeV	146
5.8	Projections of figures 5.3(a) and 5.3(b) onto Q value with the restriction $1.845 \leq M(K\pi) \leq 1.885$ GeV	147
5.9	Projections of figures 5.4(a) and 5.4(b) onto $K\pi$ mass with the restriction $4.3 \leq Q \leq 7.3$ MeV	148
5.10	Projections of figures 5.4(a) and 5.4(b) onto Q value with the restriction $1.845 \leq M(K\pi) \leq 1.885$ GeV	149
5.11	Projections of figures 5.5(a) and 5.5(b) onto $K\pi\pi\pi$ mass with the restriction $4.3 \leq Q \leq 7.3$ MeV	150
5.12	Projections of figures 5.5(a) and 5.5(b) onto Q value with the restriction $1.845 \leq M(K\pi\pi\pi) \leq 1.885$ GeV	151
5.13	Projections of figures 5.6(a) and 5.6(b) onto $K\pi\pi\pi$ mass with the restriction $4.3 \leq Q \leq 7.3$ MeV	152
5.14	Projections of figures 5.6(a) and 5.6(b) onto Q value with the restriction $1.845 \leq M(K\pi\pi\pi) \leq 1.885$ GeV	153
5.15	(a) Mass distribution for the $D^0 \rightarrow K^-\pi^+$ mode with the correct particle assignments (b) Mass distribution with the kaon and pion assignments inverted	154

5.16	(a) Mass distribution for the $D^0 \rightarrow K^-\pi^+\pi^-\pi^+$ mode with the correct particle assignments (b) Mass distribution with the kaon and pion assignments inverted	155
5.17	(a) $\Delta\Gamma\rho < 0$, maximal destructive interference with a large DCSD amplitude (b) $\Delta\Gamma\rho > 0$, maximal constructive interference with a large DCSD amplitude	166

List of Tables

Table	page
1.1 Charmed Meson Properties	5
1.2 Limits on Mixing	37
3.1 Properties of Semiconductors	56
3.2 Properties of the E691 SMDs	63
3.3 Properties of the E691 Magnets	80
3.4 Properties of the E691 Drift Chamber System	84
3.5 Threshold Momenta for the E691 Cerenkov Counters	88
3.6 Properties of the E691 Čerenkov counters	89
3.7 Detailed Properties of the SLIC	97
3.8 Detailed Properties of the Pairplane Counters	100
3.9 Detailed Properties of the Hadrometer	102
4.1 Computing Intensive Experiments	113
5.1 Possible contributions to the low mass right sign D^* background	139
5.2 Results of a maximum likelihood fit to the right sign $K\pi$ mode	160
5.3 Results of a maximum likelihood fit to the wrong sign $K\pi$ mode	160
5.4 Results of a maximum likelihood fit to the right sign $K\pi\pi\pi$ mode	162
5.5 Results of a maximum likelihood fit to the wrong sign $K\pi\pi\pi\pi$ mode	162
5.6 Limits on mixing in the case of interference for the $K\pi$ mode.	168
5.7 Limits on mixing in the case of interference for the $K\pi\pi\pi$ mode.	168
6.1 Limits on rare D meson decays	174
A.1 Cuts used in the $K\pi$ strip	178
A.2 Cuts used in the $K\pi$ substrip	178
A.3 Cuts used in the $K\pi\pi\pi$ substrip	179
A.4 Cuts used in the $K\pi$ analysis job	180
A.5 Cuts used in the $K\pi\pi\pi$ analysis job	181

1

Introduction

The Standard model, the theoretical synthesis characterized by the gauge group $G = SU(3) \times SU(2) \times U(1)$ can explain the vast majority of experimental data on the strong and weak interactions. For instance, from the value of G_F , the weak coupling constant, the mass scale of the gauge bosons which mediate the electroweak interaction can be roughly deduced (~ 90 GeV). These gauge bosons were subsequently observed in 1983 at the CERN collider by UA1 and UA2. The gluonic degrees of freedom of $SU(3)$ were beautifully manifested by the 3-jet events observed at PETRA and by the measured width of the neutral pion. Despite these and many other successes, the Standard model is inelegant (it is characterized by 17 free parameters) and leaves many questions unanswered; for instance, what is the origin of fermion masses, couplings and CP violation ? It is the task of the experimentalist to seek answers to these questions by the detailed study of rare physical processes. This thesis will describe a high sensitivity search for $D^0 - \overline{D^0}$ mixing, one such process which provides an opportunity to test the Standard Model and constrain those theories which go beyond the Standard Model.

1.1.1 On the discovery of Charm

Historically, the importance of rare decays in the development of new physics is evident. Recall that the stringent upper limit on the decay $K_L \rightarrow \mu^+ \mu^-$ was one of the original motivations for postulating the existence of the charm quark. To understand this, consider the weak Lagrangian in the 3 quark model with one isospin doublet :

$$\psi_1 = \begin{pmatrix} u \\ d_c \end{pmatrix}$$

(where $d_c = \cos \theta_c d + \sin \theta_c s$) and three right handed singlets s_r, u_r, d_r . The neutral part of the Lagrangian will take the form: $\psi_1 \bar{\psi}_1 = u \bar{u} + d \bar{d} \cos^2 \theta_c + s \bar{s} \sin^2 \theta_c + d \bar{s} \cos \theta_c \sin \theta_c + s \bar{d} \cos \theta_c \sin \theta_c$. Thus we expect decays in which d and \bar{s} quarks annihilate. Moreover, the branching ratio for such modes should be comparable to $\text{BR}(K^+ \rightarrow \mu^+ \nu) = 63\%$, so one would expect copious dilepton decays of the K_L . In fact, $\text{BR}(K_L \rightarrow \mu^+ \mu^-) = 9 \times 10^{-9}$ and $\text{BR}(K_L \rightarrow e^+ e^-) < 2.0 \times 10^{-7}$. To suppress such "strangeness changing neutral currents", Glashow, Iliopoulos, and Maiani [Gl70] proposed a modified structure for the weak interaction with two weak doublets. The second doublet takes the form

$$\psi_2 = \begin{pmatrix} c \\ s_d \end{pmatrix}$$

where the upper member is the hypothetical charm quark and $s_d = \cos \theta_c s - \sin \theta_c d$. The neutral part of the Lagrangian is then given by:

$$\begin{aligned} \psi_1 \bar{\psi}_1 + \psi_2 \bar{\psi}_2 &= u \bar{u} + d \bar{d} + s \bar{s} \\ &+ s \bar{d} \sin \theta_c \cos \theta_c + d \bar{s} \sin \theta_c \cos \theta_c \\ &- s \bar{s} \sin \theta_c \cos \theta_c - d \bar{d} \sin \theta_c \cos \theta_c. \end{aligned}$$

Miraculously, the terms proportional to $s\bar{d}$ and $d\bar{s}$ have cancelled. In the limit where the s and d quark masses are equal, this cancellation is exact.

The strength of mixing in the $K^0 - \bar{K}^0$ system provided an additional constraint on this domain of new physics. By measuring the time dependence of wrong sign K^0 decays, it was possible to extract the numerical value of $\Delta M_K = M_L - M_S = \text{Re}\langle K^0 | H_W (\Delta S = 2) | \bar{K}^0 \rangle$. In the Standard Model, the principal contribution to ΔM comes from the box diagram with two virtual W's emitted, as shown in Figure 1.1.

In the absence of the charm quark, the magnitude of ΔM is proportional to M_W^2 :

$$\Delta M_K \cong \frac{G_F^2}{4\pi^2} (M_W^2) \cos \theta_c^2 \sin \theta_c^2 f_K^2$$

where M_W is the mass of W boson, f_K (~ 150 MeV) is the measured kaon decay constant. Using the known values of G_F , f_K , and a reasonable estimate for M_W , ΔM_K was predicted to be 0.985×10^{-8} MeV, four orders of magnitude larger than its observed value (3.521×10^{-12} MeV).

In the four quark model, one can show that,

$$\Delta M_K \cong \frac{G_F^2}{4\pi^2} (m_c^2 - m_u^2) \cos \theta_c^2 \sin \theta_c^2 f_K^2$$

Using the measured value of ΔM , Gaillard, Lee, and Rosner [Ga75] were able to estimate the value of $m_c \sim 1.4$ GeV. In 1973, this prediction was confirmed when the J/ψ meson, a narrow bound state of c and \bar{c} quarks, was observed independently by collaborations at SPEAR and Brookhaven.

By extending the known SU(3) symmetry of the (u,d,s) quarks to an

Contributions to Δm_k

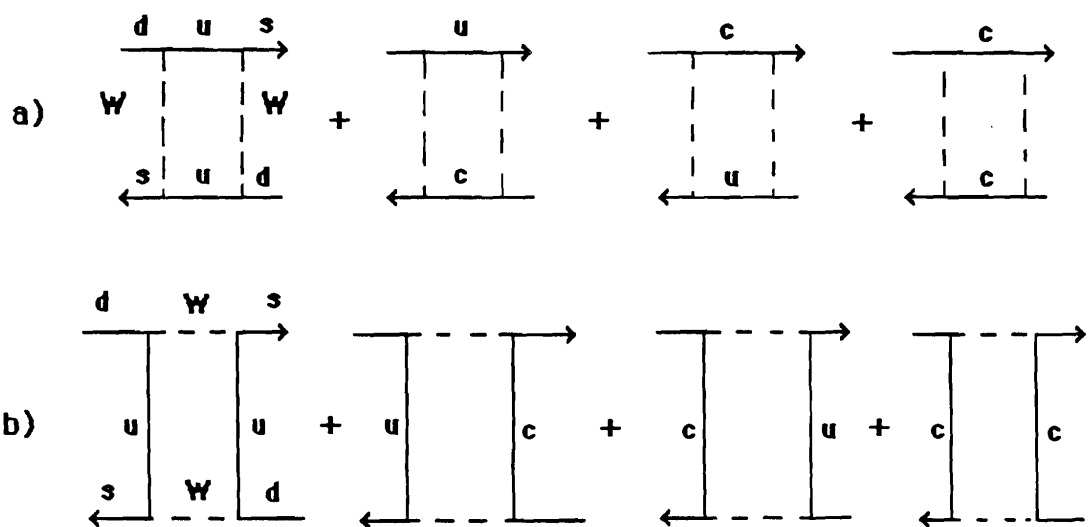


Figure 1.1 Box diagrams for $K^0 - \bar{K}^0$ mixing

approximate SU(4) symmetry and decomposing the direct products of the representations $\bar{4} \times 4$ and $4 \times 4 \times 4$ as direct sums of irreducible representations, Gaillard et al. were able to predict the spectrums of meson and baryon states containing charmed quarks.

1.1.2 On Charmed Mesons

In the four quark model the charmed mesons with the lowest mass, which therefore decay weakly, are the pseudoscalar particles: the D^0 , D^+ , and D_s^+ mesons. They have been observed. Their masses, quark content, quantum numbers, and lifetimes as determined by experiment E691 [Ra87],[Ra88] are given in Table 1.1.

Table 1.1 Charmed Meson Properties

Meson	Quark Content	Mass (in MeV)	τ (in sec)
D^0	$c\bar{u}$	1864.6 ± 0.6	$4.22 \pm .013 \times 10^{-13} *$
D^+	$c\bar{d}$	1869.3 ± 0.6	$1.09 \pm .039 \times 10^{-12} *$
D_s^+	$c\bar{s}$	$1968.5 \pm 0.8^*$	$4.7 \pm .045 \times 10^{-13} *$

* These are the measured values from experiment E691

The three pseudoscalar mesons are accompanied by vector partners the $(D^{*0}, D^{*+}, D_s^{*+})$ mesons. The masses of both types of states are roughly given by the sum of their quark constituent masses. However, $m(D^{*+}) > m(D^+)$ despite their identical quark content. The mass differ-

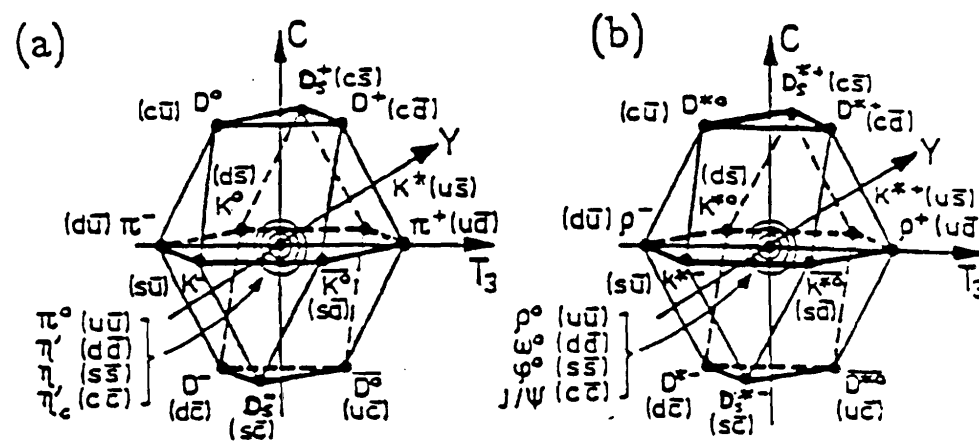


Figure 1.2 The multiplets for the (a) pseudoscalars (b) vector mesons.

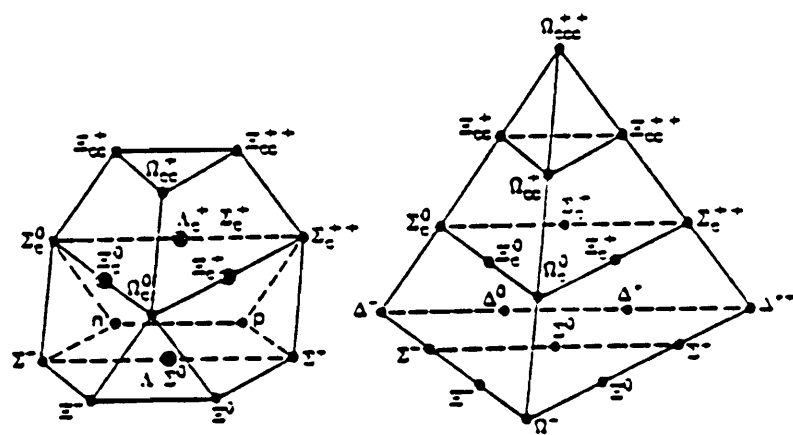


Figure 1.3 The baryon multiplets (a) spin $\frac{1}{2}$ (b) spin $\frac{3}{2}$.

ence between the vector and scalar states which are in the same orbital wave function is due to the quark spin-spin hyperfine interaction. This effect is the QCD analogue of the hyperfine splitting which occurs in the hydrogen atom or positronium. Here the energy splitting between the 3S_1 and 1S_0 levels is given by the scalar product of the effective magnetic moments of the constituents [Ha86]:

$$\Delta E_{hf} = \frac{-2}{3} \vec{\mu}_1 \cdot \vec{\mu}_2 |\psi(0)|^2$$

If the effective magnetic moments are expressed in terms of the quark masses: $\vec{\mu}_i = e_i \vec{s}_i / 2m_i$, and the effective coupling $e_1 \cdot e_2 = -e^2 = -4\pi\alpha_s$, then

$$\Delta E_{hf} = 2\pi \frac{\alpha_s}{3} \frac{\vec{s}_1 \cdot \vec{s}_2}{m_1 m_2} |\psi(0)|^2$$

For spin 1/2 quarks, $\vec{s}_1 \cdot \vec{s}_2 = -3/4$ for $S = 0$ and $\vec{s}_1 \cdot \vec{s}_2 = 1/4$ for $S = 1$ (here $S = s_1 + s_2$ the total spin). Thus $m(D^0) = m(c) + m(u) - \frac{3a}{m_c m_u}$ and $m(D^{*+}) = m(c) + m(d) + \frac{a}{m_c m_d}$ with $a = 2\pi\alpha_s/12 |\psi(0)|^2$. Using the well measured $K^* - K$ mass difference, and $m^2(K^*) - m^2(K) = 4a/\mu_{red}$ where $\mu_{red} = (m_s + m_d)/(m_s m_d)$ is the reduced mass, we find $\frac{4a}{\mu_{red}} = 0.598 \text{ GeV}^2$.

Inserting the value of the ratio of a/μ_{red} as determined above, we obtain $Q = m(D^{*+}) - m(D^0) - m(\pi^+) \sim 6 \text{ MeV}$; that is, the amount of available rest mass energy in the usual D^* decay chain is very small. Since the D^* decay occurs nearly at rest in the center of momentum frame of the D^* , in the lab frame the momenta of the D^0 and the accompanying pion will be proportional to their masses (i.e. $p_{D^0} \sim \gamma_{D^0} \times p_{cm} \sim \frac{m_{D^0}}{E_{D^*}} \times$

p_{cm} , $p_\pi \sim \gamma_\pi \times p_{cm} \sim \frac{m_\pi}{E_{D^*}} \times p_{cm}$). For instance, for a typical D^0 with a momentum of 60 GeV in the lab, the pion from the D^* decay will have a momentum of about 4.5 GeV. Thus the pion which accompanies the D^0 is sometimes referred to as “the slow pion”.

In the D^* center of mass, the number of states in phase space per unit interval of dQ is proportional (in the non-relativistic limit) to the square root of the Q value: $dN \propto p^2 dp d\Omega \propto Q^{1/2} dQ$. As a function of Q , while the D^* signal peaks at a small Q value, the phase space background is at a minimum. Moreover, the experimental resolution in Q value is extremely good, typically 1 MeV. These properties of the D^* decay cascade (as seen in Figure 1.4) are a powerful tool for suppressing experimental backgrounds. Finally, it is worth noting that above threshold D^* s are especially abundant. Three D^* s are typically produced per D^0 since the production ratio is roughly given by $\frac{2s_{D^*} + 1}{2s_{D^0} + 1}$.

In the decay cascade $D^{*+} \rightarrow D^0 \pi^+$ and the charge conjugate reaction $D^{*-} \rightarrow \overline{D^0} \pi^-$, the charge of the slow pion is correlated with the charm quantum number of the D^0 meson. This is a method of tagging neutral D^0 mesons and will be essential to the analysis presented in this thesis.

1.2 Theoretical Aspects of Mixing

1.2.1 General Formalism

In the $D^0 - \overline{D^0}$ system, as in the neutral kaon system, it is natural to

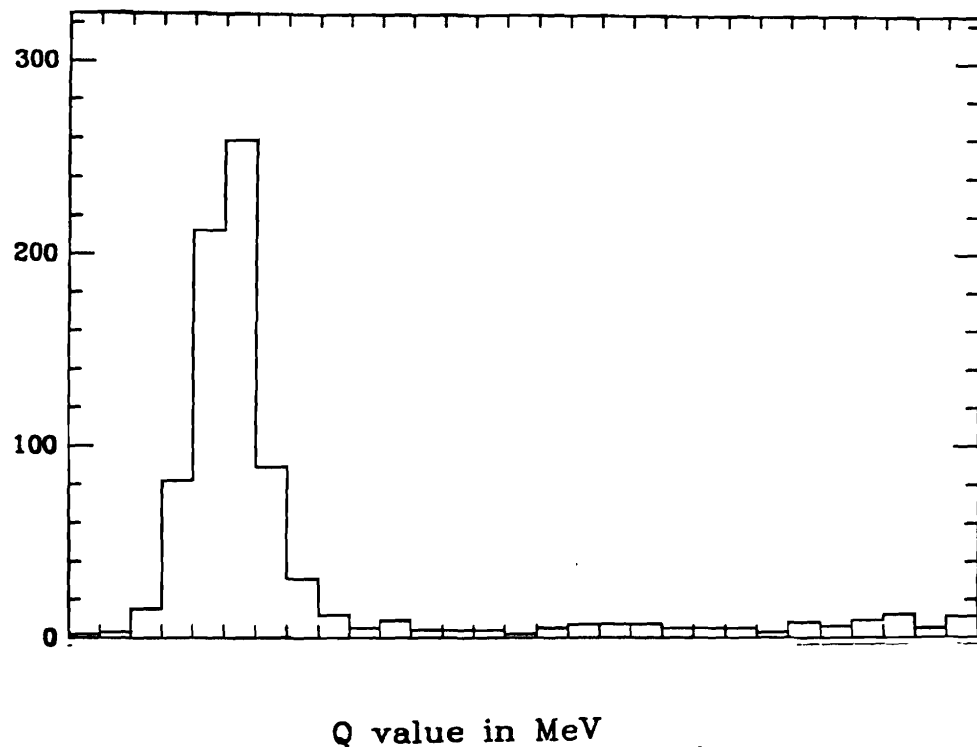


Figure 1.4 Q value distribution for the decay $D^{*+} \rightarrow D^0\pi^+ \rightarrow K^-\pi^+\pi^+$ and charge conjugate.

expect that the eigenstates of the strong and electromagnetic interaction will be superpositions of weak interaction eigenstates. The latter will have definite lifetimes and CP transformation properties. Thus, a D^0 meson which is produced as a strong interaction eigenstate, may transform itself into its antiparticle while decaying by the weak interaction.

To describe mixing in the neutral charm system, we introduce a formalism analogous to the one used for the $K^0 - \overline{K^0}$ system. Let

$$\psi = \begin{pmatrix} \psi_{D^0} \\ \psi_{\overline{D^0}} \end{pmatrix} \text{ or } |\psi\rangle = \psi_{D^0}(t)|D^0\rangle + \psi_{\overline{D^0}}(t)|\overline{D^0}\rangle$$

where $|D^0\rangle, |\overline{D^0}\rangle$ are the two charm eigenstates. The time evolution of ψ is then given by the Schrodinger equation:

$$i\frac{\partial\psi}{\partial t} = H\psi$$

where $H = H_W + H_S + H_{EM}$ is the full hamiltonian with contributions from the weak, strong and electromagnetic interactions. One can decompose H as the sum of two hermitian matrices, $H = M - i\Gamma$. Since the weak interaction is not diagonal in the basis of strong interaction eigenstates, H will contain off diagonal elements, as shown below.

(1.1)

$$i\frac{\partial\psi}{\partial t} = \begin{pmatrix} M_{11} - \frac{i\Gamma_{11}}{2} & M_{12}^* - \frac{i\Gamma_{12}^*}{2} \\ M_{12} - \frac{i\Gamma_{12}}{2} & M_{22} - \frac{i\Gamma_{22}}{2} \end{pmatrix} \begin{pmatrix} \psi_{D^0} \\ \psi_{\overline{D^0}} \end{pmatrix}$$

In the absence of decays $\Gamma_{ij} = 0$. The off diagonal elements of this matrix induce transformations between D^0 and anti- D^0 mesons. Thus

there is no mixing if $\Gamma_{ij} = 0$ for $i \neq j$ and $M_{ij} = 0$ for $i \neq j$. CPT invariance implies $M_{11} = M_{22} = M$ and $\Gamma_{11} = \Gamma_{22} = \Gamma$.

Diagonalizing this equation, we find two eigenvectors:

$$|D_{1,2}^0\rangle = \frac{1}{\sqrt{2(1+\epsilon^2)}}((1+\epsilon)|D^0\rangle \pm (1-\epsilon)|\overline{D^0}\rangle)$$

with eigenvalues $-im_1 - \frac{\lambda_1}{2}$, $-im_2 - \frac{\lambda_2}{2}$, where

$$m_{1,2} = M \pm \text{Re} \sqrt{(M_{12} - \frac{1}{2}i\Gamma_{12})} \sqrt{(M_{12}^* - \frac{1}{2}i\Gamma_{12}^*)} \cong M \pm \text{Re } M_{12}$$

and

$$\lambda_{1,2} = \Gamma \mp \text{Im} \sqrt{(M_{12} - \frac{1}{2}i\Gamma_{12})} \sqrt{(M_{12}^* - \frac{1}{2}i\Gamma_{12}^*)} \cong \Gamma \pm \text{Re } \Gamma_{12}$$

and $\epsilon = \frac{\frac{1}{2}\text{Im } \Gamma_{12} + i \text{Im } M_{12}}{\frac{1}{2}i\Delta\Gamma - \Delta M}$ is a parameter which measures the amount of direct CP violation. If Γ_{12} and M_{12} are real, then $\epsilon = 0$. For most of this thesis, we will assume that all CP violating effects can be neglected.

1.2.2 The time dependence of mixing

In contrast to normal D^0 decays, the number of mixed D^0 decays, as a function of time, is proportional to $t^2 e^{-\Gamma t}$. In this section, we describe how this intriguing and experimentally useful result is obtained.

If a solution of equation (1.1) is prepared at $t = 0$ in a pure $|D^0\rangle$ state, then the initial wave function can be written:

$$|\psi(0)\rangle = |D^0\rangle = \frac{1}{\sqrt{2}}(|D_1^0\rangle + |D_2^0\rangle).$$

The time evolution of $|\psi\rangle$ is found by allowing each of the two weak eigenvectors to evolve independently with its characteristic frequency:

$$|\psi(t)\rangle = \frac{1}{\sqrt{2}}(e^{-(im_1 + \lambda_1/2)t}|D_1^0\rangle + e^{-(im_2 + \lambda_2/2)t}|D_2^0\rangle).$$

At some later time, the state $|\psi(t)\rangle$ will contain a small admixture of $\overline{D^0}$.

To calculate the amount of this mixing as function of time we evaluate the modulus squared of the overlap integral; $|\langle \overline{D^0} | \psi \rangle|^2$ is then the probability that a D^0 has turned into a $\overline{D^0}$. Factoring out $e^{-im_1 t - \frac{\lambda_1}{2} t}$, and using the orthonormality of the weak eigenstates, the overlap integral becomes:

$$\begin{aligned} \langle \overline{D^0} | \psi \rangle &= e^{-im_1 t} e^{-\lambda_1/2 t} \{ \langle D_1^0 | D_1^0 \rangle - e^{im_1 t - im_2 t} e^{\frac{\lambda_1}{2} t - \frac{\lambda_2}{2} t} \langle D_2^0 | D_2^0 \rangle \} \\ &= e^{-im_1 t - \lambda_1/2 t} \{ 1 - e^{im_1 t - im_2 t} e^{\frac{\lambda_1 - \lambda_2}{2} t} \}. \end{aligned}$$

To simplify the algebraic manipulations, we introduce the standard notations $\Delta M = m_1 - m_2$, $\Delta \Gamma = \lambda_1 - \lambda_2$, $x = \frac{\Delta M}{\Gamma}$, $y = \frac{\Delta \Gamma}{\Gamma}$. Here λ_1 is the width of the CP odd eigenstate. In terms of these variables:

$$|\langle \overline{D^0} | \psi \rangle|^2 = \frac{1}{4} e^{-\Gamma t} \{ 1 - 2 \cos(\Delta M t) e^{\Delta \Gamma t} + e^{2\Delta \Gamma t} \}.$$

Since mixing is known to be much less than maximal in the $D^0 - \overline{D^0}$ system, we can expand the arguments of the exponential and cosine in powers of $\Delta M t$ and $\Delta \Gamma t$, (N.B. this expansion would not be valid for the K^0 or B_s systems in which $x, y \sim O(1)$). Retaining all the terms up to second order, (and noting the cancellation of the first order terms in $\Delta \Gamma t$) one finds:

$$|\langle \overline{D^0} | \psi \rangle|^2 = \frac{1}{4} e^{-\Gamma t} [(\Delta M)^2 t^2 + (\frac{\Delta \Gamma}{2})^2 t^2].$$

Thus in contrast to normal D^0 decays which obey an exponential "radioactive" decay law, mixing is characterised by a $t^2 \exp(-\Gamma t)$ time dependence which peaks at $\frac{2}{\Gamma}$.

To observe mixing, many experiments search for wrong sign decays in the abundant and experimentally accessible hadronic modes, for instance $D^0 \rightarrow K^-\pi^+$ or $D^0 \rightarrow K^-\pi^+\pi^-\pi^+$. Thus a full treatment must take account of the fact that wrong sign hadronic final states can also be produced by the double Cabibbo suppressed process (as shown in Fig 1.5.). Relegating the algebra to Appendix II, we find the number of wrong sign decays as a function of time is given by:

$$\begin{aligned}
 I(D^0 \rightarrow K^+\pi^-) = & \frac{e^{-\Gamma t}}{4} [|\alpha|^2 \{ (\Delta M)^2 t^2 + \frac{1}{4} (\Delta \Gamma)^2 t^2 \} \\
 & + (4 - 2\Delta \Gamma t) |\rho|^2 \\
 & + 2 \operatorname{Re}(\rho \alpha) \Delta \Gamma t \\
 & \mp 4 \operatorname{Im}(\rho \alpha) \Delta M t]
 \end{aligned}$$

Here $\rho = \tan^2 \theta_c \hat{\rho}_f = \frac{\langle K^+\pi^- | D^0 \rangle}{\langle K^+\pi^- | \bar{D}^0 \rangle}$ is the double Cabibbo suppressed amplitude. $\alpha = \frac{1-\epsilon}{1+\epsilon}$ is the usual measure of direct CP violation, $|\alpha| \approx 1$. The term proportional to $\Delta M t$ in the above equation has a $-$ sign for wrong sign D^0 decays and a $+$ sign for wrong sign \bar{D}^0 decays. In a sample of events with equal numbers of D^0 s and \bar{D}^0 s, this term will average to zero. It is also explicitly CP violating and thus will be neglected.

We now consider two limiting cases of equation 1.

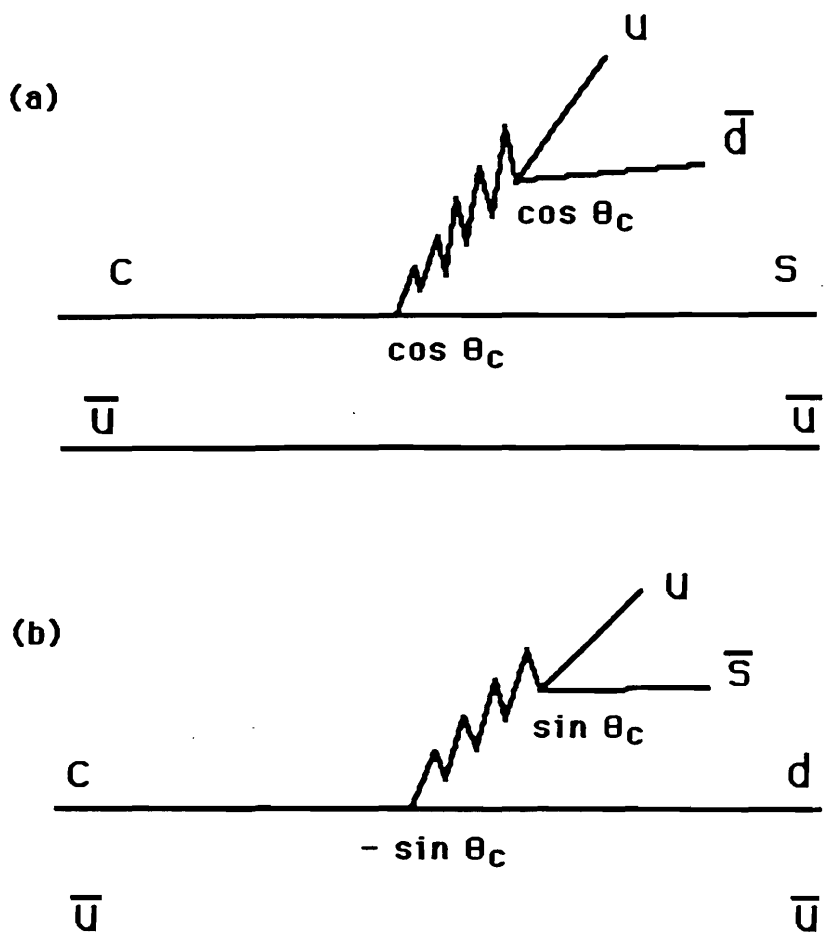


Figure 1.5 (a) The Feynman graph for the Cabibbo favored decay $D^0 \rightarrow K^-\pi^+$ (b) The Feynman graph for the doubly Cabibbo suppressed decay $D^0 \rightarrow K^+\pi^-$

Case 1 : $\Delta M \gg \Delta \Gamma$

$$I(D^0 \rightarrow K^+ \pi^-) = \frac{e^{-\Gamma t}}{4} [(\Delta M)^2 t^2 + 4|\rho|^2]$$

We omit the term proportional to $\Delta \Gamma \tan^4 \theta_c$, since it is third order in a small quantity.

Case 2 : $\Delta M \sim \Delta \Gamma$

$$I(D^0 \rightarrow K^+ \pi^-) = \frac{e^{-\Gamma t}}{4} [(\Delta M)^2 t^2 + \frac{1}{4}(\Delta \Gamma)^2 t^2 + 4|\rho|^2 + 2 \operatorname{Re}(\rho \alpha) \Delta \Gamma t].$$

Thus, even in the presence of double Cabibbo suppressed decays (DCSD), the wrong sign decays due to mixing retain their unique signature: a time dependence proportional to $t^2 e^{-\Gamma t}$. This means that decays due to the Standard model allowed DCSD process can in principle be distinguished from mixing even though both processes yield identical final states. For instance, if decays with $t < 0.88$ psec are excluded from an experimental sample, only 14% of decays due to DCSD are retained while 68% of the mixed decays remain.

In Case 2, we note a term with a time dependence proportional to $te^{-\Gamma t}$ is due to the interference of the mixing amplitude and DCSD amplitude. Such a term will only be important if $\Delta \Gamma \sim \Delta M$, which is not expected to be the case for mixing in heavy quarks where one expects $\Delta M \gg \Delta \Gamma$. By contrast, in K^0 decays $|\Delta \Gamma| \sim |\Delta M|$. This is due to an accident which is peculiar to the kaon system; the K_L is barely above threshold for decay to the 3 pion CP eigenstate ($CP = -1$), while phase space strongly favors a K_s decay to a 2 pion final states

with $CP = +1$. Finally, the 2 pion and 3 pion modes almost completely determine the widths of the K_s and K_L because of their large branching ratios $Br(K_L \rightarrow 3\pi) \sim 34\%$, $Br(K_s \rightarrow 2\pi) \sim 100\%$. In D^0 mixing, the D^0 is far above threshold for most decays to CP eigenstates and the branching ratios for such CP eigenstates as $D^0 \rightarrow \pi\pi$, $D^0 \rightarrow K\bar{K}$, $D^0 \rightarrow \pi\pi\pi\pi$ are small compared to the abundant Cabibbo favored modes, so it is likely that $\Delta M \gg \Delta\Gamma$.

If the amplitude for mixing and the amplitude for DCSD were precisely matched at $t = 2\tau_{D^0}$ and $\Delta\Gamma$ was large, then destructive interference ($\Delta\Gamma\rho < 0$) could wipe out the signature of mixing: an excess of events beyond 2 lifetimes. A simple theoretical argument [Bi87] shows that this scenario is extremely unlikely. The quantity ρ which measures the strength of the DCSD amplitude can be expressed as a product of Kobayashi-Maskawa matrix elements: $\rho \approx V_{cd}V_{us}/V_{cs}V_{us} \sim -\tan^2\theta_c$. The other relevant quantity $\Delta\Gamma (= \Gamma_{odd} - \Gamma_{even})$ is determined by the relative widths of D^0 decays to CP odd and CP even final states. It is quite likely that $\Delta\Gamma < 0$ since there are more possible final states with even CP than final states with odd CP (i.e. $D^0 \rightarrow K^-K^+$, $D^0 \rightarrow \pi^-\pi^+$, $D^0 \rightarrow \pi^0\pi^0$, $D^0 \rightarrow K\bar{K}K\bar{K}$ and $D^0 \rightarrow \pi\pi\pi\pi$ versus $D^0 \rightarrow \pi^-\pi^+\pi^0$, $D^0 \rightarrow K^+K^-\pi^0$, and $D^0 \rightarrow \pi^0\pi^0\pi^0$). While most of the decays listed above have not been observed, $D^0 \rightarrow K^-K^+$, $D^0 \rightarrow \pi^-\pi^+$ and $D^0 \rightarrow \pi^+\pi^-\pi^+\pi^-$ are known to be quite large. Thus $\Delta\Gamma\rho > 0$ which corresponds to constructive interference is the favored scenario.

Unlike experiment E691, most experiments that have studied mix-

ing are unable to resolve times comparable to 0.5×10^{-13} sec $\sim \tau_{D^0}/8$ and thus in effect measure the rate $I(D^0 \rightarrow K^+ \pi^-)$ integrated over all times. In order to make detailed comparisons between different experiments, we calculate r , the integrated number of wrong sign decays per right sign decay:

$$r = \frac{N(D^0 \rightarrow K^+ \pi^-)}{N(D^0 \rightarrow K^- \pi^+)}$$

$$= \frac{\int_0^\infty I[D^0 \rightarrow K^+ \pi^-](t) dt}{\int_0^\infty I[D^0 \rightarrow K^- \pi^+](t) dt}$$

$$= \frac{\int_0^\infty \frac{1}{4} e^{-\Gamma t} [(\Delta m t)^2 + \frac{1}{4}(\Delta \Gamma t)^2 + 4 \tan^4 \theta_c |\hat{\rho}_f|^2 + 2 \tan^2 \theta_c (\Delta \Gamma t) \operatorname{Re}(\hat{\rho}_f \alpha)] dt}{\int_0^\infty e^{-\Gamma t} dt}$$

Using the identities $\int_0^\infty t^2 e^{-\Gamma t} dt = \frac{2}{\Gamma^3}$, $\int_0^\infty t e^{-\Gamma t} dt = \frac{1}{\Gamma^2}$, and $\int_0^\infty e^{-\Gamma t} dt = \frac{1}{\Gamma}$ we find:

$$r = \frac{1}{4} \Gamma \left[\frac{2}{\Gamma^3} (\Delta M)^2 + \frac{1}{2\Gamma^3} (\Delta \Gamma)^2 + 4 \tan^4 \theta_c |\hat{\rho}_f|^2 \frac{1}{\Gamma} + 2 \tan^2 \theta_c \hat{\rho}_f \Delta \Gamma \frac{1}{\Gamma^2} \right]$$

$$= \frac{1}{2\Gamma^2} (\Delta M)^2 + \frac{1}{8\Gamma^2} (\Delta \Gamma)^2 + \frac{1}{2\Gamma} \Delta \Gamma \tan^2 \theta_c \hat{\rho}_f + \tan^4 \theta_c |\hat{\rho}_f|^2$$

$$= \frac{1}{2} x^2 + \frac{1}{2} y^2 + y \hat{\rho}_f \tan^2 \theta_c + \tan^4 \theta_c |\hat{\rho}_f|^2.$$

This can be schematically rewritten:

$$r = r_{\text{mix}} + r_{\text{int}} + r_{2\text{Cabibbo}}$$

where $r_{\text{mix}} = \frac{1}{2}(x^2 + y^2)$ and $r_{\text{int}} = y \tan^2 \theta_c \hat{\rho}_f$ and $r_{2\text{Cabibbo}} = \tan^4 \theta_c |\hat{\rho}_f|^2$.

To recapitulate, experiments which search for mixing in hadronic decay

modes, measure the quantity r . Those experiments which are only sensitive to semileptonic decay modes, for which there is no contribution from doubly Cabibbo suppressed decays, measure r_{mix} . E691 which measures hadronic modes and their full time dependences can, in principle, determine all four quantities: r , r_{mix} , r_{int} , and $r_{2Cabibbo}$.

1.2.3 Standard Model predictions

After the discovery of the b quark, the simple Cabibbo rotation matrix discussed in [1.1] was generalized by Kobayashi and Maskawa to a 3 by 3 unitary matrix [the KM matrix], with the charged current given by:

$$j^\mu = (\bar{u}, \bar{c}, \bar{t}) \gamma^\mu \frac{(1 - \gamma^5)}{2} U \begin{pmatrix} d \\ s \\ b \end{pmatrix}$$

The KM matrix U contains three rotation angles and one complex phase in contrast to the Cabibbo matrix which is determined by one rotation angle. The complex phase allows for CP violation.

There are now three weak isodoublets which have the form:

$$\begin{pmatrix} u_i \\ d_i \end{pmatrix}$$

with $d'_i = \sum_j U_{ij} d_j$. As a consequence of the unitarity of U , first order flavour changing neutral currents again vanish, in agreement with observation:

$$\begin{aligned} \sum_i \bar{d}'_i d'_i &= \sum_{ijk} \bar{d}_j U_{ji}^+ U_{ik} d_k \\ &= \sum_j \bar{d}_j d_j. \end{aligned}$$

A phenomenologically inspired and intuitively useful parameterization of the experimental values of the KM matrix was devised by Wolfenstein:

$$\begin{pmatrix} V_{ud} & V_{us} & V_{ub} \\ V_{cd} & V_{cs} & V_{cb} \\ V_{td} & V_{ts} & V_{tb} \end{pmatrix} = \begin{pmatrix} 1 & \lambda & \lambda^3 \\ -\lambda & 1 & \lambda^2 \\ -\lambda^3 & -\lambda^2 & 1 \end{pmatrix}$$

where $\lambda \sim \sin \theta_c$. This form exhibits most of the important features clearly. Transitions from the upper to lower element of a weak doublet are of order unity (e.g. V_{ud}, V_{cs}). Decays which require jumps across one generation are singly suppressed (e.g. V_{us}), while jumps across two generations are further suppressed (e.g. V_{ub}, V_{ts}).

Within the Standard Model, the magnitude of ΔM_D and $\Delta \Gamma_D$ are determined by the box diagram, a second order weak process in which two W bosons and two virtual quarks are exchanged as shown in Figure 1.6.

The size of ΔM_D is thus controlled by the masses of the internal quarks which circulate in the loop and the strength of their KM couplings. From the Wolfenstein parametrization, the diagrams which contain internal b quarks ($\propto \lambda^4$) can be neglected compared to the diagrams involving internal s or internal d quarks ($\propto \lambda^2$). The most important term is proportional to $m_s^2 - m_d^2$ and is large only if $SU(3)$ symmetry is badly broken [Co83]:

$$\Delta M_{D^0} = \frac{G_F^2}{4\pi^2} f_{D^0}^2 (m_s^2 - m_d^2) m_{D^0} \lambda^2$$

The factor of λ^2 comes from V_{us} , while V_{cs} gives a factor of order one. A simple estimate of ΔM can be obtained by comparing this expression

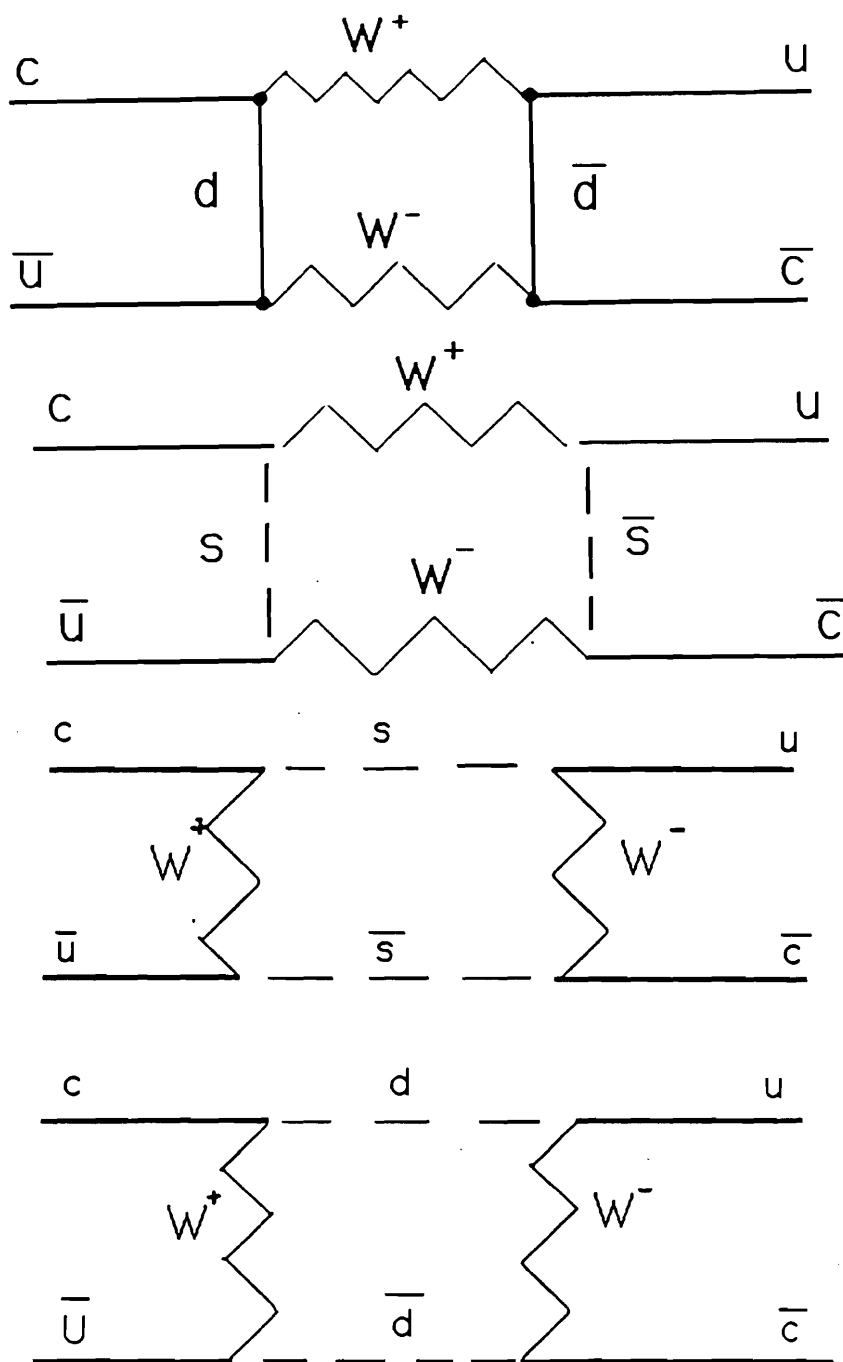


Figure 1.6 Box diagrams for $D^0 - \bar{D}^0$ mixing

with the result quoted earlier for kaon decay:

$$\frac{\Delta M_{D^0}}{\Delta M_{K^0}} = \frac{f_{D^0}^2}{f_{K^0}^2} \frac{m_{D^0}}{m_{K^0}} \frac{m_s^2}{m_c^2}.$$

Assuming $f_{D^0} \sim f_{K^0}$ and various choices of $m_s = 150\text{-}500 \text{ MeV}$, one finds:

$$\frac{\Delta M_D}{\Gamma} \sim 3.5 \times 10^{-4} - 10^{-3}.$$

This implies that

$$r_{D^0} \cong \frac{1}{2} \left(\frac{\Delta M_D}{\Gamma} \right)^2 \sim 0.6 \times 10^{-7} - 0.5 \times 10^{-6}.$$

More elaborate calculations carried out by Chau et al.[Ch83] give similar conclusions ($10^{-7} < r_D < 10^{-4}$), with the lower values usually favored. Thus the simplest treatments in the Standard Model based on short distance dynamics predict a mixing rate below the current level of experimental sensitivity.

The small rate for D mixing expected in the Standard Model is a reflection of the short lifetime of the D^0 meson and the small value of ΔM_D . The ratio $\Delta M_D/\Delta M_K \sim 0.04$ (for $m_s = 500 \text{ MeV}$) is a measure of the size of flavor SU(3) breaking effects relative to flavor SU(4) breaking effects: $\Delta M_D \sim m_s^2 - m_d^2$ while $\Delta M_K \sim m_c^2 - m_u^2$. In the limit of exact SU(3) symmetry, $m_s = m_d$, and there is no mixing. Clearly, SU(4) symmetry ($\Rightarrow m_c = m_s$) is a much poorer approximate symmetry and thus mixing in the kaon system is large. Similar considerations show that ΔM_B should be very large, since $\Delta M_B \propto m_t^2 - m_c^2 \sim m_t^2$.

Recently, Wolfenstein[Wo85] and independently Donoghue, Golowich, Holstein, and Trampetic [Do86], have pointed out that long distance effects due to the strong interaction which break SU(3) flavor symmetry can

give contributions to ΔM in the D system which are typically at least two orders of magnitude larger than the contribution from the box diagram. In these analyses, mixing arises when a D^0 decays to a virtual meson intermediate state that is also accessible to $\overline{D^0}$. The amplitude for mixing is given by the following expression from second order perturbation theory [Do86]:

$$\sum_I \frac{< D^0 | H_W | I > < I | H_W | \overline{D^0} >}{[m_D^2 - m_I^2 + i\epsilon]}$$

Here I refers to the intermediate state and H_W is the weak Hamiltonian. Since the rate of mixing is equal to the modulus squared of this amplitude, it is difficult to make accurate predictions for the size of such dispersive effects without knowing the widths and strong interaction phase shifts of D^0 decays to all the possible virtual intermediate states. Calculations of this effect at the quark-gluon level are also considered to be hopeless[Bi87].

It is however possible to make some estimates of the order of magnitude of such long distance effects. For instance, by assuming that all possible zero strangeness intermediate virtual states contribute coherently to ΔM_D , Wolfenstein derives a theoretical upper limit $r < 5.0 \times 10^{-3}$. In other words, mixing below about the 0.5% level can be accommodated by the Standard Model.

If instead, the only virtual processes which contribute are $D^0 \rightarrow K^- K^+ \rightarrow \overline{D^0}$ and $D^0 \rightarrow \pi\pi \rightarrow \overline{D^0}$, and some assumptions are made about the form factors for these states, Wolfenstein finds $r \sim 2 \times 10^{-4}$. A similar realistic estimate by Bigi[Bi87], which uses the assumption $\Delta M_D \sim \Delta \Gamma_D$, finds $r \sim 10^{-3}$. The analysis of Donoghue et al. at-

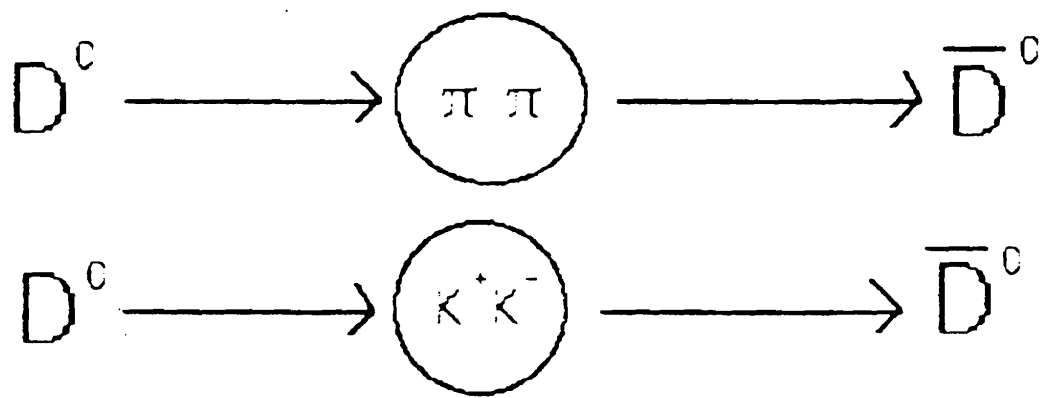


Figure 1.7 Long distance contributions to $D^0 - \bar{D}^0$ mixing with virtual $\pi^+ \pi^-$, $\pi^0 \pi^0$, or $K^- K^+$ intermediate states.

tempts to explicitly calculate the amount of SU(3) breaking induced by long distance effects; they find $r \sim 1 \times 10^{-5}$.

These studies seem to suggest the inadequacy of perturbation theory descriptions, at the present time, to describe processes dominated by long distance dynamics and thus the importance of direct experimental measurements.

1.2.4. Predictions in Nonstandard Models

In many extensions of the Standard Model, the strength of mixing is enhanced by processes which involve the exchange of newly postulated vector or scalar particles. Mixing proceeds either by an analogue of the box diagram with the W bosons replaced by the new vector particle, or in models with extra scalars, where the c and u quarks annihilate to the new scalar particle which in turn becomes a $\overline{D^0}$. These models sometimes produce flavor changing neutral currents but are usually tuned to avoid violent disagreement with experimental results for kaon mixing and the stringent limits on rare kaon decays. Such models however often allow for larger mixing effects in the $D^0\overline{D^0}$ system.

In supersymmetric models, motivated by the desire to eliminate self energy divergences and incorporate gravity, each of the usual fermions (quark, lepton) of the Standard Model has a supersymmetric bosonic (squark, slepton) counterpart. The main contribution to mixing comes from the quark-squark-gluino vertex. A. Datta [Da85] has attempted to estimate this effect and finds $r_D < 3 \times 10^{-5}$ with a favorable choice of

squark mass matrices. This rate is somewhat larger than box diagram predictions.

In a model devised by Kane and Thun to explain the existence of generations, a horizontal gauge boson which mediates transitions between generations can also induce large D mixing. Demanding consistency with the kaon system, they derive a limit $r_D < 1 \times 10^{-3}$ with very large theoretical uncertainties due to the unknown couplings of the new boson. In this model, it is easy to imagine a horizontal boson which mediates transitions between (c,u) quarks rather than between (s,d) quarks and thus evades the stringent bounds on rare K decays. Thus the $D - \bar{D}$ system provides more stringent constraints on the couplings of such a boson.

In some models more elaborate Higgs sectors or more than one Higgs doublet are proposed to explain CP violation. In these models, mixing proceeds by the diagram shown below where H' is the extra neutral Higgs boson. An upper bound on the size of D mixing can be derived by assuming that mixing in the kaon system is saturated by the Higgs induced effect. In that case,

$$\Delta M_D = 0.8 \times 10^{-13} \text{ GeV} \sin^2 \theta_D / \sin^2 \theta_K \Rightarrow r_D = 8 \times 10^{-4} (\sin \theta_D / \sin \theta_K)^4.$$

Here θ_D and θ_K are the couplings of the extra Higgs to the D and K mesons respectively. Neither of these quantities is known or calculable. If the ratio of these two mixing angles is large, D mixing could easily be pushed up into the 1-2% range [Da85],[Ha85].

In models which postulate the existence of another level of struc-

ture below the level of quarks, enhanced mixing is possible. For instance, in the composite technicolor model of King[Ki87] in which the left handed quark doublets and u_R are composite entities, D^0 mixing can be enhanced into the range $r_D \sim .1 - 1\%$.

The possibility of a fourth generation of quarks and leptons cannot be ruled out at the present time. Although the unitarity of the KM matrix provides some constraints, a charge $-1/3$ quark of the fourth generation could enhance D mixing via the box diagram if it was strongly coupled to either the c or u quark. He and Pakvasa find [He85] that existing data permit r_D to be as large as 3.3%. Anselm et al.[An85] perform a similiar analysis and find $r_D < 2 \times 10^{-3}$ from fourth generation mediated mixing. A more general treatment due to Bjorken and Dunietz [Bj87] shows that

$$\Delta M_D \approx [\lambda^2 m_s^2 + m_{B^*}^2 (V_{cB^*} V_{uB^*}^*)^2]$$

where the subscript B^* refers to the lower member of the fourth quark doublet. Taking the mass of the strange quark to be 500 MeV, and assuming that the four by four coupling matrix continues to follow the form postulated by Wolfenstein, they obtain: $(\Delta M/\Gamma)_D \approx 10^{-3} [1 + \lambda^4 (m_{B^*}/m_s)^2]$. Thus if the mass of the B^* quark is extremely large, mixing could be observable.

Many extensions of the Standard Model allow $D^0 - \overline{D^0}$ mixing to be significantly larger than the box diagram prediction. Observations of or upper limits on mixing can provide useful constraints on the masses and couplings of the newly postulated particles in such models.

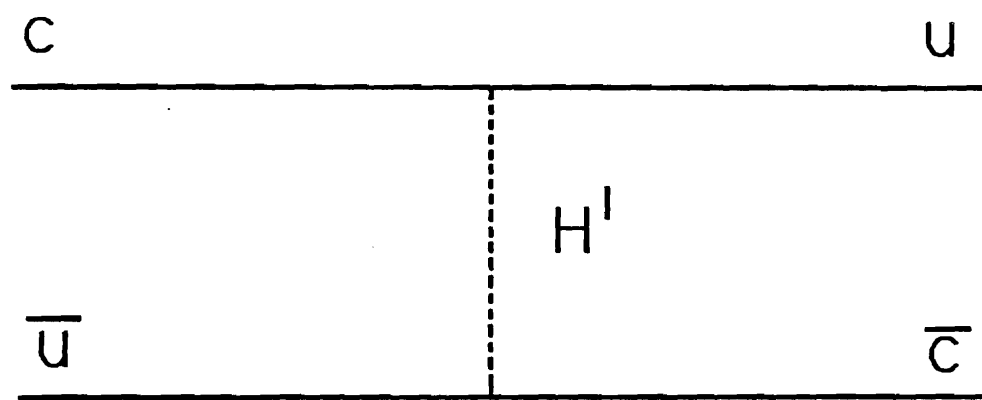


Figure 1.8 Higgs induced $D^0 - \bar{D}^0$ mixing

1.3 Experimental Limits and Hints

Immediately after the discovery of the D^0 meson at SPEAR, experimentalists began to search for $D^0 - \overline{D^0}$ mixing by a variety of techniques. The methods that have been employed can be roughly divided into two classes: direct and indirect. The former means that the experiment used exclusive and completely reconstructed D^0 decays. In contrast, experiments with neutrino or muon beams, or beam dump experiments use inclusive measurements of lepton pairs. After subtracting the expected numbers of such pairs from the various sources of background, and estimating the amount of charm produced, such experiments attempt to *indirectly* constrain the amount of mixing. Limits obtained using direct techniques have the advantage of being independent of assumptions about production mechanisms, and do not depend critically on the accuracy of Monte Carlo simulations used to determine the conventional sources of background. However, until recently, the small size of the fully reconstructed samples of exclusive D^0 decays made it difficult to constrain the amount of mixing. Thus, in this domain, indirect measurements using beam dumps and muon beams which are not limited by statistics were competitive .

Experiment E615 [Lo86] exemplifies the beam dump techniques. To detect mixing the experimenters searched for the reaction



where only the final state muons are detected. A 225 GeV pion beam impinged on a tungsten target. The decay products passed through a

selection magnet, a hadron absorber, 16 planes of drift chambers, 9 planes of MWPC's, an analysis magnet, and a 2 meter thick iron muon wall.

The largest source of background was random $\mu\mu$ pairs produced from other pion interactions in the same rf bucket. This background, which is concentrated in the forward-backward direction, is distinguished from $D - \bar{D}$ mixing by fitting the $|\cos \theta|$ distributions where θ is the angle between a μ^+ and the incident pion direction. The random pion background is strongly peaked near $|\cos \theta| = 0.9$ while the $D^0 - \bar{D}^0$ mixing sample has a relatively flat distribution for $0 \leq |\cos \theta| \leq 0.6$ and then falls off rapidly as $\cos \theta \rightarrow 1.0$. The $|\cos \theta|$ distribution for $D\bar{D}$ pairs is a convolution of measured $\frac{d^2\sigma}{dx_f dp_t^2}$ distributions from other hadroproduction and beam dump experiments (LEBC-EHS,BIBC,ACCMOR,CCFRS), muon spectra from the model of Ali (assuming contributions from $D \rightarrow K\mu\nu$, $D \rightarrow K^*\mu\nu$, $D \rightarrow \pi\mu\nu$ of 55%, 39%, and 6% respectively), and an experimental Monte Carlo simulation. E615 finds a total of 3973 like sign muon pairs with invariant mass greater than $2.0 \text{ GeV}/c^2$. Using their model of the angular dependence of charm hadroproduction, they conclude that, at the 90% confidence level, no more than 63 of the pairs could be due to mixing.

To extract a numerical value for a 90% confidence level limit on the rate of mixing, a value for the total cross section for $D\bar{D}$ production by pion beams must be chosen. It is assumed that each \bar{D}^0 is accompanied with equal probability by a D^0 or D^+ , therefore $\sigma(D^0\bar{D}^0) = \frac{1}{2}\sigma(D^0) = 3.8 \pm 0.5 \mu b/\text{nucleon}$ where $\sigma(D^0)$ is an average of published cross sections from other hadroproduction experiments. It also is assumed that there is

no significant $\Lambda_c - \bar{D}$ production- although the final limit does not change by more than 10% if $\sigma(D\Lambda_c)$ is comparable to $\sigma(D\bar{D})$. The D pair cross section is then extrapolated to the tungsten ($A = 183$) target assuming an A^1 nuclear dependence. This last assumption is especially dubious since target dependences proportional to A^α in the range $\alpha = 0.5 - 0.92$, as well as strong variations of α as a function of x_F and p_T^2 have been reported [Reu86]. For instance, an $A^{0.85}$ nuclear dependence reduces the extrapolated cross-section (and increases the limit) by a factor of 2.2. Since experiment E615 observes only semileptonic decays it is not sensitive to DCSD, thus $r = r_{mix}$. The final limit obtained is $r_{mix} < 0.56\%$

Experiments using conventional spectrometers performed at e^+e^- storage rings or using photon beams have employed the decay chain $D^{*+} \rightarrow D^0\pi^+ \rightarrow K^-\pi^+[K^+\pi^-]\pi^+$ where the charge of the bachelor pion tags the charm quantum number of the D^0 meson at production. The limits from the DELCO, ARGUS, HRS, E87 and NA11 experiments [Ab86], [Al87], [Ya85], [Yam85], [Av80], [Ba83] are given in Table II. The signature of mixing is a reconstructed D^0 decay accompanied by a wrong sign slow pion (e.g. $\{K^-\pi^+\}\pi^-$ final state). This method is inherently limited by the presence of double Cabibbo suppressed decays, expected in the Standard model to occur at a rate $O(\tan^4 \theta_c) \sim 0.3\%$, which yield identical final states.

The ACCMOR collaboration employed an interesting variation of the above methods to overcome the relatively low statistics of their event sample. After tagging a D^0 meson via the decay $D^0 \rightarrow K^-\pi^+$, they ex-

amined the sign of the lepton from the accompanying decay of the second charm in the event. Using this technique in conjunction with the D^* trick, they derived a 90% confidence level limit of 7% on mixing.

1.3.1. The MarkIII events

The ψ'' (3770) resonance decays almost exclusively to $D\bar{D}$ pairs. Using a 4π solenoidal detector at SPEAR the MARKIII collaboration has collected a large sample of reconstructed D decays by operating at the ψ'' . For 224 of these events, they were able to fully reconstruct the D^0 mesons on both sides of the detector (These events are said to be "doubly tagged"). A typical D^0 will decay by the most Cabibbo favored process to a final state with net strangeness -1, while its antiparticle in the opposite hemisphere of the detector will normally decay to a final state with strangeness +1. Thus the vast majority of events should yield final states with no net strangeness. A decay in which the final state strangeness is ± 2 ($\Delta S = 2$) can only occur if one of the D^0 's transforms itself into its anti-particle or if one of the final states is produced by the second order double Cabibbo suppressed mechanism. The MARKIII collaboration found 3 events with $\Delta S = 2$ [Gl85],[Gl88]. From a naive calculation, DCSD should contribute at most 0.8 events. The dominant experimental backgrounds due to double misidentifications of the kaon and pion in Cabibbo favored decay modes are expected to yield 0.4 ± 0.1 events.

However, a more careful consideration which takes account of the restrictions of quantum statistics shows that DCSD are suppressed for

states with odd C parity such as the ψ'' . This can be seen from an argument due to Yamamoto[Yam85], Bigi and Sanda[Bi86]. Since the ψ'' decays strongly to $D^0\overline{D^0}$, the initial state must preserve the C parity of the spin one resonance. Thus the initial state will have the form:

$$|i\rangle = |D^0(k, t_1)\overline{D^0}(k, t_2)\rangle + (-1)^L |D^0(k, t_2)\overline{D^0}(k, t_1)\rangle$$

where $t_{1,2}$ are the two times of decay of the D mesons. If $A(D^0 \rightarrow f_i) = A_i$ and $A(\overline{D^0} \rightarrow f_i) = \overline{A}_i$, then the total integrated number of $\Delta S = 2$ events is given by:

(1.3)

$$\begin{aligned} \text{for } L \text{ odd} \quad & \frac{1}{2} [(x^2 + y^2)(A_1 A_2 - \overline{A_1 A_2})^2 \\ & + (2 - x^2 + y^2)(A_1 \overline{A_2} - \overline{A_1} A_2)^2] \\ \text{for } L \text{ even} \quad & \frac{1}{2} [3(x^2 + y^2)(A_1 A_2 + \overline{A_1 A_2})^2 \\ & + (2 - 3x^2 + 3y^2)(A_1 \overline{A_2} + A_2 \overline{A_1})^2 \\ & + 8y(A_1 A_2 + \overline{A_1 A_2})(A_1 \overline{A_2} + A_2 \overline{A_1})]. \end{aligned}$$

Specializing to the case, $f_1 = f_2 = K^-\pi^+$ (or any other two body final state), $A_1 = A_2 = A$ and $\overline{A_1} = \overline{A_2} = \overline{A}$, then equation (1.3) reduces to:

(1.4)

$$N(\Delta S = 2) = \frac{1}{2}(x^2 + y^2) \quad \text{for } L \text{ odd}$$

$$= \frac{3}{2}(x^2 + y^2) + 4|\rho|^2 \tan^4 \theta_c + 8y|\rho| \tan^2 \theta_c \quad \text{for } L \text{ even}$$

For $D\bar{D}$ pairs in a relative p wave, DCSD to identical two body final states are forbidden. This can be understood from the following intuitive argument. The final state consists of two pairs $[K^-\pi^+], [K^-\pi^+]$. Within each pair, the kaon and pion must be in a relative s wave, since they are spinless particles produced from a D^0 . However, suppose each $[K^-\pi^+]$ pair is thought of as a blob or entity. The two entities are identical spin zero bosons; since they were produced from a p wave state of two D mesons, they must be in a relative p wave state. But these blobs/entities are subject to Bose-Einstein statistics which requires identical bosons to have symmetric wave functions. Hence this final state cannot be reached by DCSD.

The argument given above holds only for decays to pseudoscalar-vector and pseudoscalar-pseudoscalar final states. It does not hold for vector-vector final states, for instance $D^0 \rightarrow K^*\rho$ or $D^0 \rightarrow \rho\rho$. In the latter case the two spins of the ρ mesons allow for an extra degree of freedom. For instance the two ρ are allowed to be in a orbital angular momentum state $L = 0$ or $L = 2$ provided the total angular momentum of the each rho pair is zero. Thus the two blobs can be distinguished.

If double Cabibbo suppressed decays are neglected, then equation

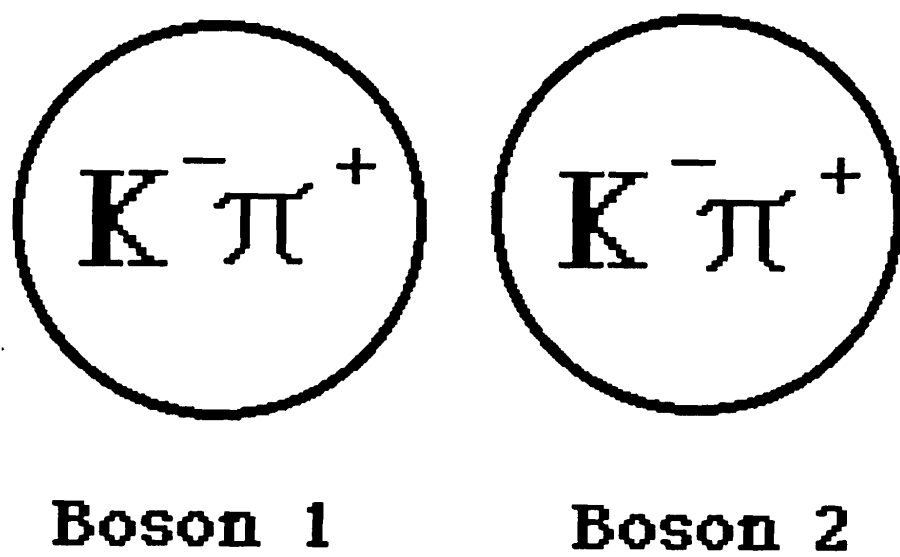


Figure 1.9 Illustration to accompany the intuitive argument for the suppression of DCSD in a p-wave state. The kaon and pion within each circle must be in a relative s-wave since they are produced by the decay of a pseudoscalar particle. Thus the two circled bosons must be in a relative p-wave state.

(1.4) shows that mixing in a p-wave state is suppressed by a factor of three relative to mixing in an s-wave state. This can again be understood as a consequence of quantum statistics. If L is odd, and if one of the D mesons mixes before the other one decays, then an antisymmetric state of $D^0 D^0$ will appear. This is forbidden since the D mesons are identical bosons and thus must form a symmetric state by the generalised exclusion principle. Thus one D^0 must decay before mixing can occur in a p wave state.

In two of the wrong strangeness events observed by MARKIII, the decays $D^0 \rightarrow K^- \pi^+ \pi^0$ were observed on both sides of the detector. The majority of $D^0 \rightarrow K^- \pi^+ \pi^0$ decays are saturated by quasi two body modes (the non-resonant component is only 5% of the total); that is the $K^- \pi^+ \pi^0$ usually resonates as a $K^{*0} \pi^0$ or as a $K^- \rho^+$ state. A Dalitz plot analysis revealed that one of the MarkIII events was consistent with $K^- \rho$ versus $K^- \rho$, while the other was consistent with $K^{*0} \pi^0$ on both sides of the detector. If this conclusion were certain i.e. there was no non-resonant component and no background contamination, then the two events would be a "smoking gun" for mixing. These events would imply a mixing rate of $r \approx r_M \sim 1\% *$.

* A maximum likelihood analysis by G.Gladding [Gl88], based on the MarkIII results, finds that if DCSD decays are neglected, then $r_M \approx 1.2 \pm 0.6\%$. This implies a 90% confidence level lower limit on mixing: $r_M > 0.4\%$. Conversely, if $r_M = 0$ and the wrong sign $K\pi\pi^0$ events are non-resonant, then $|\rho_{K^+\pi^-\pi^0}|^2 = (7 \pm 4) \tan^4 \theta_c$.

Table III *Limits on mixing*

Experiment	Technique	Result (90% CL)
Stanford,Berkeley (1977) at SPEAR (6.8 GeV) [Fe77]	$e^+e^- \rightarrow \gamma^* \rightarrow D^{*+}X$ $D^{*+} \rightarrow D^0\pi^+ \rightarrow K^-\pi^+\pi^+$	16%
SLAC,LBL (1977) at SPEAR (4 GeV) [Go77]	$e^+e^- \rightarrow \gamma^* \rightarrow D^0X$ $D^0 \rightarrow K^-\pi^+$ and K^- in opposite hemisphere	18%
E87(1980) [Av80]	$\gamma p \rightarrow D^{*+}X$ $D^{*+} \rightarrow D^0\pi^+ \rightarrow K^-\pi^+\pi^+$	11%
EMC at CERN (1981) [Au81]	$\mu^+N \rightarrow \mu^+(\mu^+\mu^+)X$	20%
Caltech,Chicago,Rochester, Fermilab,Stanford(1982) [Bo82]	$\pi^-Fe \rightarrow \mu^+\mu^+$	4.4%
ACCMOR (1983) 120-200 π^- on Be [Ba83]	$D^{*+} \rightarrow D^0\pi^+ \rightarrow K^-\pi^+\pi^+$ or tag a D^0 with a wrong sign e^-	7%
Bologna,Dubna,Munchen Saclay (1985) [Be85]	$\mu^+N \rightarrow \mu^+\mu^-\mu^-X$	1.2%
DELCO at PEP(1985) [Ya85] (29 GeV)	$e^+e^- \rightarrow \gamma^* \rightarrow D^*X$ $D^{*+} \rightarrow D^0\pi^+ \rightarrow K^-\pi^+\pi^+$	8.1%
HRS at PEP (1986) [Ab86] (29 GeV)	$e^+e^- \rightarrow \gamma^* \rightarrow D^*X$ $D^{*+} \rightarrow D^0\pi^+ \rightarrow K^-\pi^+\pi^+$	4%
E615(1986) [Lo86] Princeton,Chicago,Iowa State	$\pi^-W \rightarrow \mu^+\mu^+$	0.56%
Argus at DORIS (1987) (10GeV) [Al87]	$e^+e^- \rightarrow \gamma^* \rightarrow D^*X$ $D^{*+} \rightarrow D^0\pi^+ \rightarrow K^-\pi^+\pi^+$	1.4%

1.3.2 Same sign dimuons

Experiments using neutrino beams have repeatedly seen "hints" (signals with a significance of 1.8-2.8 σ) of same sign dimuons at a level higher than expected from semileptonic K , π decays. Although these excess events could be attributed to W^+ exchange followed by gluon bremsstrahlung, the rate observed by the CDHS collaboration [Bu85] is at least 30 times higher than published predictions based on first order perturbative QCD [La86],[Cu86]. Another explanation is $D^0 - \overline{D^0}$ mixing at the 1-2% level [Bi86], [Bj87] *. Although the observed events have kinematic properties consistent with charm i.e. p_T , ϕ_{12} , z_{vis} (the fraction of the incident neutrino energy observed in the calorimeter) distributions; the ratio of same sign to opposite sign dimuons seems to be energy dependent. This would not be expected if these events were due to mixing. Finally, the most recent high statistics neutrino experiment E744 performed at Fermilab finds a much smaller rate of same sign dimuons [Or87].

Thus at the time our experiment was performed, a mixing signal of 1% was consistent with all previous limits and might have accounted for the anomalies in the MARKIII and CDHS data samples.

1.4 On Charm Production and Detection

According to a widespread misconception, fixed target experiments cannot provide useful information on rare charm decay modes. This erroneous belief arose because the first efforts to detect charmed mesons at fixed target experiments were only marginally successful. In contrast to

* An alternative theoretical treatment by Barger et al.[Ba82] finds that 1% D mixing cannot account for the observed rate of same sign dimuons.

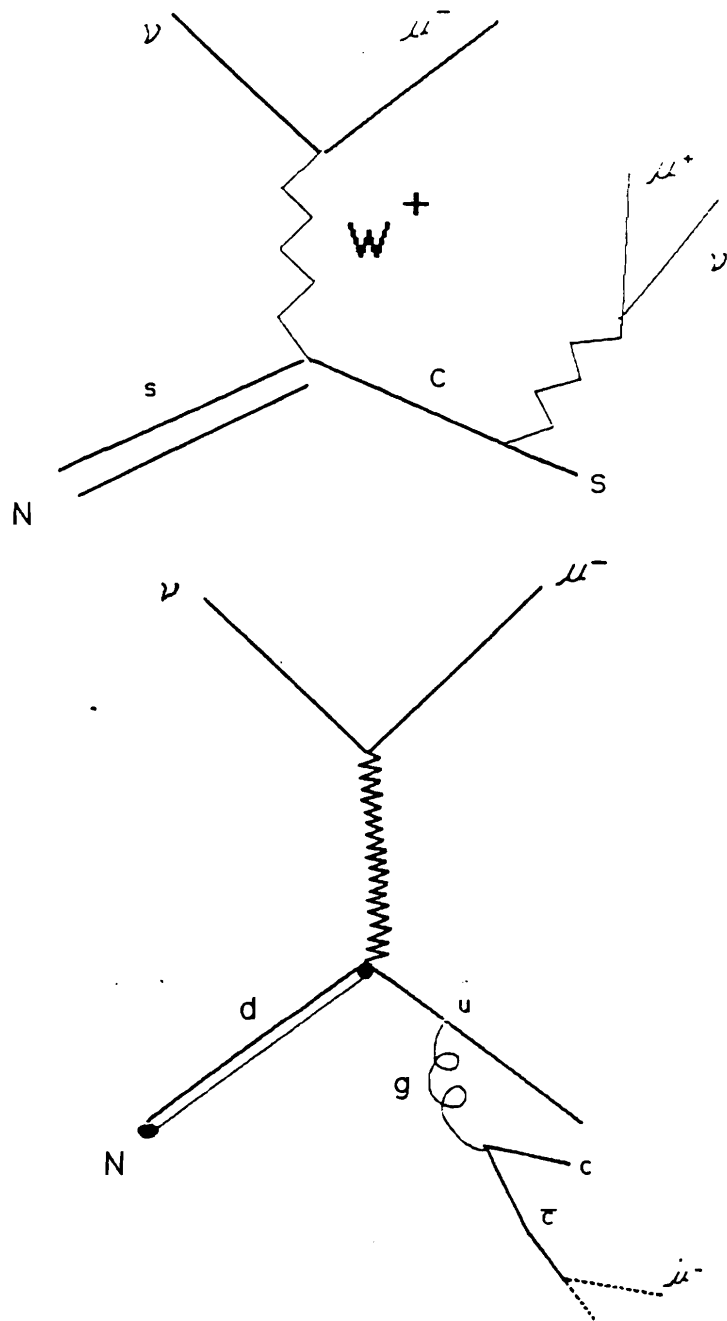


Figure 1.10 (a) Opposite muons in neutrino charm production (b)
 Same sign dimuons from gluon bremsstrahlung

the e^+e^- environment in which roughly 33% of the events contain charm, and where the average multiplicities are low (~ 4.4), fixed target experiments are plagued by severe hadronic backgrounds and large numbers of spurious combinations.

The higher instantaneous rates for heavy quark production are, however, clearly advantageous. For instance [Bj86], if the 10^{13} 800 GeV protons generated per minute by the Fermilab Tevatron were to be directed into a single beam dump, then $10^{10} c\bar{c}$ pairs and $10^6 b\bar{b}$ pairs would be generated per minute. This can be compared to the 30000 $c\bar{c}$ pairs or 7000 $b\bar{b}$ pairs generated per *year* at a typical e^+e^- storage ring. However, for early fixed target experiments, the poor signal to background ratios of the charm signals made it difficult to extract useful physics results, outside of the limited domains of cross-section and lifetime studies.

It was hoped that specialized triggers which exclude a large fraction of events with a simple criterion and thus enhance the fractional charm content of the recorded events would allow the large instantaneous rates of fixed target experiments to be fully exploited. Triggers based on various criteria were attempted: multiplicity jumps downstream of the target, high p_t leptons produced by semileptonic decays of charm, ϕ 's or kaons associated with hadronic decays, or high mass diffractive photoproduction ($\gamma p \rightarrow p^* X$ where the invariant mass of X is large). But these valiant efforts were mostly unsuccessful.

These early fixed target experiments were unable to take advantage of one feature of charm production which distinguishes it from most

hadronic backgrounds. Since charm decays by the weak interaction, the charmed hadron travels a short distance from its point of production before decaying. To resolve this distance, the transverse resolution of the detector must be significantly smaller than the typical impact parameter of the charm decay ($\frac{\sigma_0}{c\tau} \ll 1$). For charm, $c\tau \sim 150\mu m$ while the resolution of the traditional drift chamber or MWPC is at best $\sim 150\mu m$. In the early 1980s, Heinje et. al. [He81] introduced a new type of detector based on the silicon technology used to make integrated circuits, which had a resolution $\sigma_0 \sim 15\mu m$, sufficient to resolve the charm decay vertex. This type of detector, referred to as silicon microstrip detector or SMD, was first used in NA11, a fixed target hadroproduction experiment at CERN.

1.5 On Experiment E691

Fermilab experiment E691 is the first high statistics fixed target charm experiment. Using a traditional two magnet spectrometer of large acceptance combined with a silicon microstrip vertex detector and an open trigger, this experiment was able to overcome the limitations of the fixed target environment and collect large clean samples of charmed particles.

In this experiment, we use the D^* decay chains $D^{*+} \rightarrow D^0\pi^+ \rightarrow [K^-\pi^+]\pi^+$ and $D^{*+} \rightarrow D^0\pi^+ \rightarrow [K^-\pi^+\pi^-\pi^+]\pi^+$ to tag the charm quantum number of the D^0 at production. The right sign D^* signals have a superb signal to background ratio and provide a model independent normalization for our measurement of mixing. Using the unique time dependence of mixing and the fine grain decay time resolution of our silicon

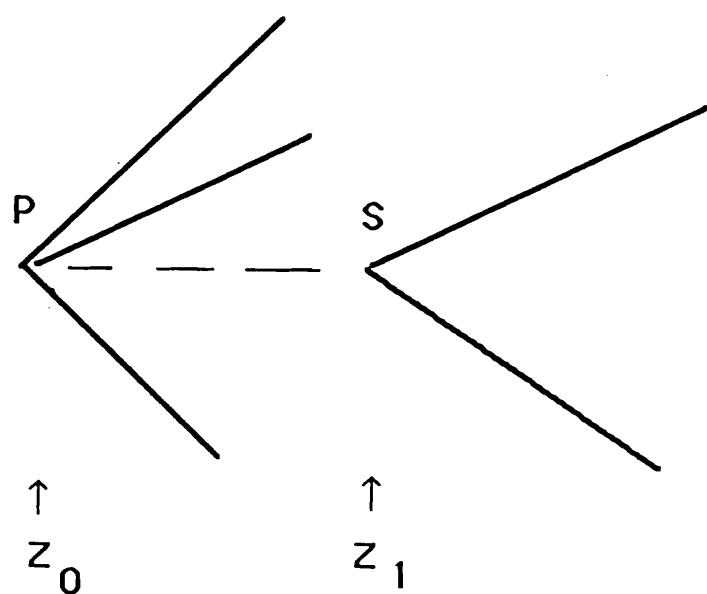


Figure 1.11 The spatial separation of the charm vertex from the point of production is used to measure the decay time in experiment E691. Here z_0 is the production vertex and z_1 is the decay vertex. $\Delta z = z_1 - z_0$ is the longitudinal vertex separation. The proper decay time can then be computed: $t \approx \frac{\Delta z}{\gamma\beta}$.

detectors, we then fit the time distributions of wrong sign decays and thus distinguish mixing, DCSD, and possible interference effects.

2

The Beam and The Target

The 800 GeV proton beam of the Fermilab Tevatron can be used to produce secondary beams of kaons, pions, muons, neutrinos or photons for fixed target experiments. Although the fractional charm content of hadronic neutrino production is $0(10^{-1})$, the total neutrino cross section is so small that it is impossible to produce sufficiently intense beams to study exclusive charm final states in detail. Muon beams are ruled out for similar reasons. We choose a photon beam rather than a hadron beam for the following reasons: the fractional charm content of photo-produced hadronic events is roughly 0.5% compared to 0.1% in charm hadroproduction, and the signal to background ratio is much more favorable in photoproduction (typically by a factor of 5-10). With a photon beam, charm is produced by the QCD process of photon gluon fusion. Thus the effective center of mass energy ($\sqrt{s_{eff}}$) includes the full incident photon energy, whereas hadroproduction proceeds by quark-quark and gluon-gluon fusion which utilizes at most a fraction of the incident projectile energy. This is critical since heavy quark cross sections near threshold are rapidly increasing functions of s_{eff} .

2.1 The Proton Beam and the Accelerator

To produce high energy photons suitable for charm studies, one must first accelerate a beam of protons. This complex process is briefly described below.

Protons from a cylinder of hydrogen gas are ionized by an electric arc and injected into a Cockcroft Walton where they are electrostatically accelerated to about 750 KeV. They then pass through a linac in which 160 meters of drift tubes raise their energy to 200 MeV. The protons are transferred to a 216m Booster Ring, a large acceptance low field synchotron, where they are accelerated through the transition energy to 8 GeV. They are then injected into the 1000 meter radius Main Ring which is a traditional strong focusing alternating gradient synchotron (pairs of vertically and horizontally focusing quadropole magnets reduce the size of betatron oscillations and thus allow for small aperture magnets). The Main Ring accelerates the protons to 150 GeV and then injects them into the Saver, an array of liquid helium cooled Nb-Ti superconducting magnets located directly above the Main Ring. In the Saver, the protons are accelerated to 800 GeV and then extracted [Sa76],[Ed85].

The RF cavities of the Main Ring impose a temporal structure on the beam; they group the protons into "buckets "2 nanoseconds in length separated by 19 nanoseconds. This RF structure of the proton beam is preserved in the photon beam.

Roughly each minute, a 22 second spill begins. (N.B. This rel-

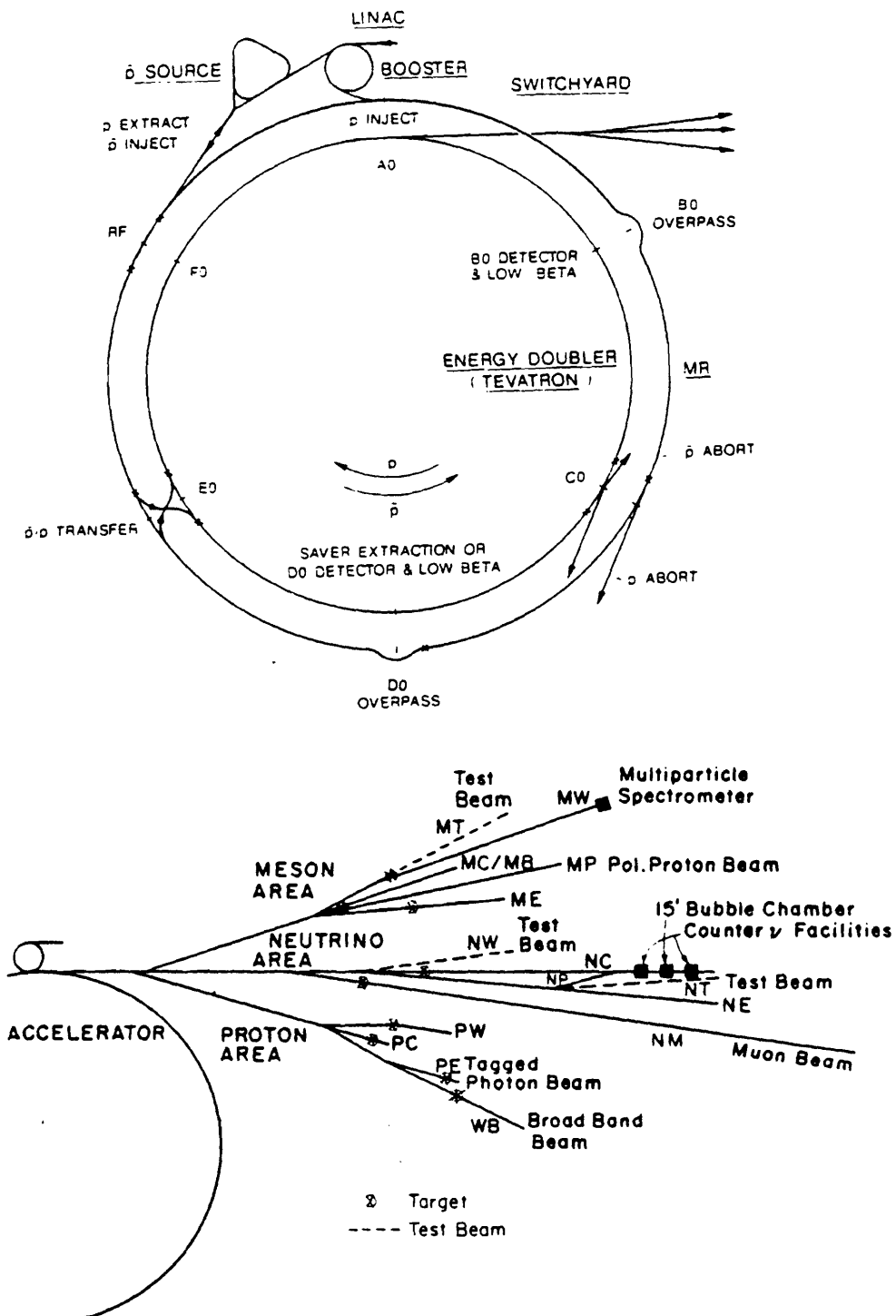


Figure 2.1 Schematic of the Fermilab Tevatron

atively slow extraction is essential for our experiment because it allows the data acquistion system of our experiment to record more events per minute. In the earlier one ring operating mode of the Fermilab machine, with 4-6 spills per minute, each one lasting only 1 second, the data acquistion system was saturated a factor of two more quickly.) The beam is resonance extracted (by exciting a betatron oscillation) and then split electrostatically by a septum into three beams for the Meson, Neutrino, and Proton Areas. The beam for the proton area is then split vertically for the PWest, PCenter, and PEast beamlines. Typically 2.5×10^{12} of the roughly $1. \times 10^{13}$ available protons were allocated for photon physics and sent to the PEast beamline.

2.2. The Electron and Photon Beam

The protons for PEast are focused and directed onto a 30 cm long Be target. The resulting charged particles are bent out into a dump leaving only π^0 's and hadronic neutrals. Photons from the decay $\pi^0 \rightarrow \gamma\gamma$ are then converted to e^+e^- pairs in a 0.32 cm thick lead sheet. The negatively charged component is magnetically selected. The resulting 260 ± 8.5 GeV electrons and residual pions are transported through a three stage beam line. Each stage consists of a quad doublet, a vertically and horizontally focussing quadrupole magnet, and a string of bending magnets. Horizontal and vertical collimators interspersed between the magnets define the beam energy. The collimators also reduce the pion contamination; since pions are produced with a higher average p_t than electrons (300 MeV/c

versus 19 MeV/c)* and the optics of the beamline is configured so that those particles that are produced at large angles are focussed far from the beam axis at the collimators. The final pion contamination is measured to be less than 1%.

The beam is bent three times and the final electron beam arrives at the experimental hall 282 meters downstream of the proton target and 7 meters west of a 0 degree line drawn straight from the target. This is necessary to reduce the rate of random triggers from the wide halo of muons produced at the upstream enclosure.

The electron beam passes through a tungsten radiator (0.2 radiation lengths) and produces photons as the electrons decelerate in the Coulomb field of the tungsten nuclei. The electrons are swept out by a bending magnet and directed into an array of shower counters. The remaining photons with energies between 80 and 260 GeV (average energy about 145 GeV) are highly collimated and have a $\frac{1}{k}$ spectrum characteristic of bremsstrahlung production in the thin radiator approximation [Ts74]. They interact in a 2" Be target and the decay products are recorded in the spectrometer.

Since the electrons are produced by a multi-stage process, the final electron flux is several orders of magnitude smaller than the incident proton flux. Typically the e/p ratio is measured to be 2.6×10^{-5} for 260 GeV electrons. Roughly 5% of the buckets contain more than one electron.

* The dominant contribution to the mean p_T for electrons, in contrast to pions, is due to multiple scattering in the lead target.

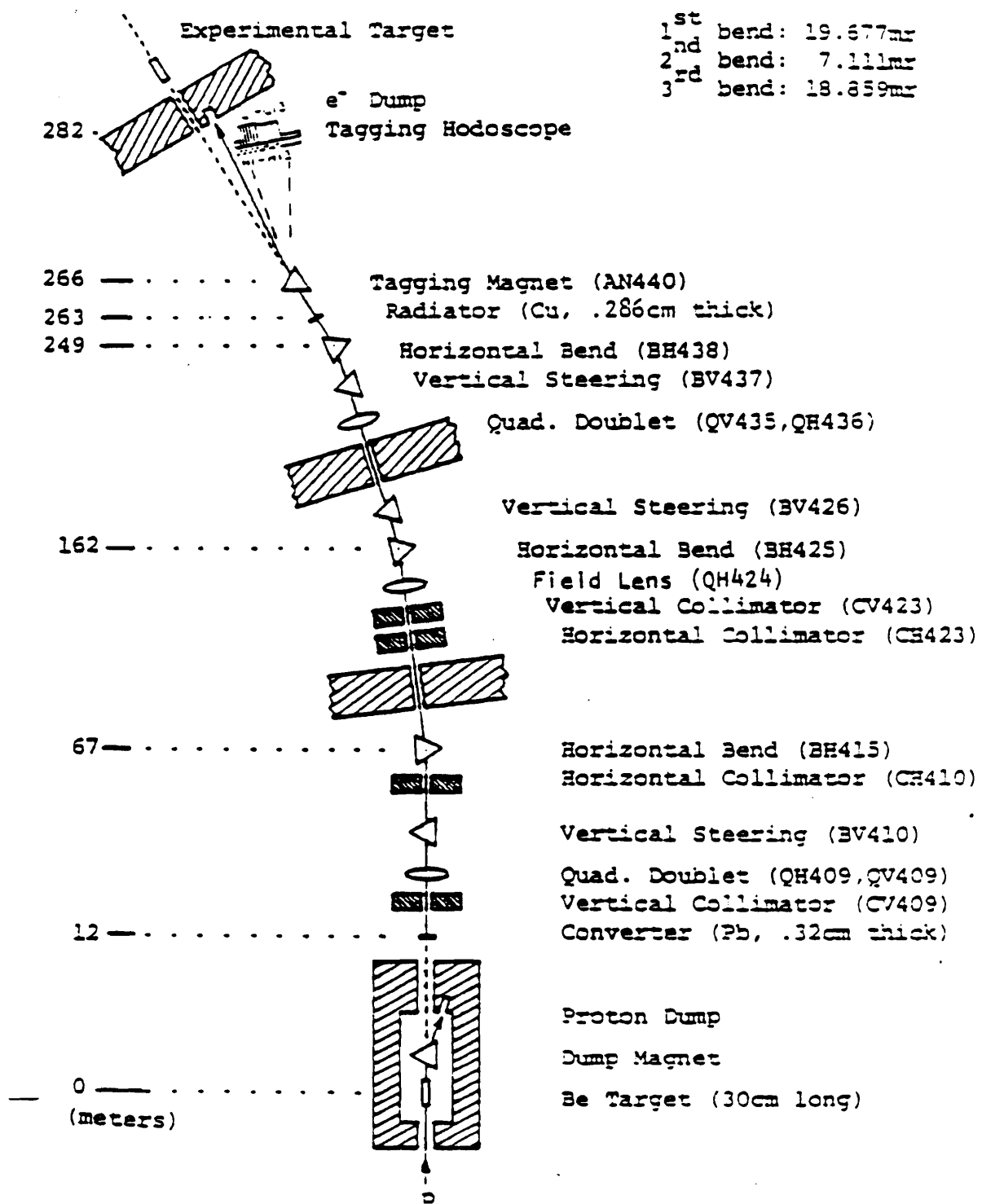


Figure 2.2 The Proton East Beamline

These superbuckets are not a severe background since the probability of two photons interacting hadronically is negligible.

A small but interesting background is produced by synchotron radiation as the electron beam is bent by the last dipole magnet. This source of background can be observed by removing the radiator and the target, with the tagging magnet turned on. The resulting horizontal tail of the neutral beam can then be detected in beam monitors located in front of the calorimeters.

The most severe electromagnetic background is photoproduction of e^+e^- pairs in the Be target. The cross-section for this process is proportional to Z^2 and is about 200 times larger than the cross section for a hadronic interaction (typical rates are $3. \times 10^5$ Hz compared to 300 Hz for hadronic interactions). Fortunately the opening angle for pair production is typically 2 milliradian (equal to the sum in quadrature of the production angle $\sim \frac{1}{\gamma}$ and the multiple scattering angle $\sim \frac{21 \times \sqrt{L/L_R}}{p(\text{in MeV})}$). Thus when projected downstream through the spectrometer and spread out by the magnetic field, these pairs fill a narrow band 3.5 cm wide through the center of the spectrometer.

The tagging system is an array of lead glass shower counters and scintillator hodoscopes used to detect and measure the energy of the incident photon. The photon energy is given by $E_\gamma = E_{beam} - E_{tag}$, where the first term is the energy of the electron beam and the second term is the energy recorded in the tagging system. The most energetic photons produce very low energy electrons which are bent beyond the furthest tag-

ging counter (L13), thus only photons in the energy range 70 - 230 GeV can be measured. The tagging energy cannot be accurately determined for events in which two overlapping electrons are in the same bucket and both radiate. Other types of events which produce wide showers that span more than one tagging counter also cannot be reconstructed.

The tagging system is calibrated in a two step procedure with the target removed. The electron beam is first directed into the C counter, a tungsten-lucite shower counter positioned on the front face of the calorimetry at the beam spot. The calibration for the C counter is then calculated in terms of the beam energy E_{beam} . The radiator is inserted, and the energy calibration for the tagging counters is also determined in terms of the electron beam energy, since $E_{tag} = E_{beam} - E_{Ccounter}$. The electron beam energy is then calibrated by using clean quasi-elastic $\psi \rightarrow \mu^+ \mu^-$ decays in which no extra energy is recorded in the calorimetry and no extra tracks over 3 GeV are detected in the tracking chambers. This method is consistent with an independent calibration performed using $\rho \rightarrow \pi^- \pi^+$ decays. The tagging energy is typically known to an accuracy of $\pm 8\%$. The tagging system is also a component of the experimental trigger. The reconstructed photon energy is an input to the determination of x_F and is critical in studies of charm production mechanisms.

2.3 The Target

The choice of the target material is a compromise between the conflicting requirements of low pair rates, small multiple scattering, large

hadronic cross sections, and good acceptance. Although the pair rates (and multiple scattering angles) scale as Z^2 (Z), hydrogen and helium targets have very low densities and thus require long targets (~ 1 m) to achieve reasonable interaction rates. Such long targets lower the acceptance of the spectrometer, and make vertex localization difficult. Beryllium is one of lightest elements easily found in a dense solid form. In contrast to lighter materials, Beryllium does not require cryogenic cooling and although it is quite toxic, it can be coated in such a way that it can be safely handled. Our target had dimensions: $1.25\text{cm} \times 2.5\text{cm} \times 5\text{cm}$. The x and y dimensions are sufficiently large, so that when the beamline is properly tuned, the beam spot is contained within the face of the target. The dimensions of the photon beam spot are roughly: $\sigma_x \sim 0.8$ cm and $\sigma_y \sim 1.8$ cm. The dimensions of the target are also well matched to the $2.5\text{cm} \times 2.5\text{cm}$ area of the first detector plane of the silicon telescope.

3

The Spectrometer

3.1 Introduction

This chapter contains a description of the Tagged Photon Spectrometer (TPS), a large acceptance two magnet spectrometer with silicon microstrip detectors, 35 planes of drift chambers, two threshold Cerenkov counters, fine grain electromagnetic calorimetry, hadronic calorimetry, and muon detection. The vertex detector will be described in some detail, and an overview of the other components of the spectrometer will be provided. Other theses [Ra87],[Me86],[Bh84],[Su84],[De83],[Du82] contain complementary and detailed discussions of the other detectors.

3.2.1 The Silicon Microstrip Detectors (SMDs)

To separate the production and decay vertices for charm decays, a detector with a $15\mu m$ intrinsic resolution which is capable of operating in a high rate environment $\sim 10^6 Hz$ is necessary. The silicon microstrip detector satisfies these requirements and has brought about a renaissance in fixed target physics.

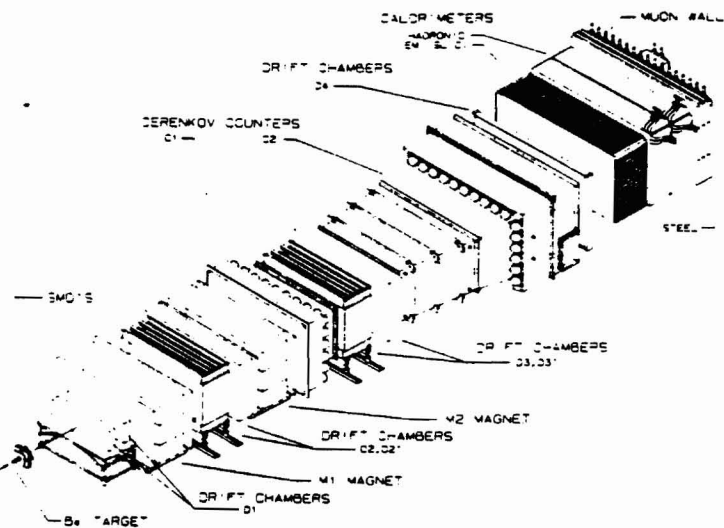
Although semiconductor detectors were used extensively in the

past as photon detectors and calorimetric detectors in nuclear physics, they were first applied to the detection of particles in the GeV energy range by Yuan in 1960[Yu60]. The NA1 collaboration later used silicon detectors in a multiplicity trigger[Be73]. In the 1980s, Heijne, Kemmer, Jarron et al. developed a position sensitive detector that is suitable for high energy physics[Ke80],[Hei80] [Hei81],[Ja84]. A telescope of six detector planes was used at CERN in the NA11 hadroproduction of charm experiment which demonstrated the feasibility of this type of detector. The vertex detector of experiment E691 borrowed some features of the NA11 design as well as features of a design for a vertex detector in the Ω spectrometer - a fixed target photoproduction experiment.

3.2.2 Principle of Operation

The band gap in a semiconductor is only a few electron volts. In contrast the energy required to make an ion pair in a typical gaseous detector material like argon is about 30 electron volts. The higher densities of solid state devices also allow much larger amounts of charge to be collected: typically 72000 ion pairs are generated per mm in silicon versus 10 ion pairs per mm in argon-ethane. Thus the dE/dx energy loss of a particle in a semiconductor does not have to be multiplied as in a MWPC and very thin detectors become practical.

Silicon rather than germanium or gallium arsenide is the semiconductor of choice for high energy physics. Germanium, because of its small band gap and high electron mobility, requires cyrogenic cooling in order



E691 TAGGED PHOTON SPECTROMETER

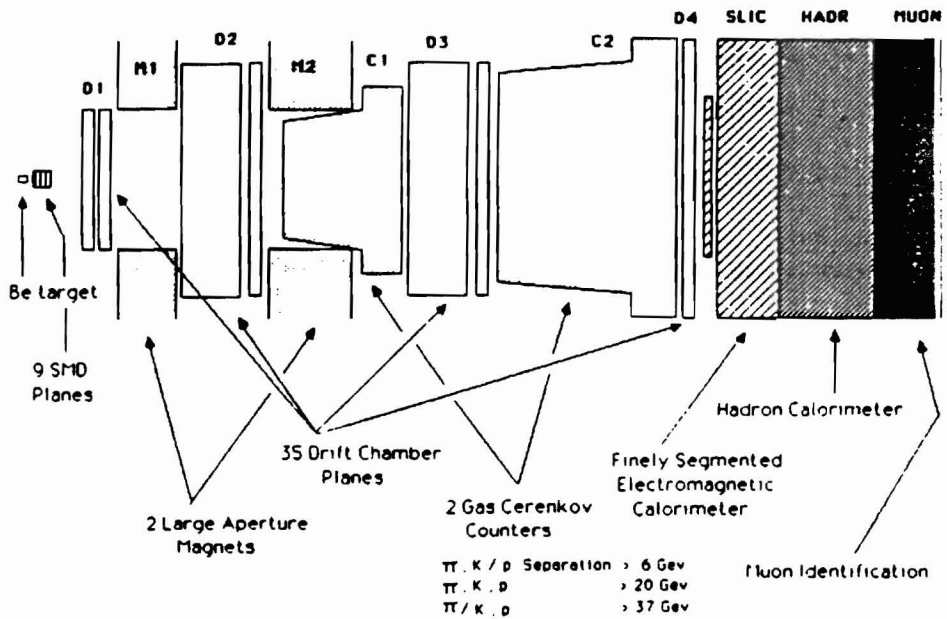


Figure 3.1 The Tagged Photon Spectrometer

to prevent thermal fluctuations from exciting electron hole pairs into the conduction band and producing large leakage currents. Gallium arsenide devices are still an exotic technology. Both GaAs and Ge also have large cross sections for pair production ($\sigma_{e^+e^-} \propto Z^2$) and large multiple scattering errors ($\sigma_{multiple} \propto Z$). Silicon, in contrast, has a much smaller value of Z and can be operated at room temperature. In addition, a well established "planar process" [Ke80] based on integrated circuit fabrication technology has been developed for silicon.

Table 3.1 Properties of semiconductors

Type of Material	Si	Ge	GaAs
Density	2.33	5.33	5.32
Z	14	32	31-33
E band gap (eV)	1.12	0.66	1.42
ΔE /pair (eV)*	3.6	2.8	4.1
Mobility $cm^2/V\ sec$	1500	3900	8500

* The average energy required to make an electron hole pair is greater than the band gap energy: much of the incident energy is converted into other types of crystal excitations.

A silicon microstrip detector (SMD) plane consists of a set of strips, each of which is a reverse biased p-i-n junction. The intermediate (i) material is high resistivity undoped n type silicon. In such a p-i-n junction, to which no external voltage has been applied, holes and electrons initially diffuse through the material. The holes migrate to the p type side, while

the electrons diffuse towards the n type side and vice versa. As an equilibrium is established, a small potential difference builds up which forces the holes to accumulate on the p side and the electrons to accumulate on the i side, as shown in Fig 3.2(a). The immobile lattice ions in a small region of the junction are ionized.

As a function of z , there is a non-zero excess of positive charge in a thin layer of the undoped material and an excess of negative charge in a thin layer of the p material. This region of net charge is called the "depletion zone" or "space charge region" since it is depleted of free charge carriers. By Poisson's equation $dE/dz = 4\pi\rho$, this zone will develop an electric field for which the maximum value depends linearly on the depletion depth and will create a potential for which the maximum value depends quadratically on the depletion depth. If a negative voltage is applied to the p material, more of the fixed positive lattice ions in the undoped region will be uncovered and the depletion zone will become larger [see Fig 3.2(b)]. The current measured across the p-i-n junction will be zero except for a small contribution from minority carriers which diffuse through the material and give rise to a leakage current. In order to collect a sufficient amount of charge for particle detection, the entire silicon wafer must be depleted.

As a minimum ionizing particle passes through such a silicon plane, it excites electron-hole pairs (excitons) and lattice vibrations (phonons). If it deposits $\sim 17\text{eV}$, it may on occasion create collective modes such as plasmons. A typical minimum ionizing particle produces 24000 electron-

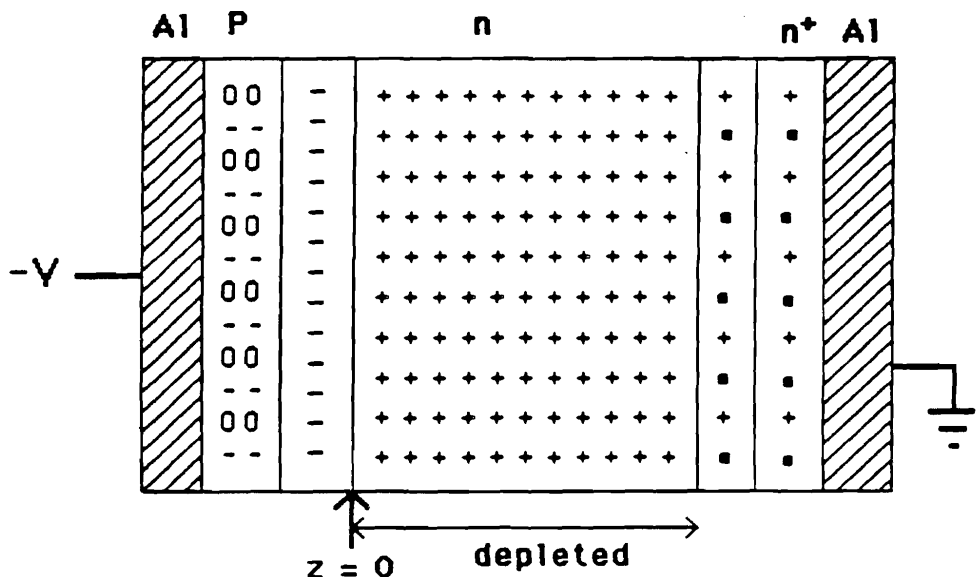
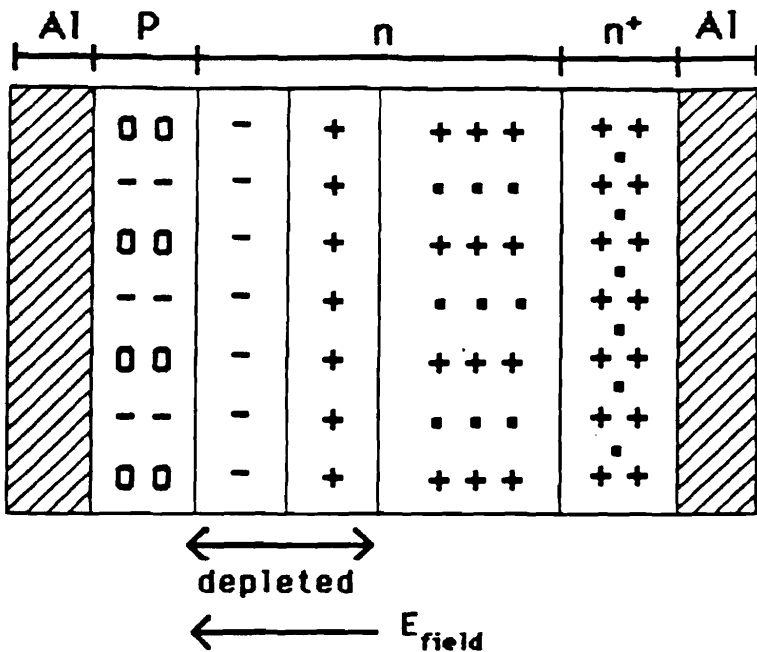


Figure 3.2(a),(b) Charge distributions in a p-i-n junction. (a) with no potential difference applied across the junction (b) with a reverse bias voltage applied across the junction. In this diagram, the open circles (boxes) represent holes (or electrons). The plus and minus signs represent positive and negative lattice ions, respectively.

hole pairs or 3.8 femtocoulombs of each charge as it passes through a $300\mu m$ thick silicon detector. The electric field of the depletion zone causes the electrons to drift towards the n side and the holes towards the aluminized strips on the p side. Although the holes have a larger effective mass than the electrons and thus a smaller mobility ($500 \frac{cm^2}{V - s}$), they can drift to the p side and be collected in less than 10 nsec. As in drift chambers, the cloud of holes spreads out as it drifts towards the strip. Since the drift distance is short, this is not a significant limitation; the width of the charge cloud at the collected strip is only about 2 microns. Due to the large interstrip resistance, each track produces a single hit in each plane it traverses: more than 90% of all hits are isolated. Occasional two hit clusters are due to large angle tracks and delta rays.

3.2.3 Fabrication of detectors

A description of the basic steps in the fabrication of an SMD plane is useful in understanding microstrip detectors. The steps of this process which we describe below all take place under clean room conditions. A pure high resistivity ($2k\Omega - cm$) n type Si wafer is manufactured by the zone refining process. It is important to use high resistivity silicon so that the detector can be fully depleted at reasonable voltages ($V_{deplete} \propto 1/\sqrt{\rho}$). Purity of the wafer is also essential to ensure long carrier lifetimes i.e. electrons and holes must not recombine at impurity sites before they are collected at the strips.

The wafer is baked at about 1040^0 C in a laminar oxygen flow,

to produce a thin layer ($\sim 0.2\mu m$) of SiO_2 . The silicon dioxide forms a protective coating against impurities and is a good electrical insulator between strips in the final detector (the interstrip resistance is greater than $1 \text{ G } \Omega$). Using a mask, $50\mu m$ pitch strips are etched on the upper face by standard photolithographic techniques. The crystal is aligned at an angle of 10^0 from its $[1,1,1]$ axis to avoid channeling effects in which the ions are preferentially implanted along certain axes. Boron atoms are then accelerated to 15 KeV, filtered by a mass separator and implanted onto the upper face of the wafer at a density of $5 \times 10^{14}/\text{cm}^2$. Arsenic atoms are deposited onto the bottom face at 30 KeV with a density of $5 \times 10^{15}/\text{cm}^2$. To repair the defects in the crystal structure caused by the ion implantation stage, the wafer is annealed at 600^0 C for 30 minutes. A thin ($1\mu m$) layer of aluminium is deposited onto the upper face and then etched with another mask to make strips. The aluminium provides electrical contacts for the strips. The rear face is uniformly aluminized so that a bias voltage can be applied. A schematic of the final detector is shown in Figure 3.3.

The typical $300 \mu m$ detector thickness is determined by the conflicting requirements of adequate charge collection, low detector capacitance ($C \sim 1/d$), and small multiple scattering errors ($\theta_{\text{scatt}} \sim \sqrt{d}$).

3.2.4 Characteristics of the E691 detectors

The silicon telescope of E691 is located 2.7 cm downstream of the edge of the Be target. It contains a total of 9 planes grouped in triplets; the

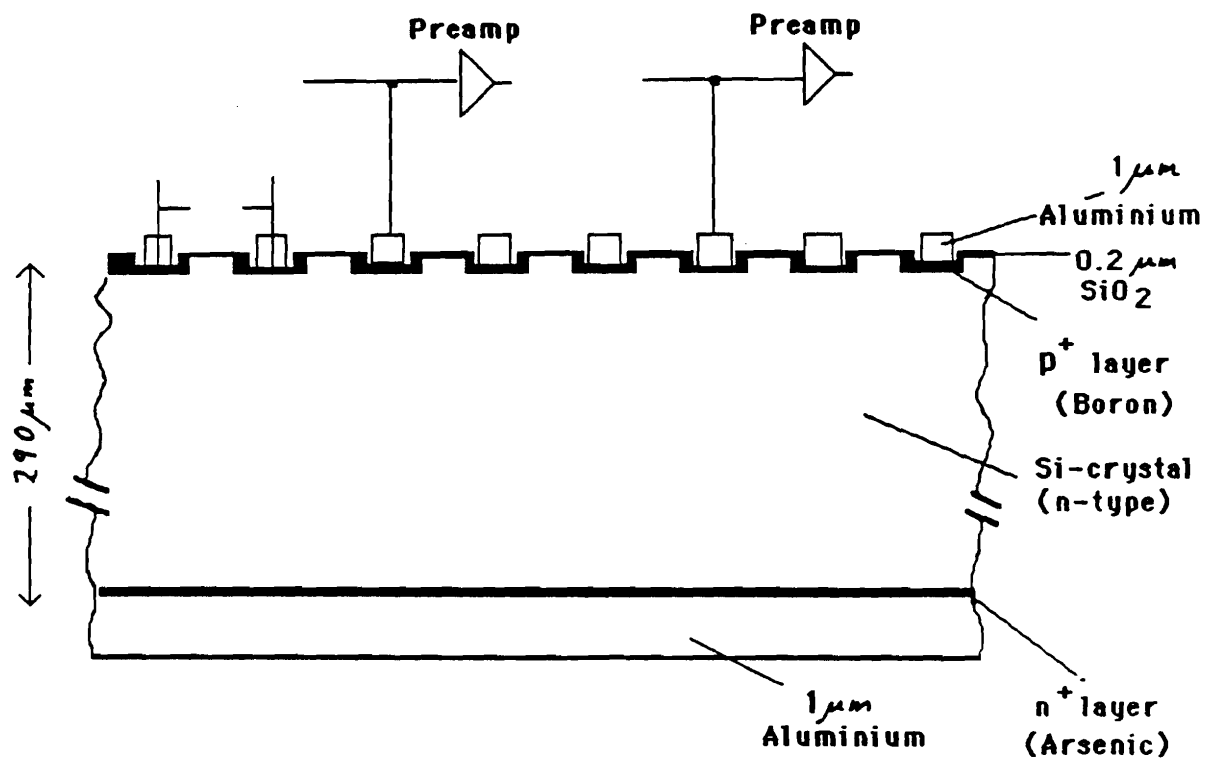


Figure 3.3 Cross-section of a silicon microstrip plane

intertriplet spacing is 8 cm. The planes of the first triplet have an active area of $2.6 \times 2.6 \text{ cm}^2$, while the planes of the second and third triplets have active areas of $5.0 \times 5.0 \text{ cm}^2$. To maintain a constant angular acceptance*, some of the outer strips of the second triplet are not instrumented. The telescope intercepts all tracks within an angular cone of ± 100 milliradians.

The first triplet was manufactured by Enertec - a division of Schlumberger. The second and third triplets were built by Micron Semiconductor, a small British firm. A summary of the detector properties and the z positions of the detector planes is given in Table 3.2.

All the detector planes have $50\mu\text{m}$ pitch and roughly $30\mu\text{m}$ strip width. The detector thicknesses varied from $297\mu\text{m}$ to $342\mu\text{m}$. The Enertec detectors were fully depleted at a bias of 90 Volts. For the Micron planes, the depletion voltage was somewhat lower, about 70 Volts. In order to reduce leakage currents, this voltage was ramped; it maintained its full value only during the 20 second accelerator beam spill.

The detector strips on the Enertec planes were fanned out directly to a printed circuit pattern on a kapton sheet. The connection between the kapton fanout and the detector was wire bonded (wire bonding is an ultrasonic bonding technique). The outer edge of the kapton sheet provided connections to the first stage of electronics i.e. preamplifiers. The strips on the Micron planes were wire bonded to a copper plated G-10 circuit pattern and then fanned out to thin kapton strips which provided extra mechanical flexibility for the connection to the hybrids.

* financial constraints were also relevant here

Table 3.2 Properties of the E691 SMDs (adapted from [Ra87])

Triplet	1	2	3
dimensions (cm)	2.6 × 2.6	5.0 × 5.0	5.0 × 5.0
pitch (μm)	50	50	50
thickness (μm)	~ 300	~ 300	~ 300
instrumented strips per plane	512	768	1000
plane ordering	X,Y,V	Y,X,V	X,Y,V
z positions at center (cm)	1.931,3.015, 6.684	11.046,11.342, 14.956	19.915, 20.254, 23.876

The Enertec detectors and assembly were mounted inside aluminium boxes, while the Micron planes were mounted inside copper coated stesalite boxes *. Both types of housing are designed as Faraday cages; that is to provide shielding from the ambient rf noise. The housings were also light tight. This last consideration is important because p-i-n diodes are excellent optical detectors.

A modified version of a high precision alignment technique developed at CERN was used to ensure that the strips in different planes are parallel. This essentially eliminated the need for multiplicative calibration constants in the SMD reconstruction. A computer controlled milling machine, which can produce parts to a tolerance of $12\mu m$, was used to fabricate mounting rings with two reference points. The strips were then aligned relative to a $75\mu m$ diameter wire and then glued onto the mount-

* stesalite is a composite epoxy fiberglass material similar to G10.

ing ring. The relative interplane rotational offset, in the x-y direction, which is a measure of the degree to which the strips are parallel, was found to be less than 1 milliradian. To ensure the stability of the relative intertriplet positions and simplify the alignment, the triplet assemblies were mounted on two rectangular granite bars (which are optically flat and have small thermal expansion coefficients).

3.2.5 SMD Readout

The most difficult problem in a practical SMD system is extracting signals from the strips of the silicon wafer and matching the density of the readout electronics to the density of the detector strips. The first component of the readout is a preamplification stage. The small signals typical of SMDs are fanned out from the strips and integrated by hybrid current sensitive preamplifiers. The term "hybrid" means that the device uses a combination of integrated and discrete components. In this case, the transistors and capacitors are discrete surface mounted components whereas the resistors are of the integrated thick film type. The device density in a hybrid circuit is greater than a PC board but less than an LSI.

These preamplifiers must be located as close as possible to the detector to minimize the capacitance of the readout; the equivalent noise charge of the readout is proportional to $\sqrt{C_{\text{readout}}}$ [Rad87]. We used 4 channel Laben (model MSD2) hybrid preamplifiers based on a design by Jarron et al[Ja84]. These preamplifiers employ bipolar microwave transis-

tors, rather than the usual FETs. They can operate near 1 GHz and have sufficiently low power consumption ($\sim 15mW/\text{channel}$) and good heat dissipation for operation in a tightly packed environment (however there is a tradeoff: although FET based devices are slower, they have much better signal to noise characteristics). The MSD2 has a current gain of ~ 200 and a risetime of ~ 3 nsec. The integration time is between 10 and 25 nsec. The MSD2 has an equivalent noise charge of about $1600 e^-$, which should be compared to the expected charge of $24000 e^-$ deposited by a normally incident minimum ionizing particle.

The second stage of the readout is of the discriminator-shift register or digital type, thus it was important for the first stage of readout electronics to provide a homogeneous response to detector signals. To ensure uniformity in the gains of the hybrids, a test setup was built by the UCSB electronics shop. The gain of each hybrid channel was individually tested; 10% of the hybrids were rejected either because the gain was outside of the two standard deviation tolerance* or because a channel was defective. The hybrids were mounted in silver plated aluminum boxes or "card cages" which provided rf shielding. The card cages were attached to the edge of the aluminium box which contained the detector. Each card cage contained 32 preamplifier cards. Even and odd numbered strips were read out on opposite sides of the detector. This was necessary because the wire bond technology available in 1985 required that the bonds be separated by $100\mu m$. In addition by separating the readouts for adjacent

* The gain was set to an accuracy of about $\pm 5\%$.

strips, we reduced interchannel crosstalk and avoided the possibility of oscillations.

The preamplifier cards were packed with a linear density of 40 channels per inch. Nevertheless, even with this compact and dense readout, the surface area of the first stage of readout electronics is roughly 150 times larger than the active area of the silicon detector. The next stage of readout occupies a surface area another order of magnitude larger.

The $1mV$ signals at the output of the preamplifiers are transmitted by 4m long nine channel aluminum shielded cables to modified MWPC readout cards. These cables are essentially 28Ω transmission lines. (The impedance of the cables is matched to the impedance of the input to the readout cards). Only four of the nine channels in the cables were used for signals; the remaining alternating channels were grounded to reduce crosstalk. As an additional precaution to reduce noise, the aluminium shields of the cables shared a common ground with the preamplifier enclosures; the latter was copper plated and soldered to the ground of the detector box. To prevent channels from shorting out or breaking when these relatively fragile cables were compressed, a jungle gym like cable support structure was built to relieve stresses. The cables were also supported at the readout box.

For the second stage of amplification, we used modified 8 channel Nanosystem S710/810 MWPC discriminator cards packed into 20 readout boxes at a linear density of 11 channels per inch. These cards contain a dual differential comparator, an adjustable monostable delay chip, and a

shift register. The basic design of this standard type of readout card was modified to include: an initial inverting stage, and a variable resistor to adjust the value of the discriminator threshold.

To ensure the uniformity of response of the readout cards, (designed for MWPC signals, which are typically a factor of 25 times larger) a test setup which injected realistic 1mV signals into the readout cards was built by the University of Toronto electronics group. Technicians, secretaries, graduate students, and professors meticulously adjusted the variable resistors which controlled the values of the discriminator thresholds (to an accuracy of $\pm 5\%$) and the one shot delays for each of the 6840 channels. The discriminator thresholds were set at a level which corresponds to 0.4 times the average expected deposition of a normally incident minimum ionizing particle. This threshold was reasonably efficient for large angle tracks, but high enough to keep noise rates down to a manageable level (typically 1 noise hit per plane per trigger).

At the MWPC card, the positive signal from the preamplifier was inverted and delayed (while the one shot fired) by 750 nsec*. If the leading edge of the delayed signal was in coincidence with a 100nsec gate (this was called the "fast load") generated by the low level trigger ($B \bullet H$), then the delayed signal set a latch bit in the shift register of the readout card. When a high level (E_T) trigger was generated, the shift registers of the

* It is important to remember that using a one-shot to delay the signal deadens the readout for the 750nsec duration of the one shot pulse. This method of delaying the signal is however advantageous compared to using long cables, from both the logistical and financial point of view.

MWPC cards were read out serially by Camac Nanoscanner (WCS-300) modules and then cleared. If no high level trigger was generated, the latches were quickly cleared without being read out.

Six parallel Nanoscanner streams were used to read out the twenty boxes of MWPC cards. (The small memories of the Nanoscanner modules and the requirement of short digitization times* dictated the use of 6 parallel Nanoscanner readout streams.) The information from the latches in the MWPC cards is transferred to the memory of each nanoscanner and then in turn transferred to the data acquisition computer of the experiment via CAMAC. The nanoscanner readout is schematically described below.

After receiving a Start pulse from the high level trigger, the nanoscanner memory is cleared and the scanner begins the transfer of the latched data of the readout cards into itself. To accomplish this transfer, the scanner emits a train of clock pulses. For each pulse, the channel in the MWPC card steps the next bit onto the data line and then returns the clock pulse. The scanner automatically produces another clock pulse a fixed time interval later. Again, the next channel on the MWPC card to be digitized automatically places the next data bit onto the data line and pulses the clock return line. To monitor the integrity of the readout four fiducial bits are set by a special coupler card in each readout box. When the data arrives at the nanoscanner, the nanoscanner counts the number of clock pulses it has emitted and stores the wire number of any strip that was hit. Clusters of hits are compactified by storing only the wire number

* The nanoscanners operated at 5 MHz.

of the last wire hit and the cluster size.

The volume of electronics associated with silicon detectors is a major limitation. For instance, the minimally redundant vertex telescope of E691 required 1710 cables and 855 readout cards. There are, however, now efforts underway to integrate some portion of the readout onto the silicon chip, e.g. the Microplex chip [Ch84].

3.2.7 SMD Monitoring

The individual transistors of the readout cards and preamplifiers collectively consume a large amount of power (~ 6 kW). To supply the required amounts of power, we used about 20 high current POWER-ONE supplies. Ten miscellaneous low current supplies were used for the fine adjustment of the delay and of the threshold voltages on the MWPC cards. Outputs from these supplies were connected by shielded cables to two central power distribution panels (on the east and west sides of the detector) and then fanned out to each of the 20 readout boxes. To avoid downtime from power supply failure, we built a relatively elaborate monitoring system for these power supplies.

Individual cables from the ~ 30 power supplies were connected to a voltage monitoring panel. By turning a multiple throw switch, a physicist on shift, while performing a visual inspection of the experimental hall, could verify the values of the threshold and bias voltages on a mounted multimeter. In addition, an alarm module automatically rang a bell in the experiment control room if any output of a high current supply differed

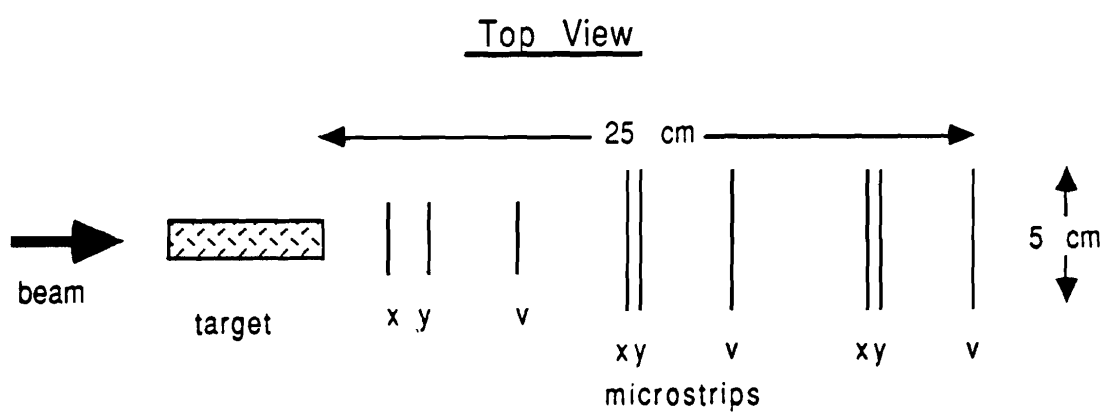


Figure 3.4 The vertex detector and target configuration

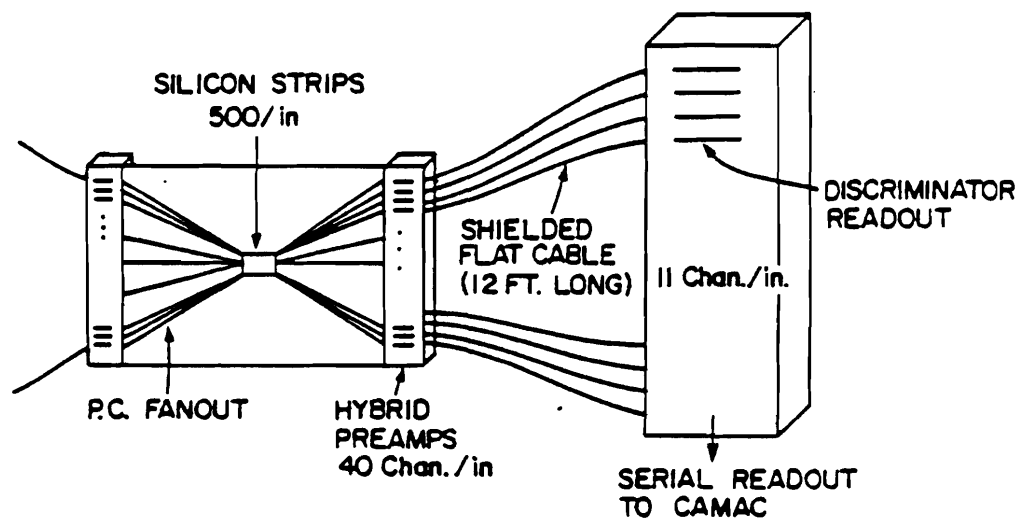


Figure 3.5 A block diagram of the SMD readout system

from its milestone value by more than ± 0.1 volts.

A complex online monitoring system (OLMS) was used to keep track of the quality of the data from the vertex detector and the other components of the experiment. Roughly 10% of all the events recorded were transferred from the data acquisition computer, a PDP 11-70, and made available to a VAX 11-780 dedicated to monitoring tasks. These events were placed in a global common block, that is a common block simultaneously accessible to many independent monitoring processes. Programs in the OLMS accumulated histograms, collected scaler records and calibration constants, and generated software alarms in cases in which detectors required special attention.

The software monitoring of the SMD system provides a typical example of the application of the OLMS in E691. The voltages which control the thresholds and delays of the MWPC cards were digitized by slow ADCs (read out only at the beginning and end of accelerator beam spills). Alarm displays on the VAX were generated if the recorded voltage from these supplies deviated from its expected value by more than ± 0.02 volts. During the later part of the run, the SMD leakage currents were also digitized by slow ADCs and generated software alarms if they went out of range.

To verify that the SMD system was functioning correctly, a number of programs in the OLMS constantly checked the quality of the SMD information. These checks included: the number of noise hits per plane, the presence of the scanner id word that is generated at the beginning

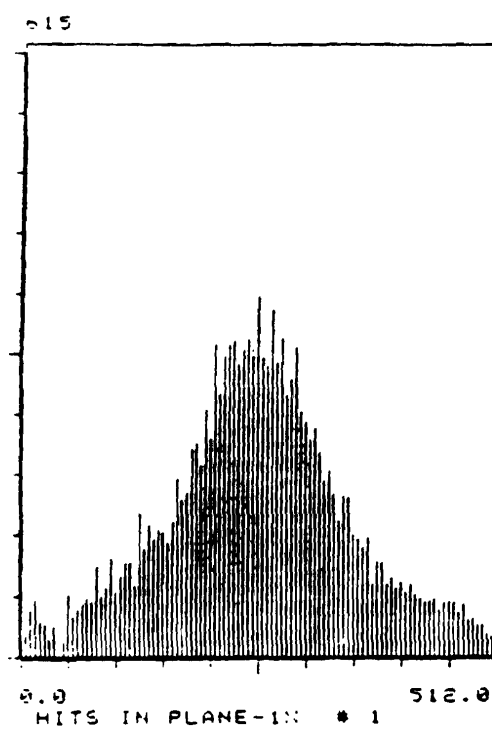
of the readout of each Nanoscanner and the fiducial bits which delineate the readout boxes in the readout chain of each scanner, as well as the average per plane tracking efficiency as determined from a partial reconstruction. Large deviations from the milestone values for these quantities were flagged on the alarm display. Beam profiles were another useful check of the SMD data. These high statistics plane by plane and scanner by scanner participation plots, usually showed the gaussian profile of the beam (see Figure 3.6) and quickly revealed problems in the SMD readout chain. When the beam was unstable, the SMDs were also an excellent tool for beam tuning.

3.2.8 Leakage Currents, Radiation Damage, and Other Problems

One problem encountered during the run was overheating of the preamplifier electronics and the readout electronics during the muggy summer months in Illinois. In order to dissipate heat and reduce noise rates, large boxer fans were directed onto the open faces of the readout boxes. A heavy duty Sears airconditioning unit also blew cold air onto the detector through an insulated tube. If the temperature on the copper housing of the second triplet rose above 60^0 F, an alarm was set off in the experiment's control room. The leakage currents in the detector also exhibited a strong dependence on the ambient temperature; this is to be expected since $I_{leak} \propto e^{-E_g/kT}$.

Radiation damage can adversely effect the performance of silicon

74



486

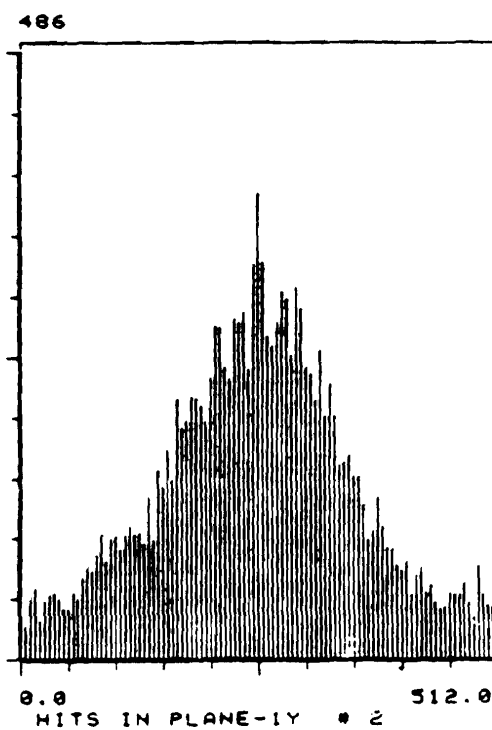


Figure 3.6 SMD beam profiles

detectors. Consequences include: increases in leakage currents, the creation of defects or trapping centers which decrease the amount of charge collected. It has also been shown that radiation damage can change the charge donor concentrations, which may in turn distort the drift field of the wafer and shift the center of gravity of the collected charge distribution [Di87].

The SMD planes in E691 suffered very little radiation damage in the course of the run. Each detector plane was connected in series with a measurement resistor; therefore when the leakage current from the detector increased, the effective voltage across the detector decreased. To compensate for the reduction of charge collected due to this effect, the depletion voltages were gradually increased. We found that a decrease in the leakage currents occurred when the beam was off for several days. As noted earlier, the depletion voltage was also ramped. The most severe radiation damage occurred in the Enertec planes; for these planes the leakage currents rose from 2 nA/strip to 90 nA/strip during the course of the run, probably from surface effects due to the method of fabrication. The total integrated dose received by these detectors was only 5×10^{11} electrons. In contrast, the Micron planes which were exposed to a comparable flux, sustained no radiation damage. Indeed, it has now been well established that properly fabricated silicon detectors can sustain doses of radiation (up to 1 MRad) that are at least two orders of magnitude larger than the dose received in E691 before any substantial degradation in their performance can be observed [Di87].

3.2.9 Resolution and Other Figures of Merit

The resolution in the direction perpendicular to the beam in a position sensitive detector, like the SMD, is given by:

$$\sigma_{intrinsic}^2 = \frac{\int_{-d/2}^{d/2} x^2 dx}{\int_{-d/2}^{d/2} dx} = \frac{2(d/2)^3}{d} = \frac{d^2}{12}$$

where d is the strip pitch. Thus the intrinsic transverse position resolution of a single plane is given by the strip width divided by $\sqrt{12} \sim 50\mu m/\sqrt{12} \sim 14\mu m$. The measured value in E691 is $16\mu m$.

Two types of effects limit the resolution on the track intercept. The first is due to intrinsic strip resolution; the size of this resolution ($\sigma_{intrinsic}$) is determined primarily by the strip pitch. The second limit is due to errors on the backwards projection of tracks in the vertex telescope; this limit has components from multiple scattering ($\sigma_{multiple}$) and from errors on angular projections ($\sigma_{angular}$).

The theoretical limit to SMD resolution is not determined by the strip pitch. Fluctuations from delta rays and charge diffusion can shift the center of gravity of the charge distribution by as much as $1 - 3\mu m$. In most experiments, however, multiple scattering imposes much more severe practical limitations, especially for low momentum tracks. For reconstructed tracks in E691 which pass the pattern recognition cuts, we find that the error on the track intercept is given by:

$$\sigma^2 = \sigma_{intrinsic}^2 + \sigma_{multiple}^2 + \sigma_{angular}^2$$

where $\sigma_{intrinsic} \approx (16)\mu m$ and $\sigma_{multiple} = \frac{50\mu m}{p(GeV)}$. The last term

is the error due to angular resolution: $\sigma_{\text{angular}} \approx \frac{\sigma_{\text{intrinsic}}^2}{3} \frac{L_1^2}{L_2^2}$ (where L_1 is the distance from the first triplet to the secondary vertex and L_2 is the length of the vertex telescope). In this experiment $\frac{L_1}{L_2}$ is typically about 0.25, so that the term due to σ_{angular} can be neglected. From the above expression for the error on the intercept, we find that multiple scattering makes a significant contribution for tracks with momenta below 5 GeV. The material in the vertex detector is usually the largest contribution to this multiple scattering error. Although our 2" beryllium target is 14.2% of a radiation length while the nine planes of silicon detectors in E691 present only 2.9% of a radiation length and 0.63% of an interaction length, the lever arm for multiple scattering from the silicon planes is about a factor of six times longer than the lever arm for multiple scattering in the target.

The two track resolution for our experiment is roughly given by the strip pitch ($\sim 50\mu\text{m}$); this is sufficiently fine to separate most tracks in the first few planes. In typical charm events, there are on average about 2 tracks which lie within $50\mu\text{m}$ at the first X plane and about 0.5 tracks which overlap to this precision at the second X plane [Kum86]. In experiments which use charge division readout schemes, the two track resolution can be considerably worse than the strip spacing.

From reconstructed tracks, we have determined that the per plane efficiency is $\sim 95\%$. The small inefficiency is dominantly due to a small number of dead strips and non-functional readout channels. It is worth

noting that the efficiency of an SMD plane is strong function of the angle of incidence of a track. For instance, with a low setting of the threshold on our discriminator readout (0.48 mV) that is fully efficient for normally incident tracks¹, we find that at an angle of 90 milliradians, near the edge of the acceptance of the vertex telescope, the track detection efficiency falls to 79% of its maximum value [Ka85]. This reduction in efficiency occurs because the charge deposited at high aspect ratios may be shared among several strips.

3.2.10 Additional uses of the vertex detector

The reconstructed information from the SMDs was primarily intended to be used to separate and identify the tracks from the charm production and decay vertices in physics analysis. We discovered that the low noise rates, high efficiency, and fine resolution of the SMDs can also form the basis for a pattern recognition algorithm in the charged track reconstruction. Instead of beginning the track reconstruction in the region of lowest track density, downstream of the second bend magnet, and then projecting the found track segments upstream towards the target, an algorithm [due to G. Hartner] finds track segments within the higher resolution SMDs and projects them downstream. The projection using this method is accurate to better than one drift chamber cell. In addition, this method reduces the combinatorics of track finding within the relatively noisy drift chambers. A single SMD track segment and a good

¹ This value of the threshold was used in test beam studies, the setting in E691 was lower and thus more efficient for tracks at large angles.

drift chamber triplet are sufficient to pin down a track. This algorithm is both fast (~ 300 ms/event on a CYBER 175) and efficient (85% of the reconstructable tracks can be found with this algorithm).

A second tracking program written by M.J. Losty marks off SMD hits and drift chamber space points already used in the first tracking pass and searches for the remaining 15% of reconstructable tracks. This second tracking pass reconstructs strange particles (e.g. 90% of K_s decays occur downstream of the vertex telescope) which leave no traces in the SMDs and a small number of tracks missed in the first pass.

A less obvious application is then the use of the vertex telescope as a veto for long lived neutral strange particles. Since the SMDs are very efficient and most K_s^0 and Λ particle decays take place downstream of the last SMD plane, the requirement that the neutral decay leave no tracks in the vertex telescope significantly reduces the background to such decays as $K_s^0 \rightarrow \pi^+ \pi^-$.

3.3 Magnets

Two large aperture copper coil magnets provide a 530 MeV/c momentum kick to charged particles for momentum analysis and pattern recognition. The magnetic fields are in the - y direction and deflect positive particles towards the west side of the spectrometer. The angular acceptances of the magnets are ± 240 mrad in the horizontal direction and ± 120 mrad in the vertical direction for M1 and ± 120 mrad and ± 60 mrad for M2, respectively. According to Monte Carlo design studies, for

typical charm decay modes, 95% of the secondaries with $p > 5$ GeV lie in a cone of ± 110 mrad. Similarly, roughly 95% of the secondaries with $p > 15$ GeV will be produced in the angular cone ± 62 mrad. The spectrometer thus has two sections with good acceptance and resolution for both low and high momentum decay products. Detailed properties of the magnets are given in Table 3.3.

Table 3.3 Properties of the E691 magnets [adapted from Su84]

Magnet	M1	M2
Name	Akhennaten	Beketaten
center (cm)	286.6	620.6
length (cm)	165	208
entrance (cm)	154 \times 73	154 \times 69
exit (cm)	183 \times 91	183 \times 86
current (amps)	2500	1800 *
p_T kick	212.4 MeV/c	320.7 MeV/c
$\int B dl$	-0.71 T-m	-1.07 T-m

* There are four coils in M2 as compared to two in M1. Hence we achieve a higher field with a lower current.

The values of the magnet currents were chosen because accurate field maps at these values of the magnet currents were available from experiment E516. In addition, on the basis of Monte Carlo studies, the higher values of the field strengths were found to be close to optimal for the energies anticipated in E691. The E516 field maps were made using the Fermilab Ziptrack magnet mapping system. The Ziptrack consisted of

three mutually perpendicular rectangular coils mounted on a cart. As any of the coils passed through a region of varying magnetic field, the changing magnetic flux induced a voltage in the coil. The induced voltages and positions of the coils are digitized by an ADC and recorded by a PDP-11 minicomputer. Several million magnetic field points were recorded and fit to a sum of orthogonal polynomials consistent with Maxwell's equations [Su84].

3.4 Drift Chambers

Four drift chamber stations (D1,D2,D3,D4) with a total of 35 planes were used for the downstream tracking and momentum analysis. D1 is located upstream of the first bend magnet and provides an initial measurement of the track trajectory. D1 is used to pin down poorly constrained SMD track segments and to eliminate phony track SMD track candidates. D2 is located between the first and second bend magnets; it provides the first space points and track segments after the momentum separation of particles. Since the copious pairs characteristic of photo-production are spread out by M1 into a thin band in the x direction, a thin band about ± 1 cm wide in the vertical direction and ± 10 cm in the horizontal direction in the central region of D2 is quite inefficient (the efficiency is reduced by 5-40%, depending on the particular assembly) *. The third set of chambers D3 is located downstream of the second bend magnet and provides additional space points and additional segments for tracks

* this is referred to as the "D2 hole" .

which are fast enough to have passed through both magnets. The last chamber D4 is located next to the electromagnetic calorimetry. Despite its long lever arm, due to extra hits from the albedo of electromagnetic showers and due to hardware problems, this chamber was inefficient and had much poorer resolution ($\sim 800\mu\text{m}$) than D1-D2-D3 .

The drift chamber planes are grouped into assemblies; where an assembly is a set of planes which completely determines the x, y, and z coordinates of a single point on a charged particle trajectory. Recall that each drift chamber hit has an associated left-right ambiguity since the time information gives no clue as to whether the charge cloud drifted to the wire from its left side or from its right side. Thus a fully determined (x,y) coordinate requires measurements from planes in three views (X,Y, and V) and is referred to as a "triplet".

The assemblies downstream of M1 consist of sets of X, U, and V planes, where the U and V planes are tilted $\pm 20.5^0$ from the vertical direction. The assemblies in D1 contain U, V, X, and X' planes. X' planes are identical to X planes but are offset by half a cell size relative to the X planes, in order to resolve left-right ambiguities in the region of highest track density.

The sense planes consist of alternating sense and field wires, designed so that the equipotentials are cylinders centered on each sense wire (in the close vicinity of each wire). The sense planes are stacked between cathode planes held at high negative voltage (typical values are -2.1 kV). Within each assembly, the sense planes are separated by 1.588 cm in the

z direction. The cathode planes are separated by the same amount. In D1-D2-D3, the field wires are held at voltages which are $0.4 - 0.6$ kV higher than the voltages of the cathode planes, while the sense wires are grounded. In D4, in contrast, the sense wires are held at high voltage, whereas the cathode planes are grounded. These field configurations are used to obtain an electric field which is roughly constant along the drift path, except for the region of charge amplification near the sense wire.

We choose a gas mixture which contains equal parts of argon and ethane. This choice yields a drift velocity which is nearly independent of the electric field strength. A 1.5% admixture of ethanol is added for quenching and to prevent chamber aging [Es86]. The gas is held at slightly above atmospheric pressure. The chambers operated with a gas gain of 2×10^5 and with a typical drift velocity of $40\mu\text{m/ns}$ [Me86].

The drift chambers were read out using 16 channel Lecroy DC201 and Nunamaker N-277C amplifier discriminator cards. The CAMAC 4290 TDC system was used for time digitization. This TDC system is equipped with an "external autotrim" feature which automatically subtracts the relative time offset due to cables and chamber electronics. The 4290 system has a crate controller for data formatting and transfer as well as a large (4000 16 bit words) buffer. The individual 4291 TDCs also provide uniform gains to within $\pm 0.1\%$, thus eliminating the need for gain calibrations. A detailed discussion of the drift chamber logic and pulsing scheme can be found in [Me86]. The absolute time offsets, which are due to the differences in z positions of the chambers, are determined by min-

imizing the residuals of reconstructed straight muon tracks produced at the upstream proton target [Ra87].

A summary of the drift chamber properties is given in Table 3.4. Note that the cell sizes increase linearly as function of the distance from the target. Thus the average hit density in each drift chamber cell is constant for each of the stations. The typical chamber resolution of $300 \mu\text{m}$ implies that the extrapolation error on the x or y intercept of a track at the target is $O(2-3 \text{ cm})$ or the size of a silicon detector.

Table 3.4 Properties of the E691 Drift Chamber System

Station	1	2	3	4
dimensions (cm)	160×120	230×200	330×200	550×300
cell size* (cm)	0.446	0.953	1.588	3.18
z position (cm)	154-195	382-501	928-1048	1738-1749
No. of assemblies	2	4	4	1
No. of planes	8	12	12	3
Resolution μm	350	300	300	800

* The cell sizes of the U and V planes are equal to $\cos(20.5^\circ)$ times the cell sizes in the table. The numbers quoted in this table are the full cell sizes.

The typical per plane efficiency for events with clean isolated tracks is about 90% **. Thus the probability of measuring a triplet is $\sim (0.9)^3 \sim 70\%$. In addition, due to the high noise rates in the chambers, there are

** We measure our per plane efficiency using reconstructed tracks. The numerical value of the efficiency is the fraction of time a track passing through a given plane gives a hit in that plane.

typically 10 to 100 phony triplets for each real triplet in an assembly. It is therefore essential to have a large number of redundant planes in order to achieve good tracking efficiencies. It should be noted that the actual per plane efficiencies in the more congested Et data, including the reconstruction program efficiency, were $\sim 90\%$ in D1 planes, $\sim 80 - 88\%$ in D2 and D3 planes, and $\sim 47 - 65\%$ in D4 planes [Me86]. An additional measure of tracking efficiency is the ratio of the reconstruction efficiency for $D^0 \rightarrow K^-\pi^+$ to the reconstruction efficiency for $D^0 \rightarrow K^-\pi^+\pi^-\pi^+$, which is roughly 50%. As a rule of thumb, due mostly to the effect of spectrometer acceptance, the full detection efficiency for each additional pion is therefore about 70%.

The charged track reconstruction program (PASS1) categorizes tracks by setting bits in the variable JCATSG. The first bit in this variable indicates whether the track passed through the field free region (either the SMDs or D1 or both). The second and third bits indicate whether the track passed through D2 or D3, respectively. The fourth bit is set if the track passed through D4. The fifth bit is used to mark spurious tracks. For instance category 3 ($3 = 2^0 + 2^1$) tracks must have passed through D1 and D2 or the SMDs and D2. Similarly, category 15 tracks have passed through all four sections of the spectrometer.

The momentum resolution of the detector is a crucial measure, in addition to the efficiency, of the quality of the tracking. In general,

neglecting multiple scattering, the momentum resolution is given by:

$$\frac{\Delta p}{p} \approx \frac{p}{0.3 \int B dl} \sqrt{\sigma_1^2(\theta_1) + \sigma_2^2(\theta_2)}$$

where $\sigma_{1,2}(\theta_{1,2})$ are the angular resolutions before and after the magnet field. The contribution to the angular resolution from detector resolution for N measurement points, with intrinsic error δ , and spacing L is equal to $\frac{\delta}{L} \sqrt{\frac{12}{N}}$. From these considerations we see that the momentum resolution improves dramatically if the particle receives a larger transverse momentum kick. It also improves somewhat if more measurement points are available $\sim 1/\sqrt{N}$. For two magnet tracks (categories 7 and 15), the measured momentum resolution is: $\frac{\Delta p}{p} \approx 0.05\% p + 0.5\%$. For 1 magnet tracks (category 3), the measured resolution is: $\frac{\Delta p}{p} \approx 0.1\% p + 0.5\%$. The second contribution of 0.5% is due to multiple scattering. For category 1 tracks, which are not tracked through the first magnet, but are bent in the fringe field of the first magnet, $\frac{\Delta p}{p} \sim 6\% p$.

The mass resolution is determined by the resolution on the momenta of the decay products and the resolution on the opening angle between the decay products:

$$\frac{\delta m}{m} \sim \frac{1}{2} \sqrt{(\delta p_1/p_1)^2 + (\delta p_2/p_2)^2 + 4(\delta\theta_{12}/\theta_{12})^2}.$$

The mass resolution is usually dominated by the momentum resolution. We find that the spectrometer achieves a 27.4 MeV mass resolution at the J/ψ mass for the dilepton mode $\psi \rightarrow \mu^+ \mu^-$ and a 10.3 MeV mass resolution at the D mass for the mode $D^0 \rightarrow K^- \pi^+$ [Cr87]. For $K_s \rightarrow \pi^+ \pi^-$ decays, 90% of which give no tracks in the SMDs system, the mass

resolution is ~ 4.4 MeV. The small fraction of K_s decays which are also tracked in the SMD system have slightly better mass resolution (from the track segment before the magnet).

3.5 Cerenkov counters

Two segmented threshold gas Cerenkov counters (C1 and C2) are used to distinguish kaons and protons from the abundant pions produced in hadronic events. The most upstream counter, C1, is located partially inside the second bend magnet and is filled with nitrogen. C2 is located downstream of the third drift chamber station D3 and is filled with a mixture of 80% He and 20% nitrogen. The different dielectric properties of the gases allow the counters to be operated in the threshold mode. The threshold momenta for several types of particles are given in Table 3.5.

From Table 3.5, we can very roughly determine the ranges in which various types of particle identification are possible when operating the counters in a digital (on-off) identification scheme. For instance, in the momentum range between 5.6 and 20 GeV, pions can be distinguished from protons and kaons, but kaons and protons cannot be separated. In the momentum range of 20 to 37 GeV, all three types of particles can be uniquely identified. Between 37 GeV and 70 GeV, only protons can be identified. Using the momentum dependence of Cerenkov radiation and the pulseheights from the counters, the reconstruction refines these rough conclusions.

The lengths of the counters were determined by the requirement

Table 3.5 Threshold Momenta (in GeV) for the E691 Cerenkov counters.

Counter	e	μ	π	K	p
C1	0.02	4.2	5.6	20.0	37.7
C2	0.04	7.9	10.4	37.0	69.8

that a typical particle produce an average of 10 photoelectrons in order to be detected. The number of photons produced per unit length is proportional to $\sin^2 \theta_c$ (where θ_c is the Cerenkov angle). For pions, θ_c in C1 is 24 milliradians whereas θ_c in C2 is only 13 milliradians, thus C2 must be roughly twice as long as C1.

The fineness of the Cerenkov counter segmentation is determined by the conflicting requirements that the number of overlapping Cerenkov rings be minimized and the ring from a single particle be completely collected in a single mirror (and therefore in a single phototube). We choose a 28 cell segmentation of C1 and a 32 cell segmentation of C2. In the central region of the counters, where the density of tracks is the highest, the segmentation is the finest. Typical mirror sizes range from 15.0 cm \times 25.0 cm in the center of C1 to 95.0 cm \times 50.0 cm in the outer part of C2. The maximum radii of the Cerenkov rings (which are produced by the focussing action of the curved mirrors) are 8.4 cm in C1 and 8.7 cm in C2. With this segmentation, the central mirrors in C1 contained two or more overlapping tracks in 7%-11% of events, while the outer mirrors contained overlapping tracks in less than 2% of events. In C2, a typical

Table 3.6 Properties of the E691 Cerenkov counters

Counter	C1	C2
Gas	100% N_2	80% He 20% N_2
θ_c (mrad)	24	13
$n - 1$ ^a	2.9×10^{-4}	8.6×10^{-5}
Length (m)	3.7	6.6
Z (mirror plane) (cm)	866	1653.4
No. of cells	28	32

a Recall the threshold momentum $p_{th} \sim \frac{mc}{\sqrt{2n-1}}$

central mirror contained overlapping tracks for 3%-7% of the events, in the outer mirrors less than 1% contained overlaps.

The cone of Cerenkov light produced by a particle traversing one of the counters is reflected by a curved mirror into a conical light collecting structure called a Winston cone to which a sensitive phototube is attached.

The mirrors are slumped from window pane glass and then are coated with aluminum. A manufacturing process was devised, by the University of Colorado group, to ensure that the reflectivity of the mirrors remained high in the peak region of Cerenkov light (recall $dN/d\lambda \propto 1/\lambda^2$) [Ba86]. The mirrors were coated, using a standard thin film deposition process, at a high vacuum $\sim 10^{-7}$ torr and using very short deposition times (~ 30 sec) to minimize the possibility of oxidation. Typical reflectivities were measured to be 85% at 2525 Å.

The Winston cones are designed to intercept rays reflected from

the mirrors that enter its aperture at an angle of less than 20^0 . Rays which enter at higher angles will exit, after multiple bounces, through the entrance of the Winston cone. These cones are made of nickel and plated with a 1000 Å thick layer of high reflectivity aluminum, which in turn was coated with a 100 Å layer of magnesium fluoride to avoid oxidation of the aluminum surface.

High gain RCA 8854 5" phototubes are attached via an intermediate acrylic cylinder to the Winston cones. These phototubes give an output pulse proportional to the initial number of photoelectrons. They are sufficiently sensitive, because of their high gain cesium gallium phosphide first dynode, so that the single photoelectron peak can be clearly distinguished from the pedestal. (The sensitivity of a phototube is determined by the sensitivity of its first dynode). To increase the detection efficiency for Cerenkov radiation which peaks at short wavelengths, the outer glass surfaces of the phototubes are coated with p-terphenyl (pTP), which absorbs light in the range 1600-2500 Å and reemits the light in the range 3500-5000 Å, where the phototubes are most sensitive. The phototubes were read out by LeCroy 2249 ADC modules. The typical number of photoelectrons collected per charged particle was about 12 in each counter; the phototube noise level corresponds to about 2 photoelectrons.

The space constraints of the spectrometer required a two bounce geometry for the C1 mirrors, as shown below. In addition, the phototubes were located in the fringe field of M2. Although the phototubes were shielded with a layer of soft iron and μ -metal, large stray fields (~ 2

Gauss) persisted in some of the phototubes. To alleviate this problem, we created compensating magnetic fields by passing a small current through coils of wire wrapped around the shields of the C1 phototubes.

In C2, the light is reflected directly into the phototube. This counter, however, contains helium, which diffuses easily through most barriers and can easily poison the high gain phototubes. A 0.6 cm thick Suprasil window with a rubber gasket is placed at the exit aperture of the Winston cone to prevent helium from leaking into the phototube. In addition, the space between the Suprasil window and the phototube is ventilated with nitrogen.

To shield the counters from the Cerenkov light produced by the copious flux of beam pairs, narrow strips of baffling were stretched at beam height across the counters. This baffles blocked off a strip about 3.8 cm wide in C2.

The thresholds and gains of the Cerenkov counters are calibrated using well separated high momentum tracks. Using these basic quantities, the reconstruction program subtracts the pedestal and determines the corrected pulse height. Pulse height predictions for the five possible particle identification hypotheses are determined; the drift chamber trajectory is divided into steps and the Cerenkov light is propagated to the phototube. A fit to the observed light distributions, assuming a slightly modified Poisson distribution, is performed, and a consistency probability is calculated for each mass hypothesis. This calculation includes the $(1 - p_{th}^2/p^2)$ momentum dependence of the light distribution, corrections

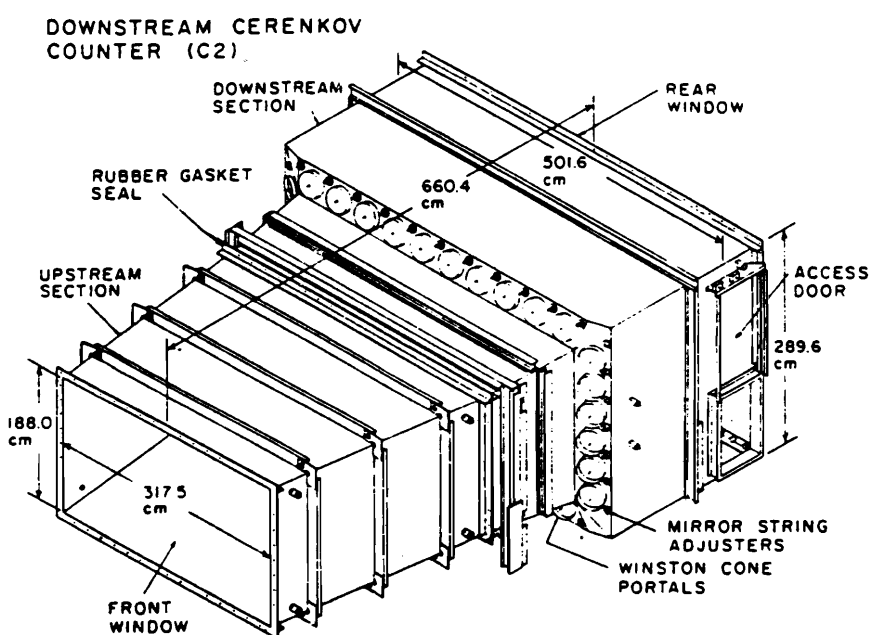
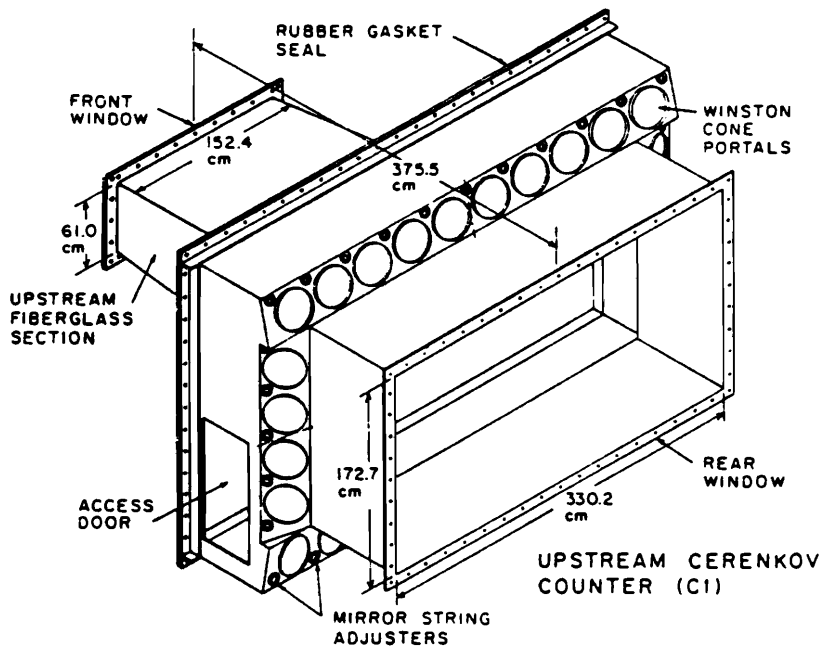


Figure 3.7 The Cerenkov counters C1 and C2

C1 MIRROR ARRAY								
13	9	2		10		14		
11	7	5	3	1	4	6	8	12
25	21	19	17	15	18	20	22	26
27	23		16		24		28	

C2 MIRROR ARRAY								
15	11	2		12		16		
13	9	7	5	3	1	4	6	8
29	25	23	21	19	17	20	22	24
31	27		18		28		30	32

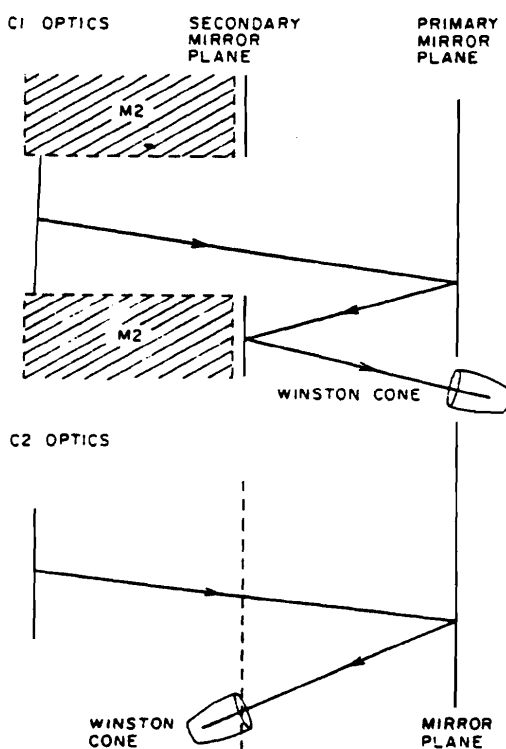


Figure 3.8 (a) Mirror segmentation in C1 and C2 (b) Light paths in C1 and C2

for the distortion of the Cerenkov ring into an ellipse as the charged particle bends in M2, gaps, and other sources of inefficiency in the mirrors and Winston cones. Electron identification and muon identification from the calorimetry are used to refine the predictions; fortunately the momentum spectra for electrons and muons fall off rapidly above 10 GeV and thus they are a relatively insignificant background.

For each track, the reconstruction program calculates a variable $CPRB2(i)$, $i = 1, \dots, 5$ which is the product of the consistency probability and an apriori probability. The consistency probability measures the agreement between the observed light levels and the predictions for each track. The apriori probability is simply the fractional content of particle type i in a hadronic event. The apriori probabilities for electron, muons, pions, kaons, and protons are 0.02, 0.01, 0.81, 0.12, and 0.04 respectively. The variable $CPRB2$ is normalized so that for each track, $\sum_{i=1}^5 CPRB2(i) = 1$. For roughly 15% of tracks, in which Cerenkov light from nearby tracks overlap completely, $CPRB2$ becomes the apriori probability.

In the analysis of a decay to an n -body final state, one typically imposes the requirement that the n fold product of the $CPRB2$ s for the n -body particle assignments lie above the apriori level. The efficiency of such a Cerenkov requirement is about 70% (e.g. $D^0 \rightarrow K\pi$) and reduces the background by a factor of 5. Occasionally, the wrong particle identification assignment is made. For instance, from the size of reflection peaks in the modes $D^0 \rightarrow K^-K^+$ and $D^0 \rightarrow \pi^+\pi^-$, we determine that with loose

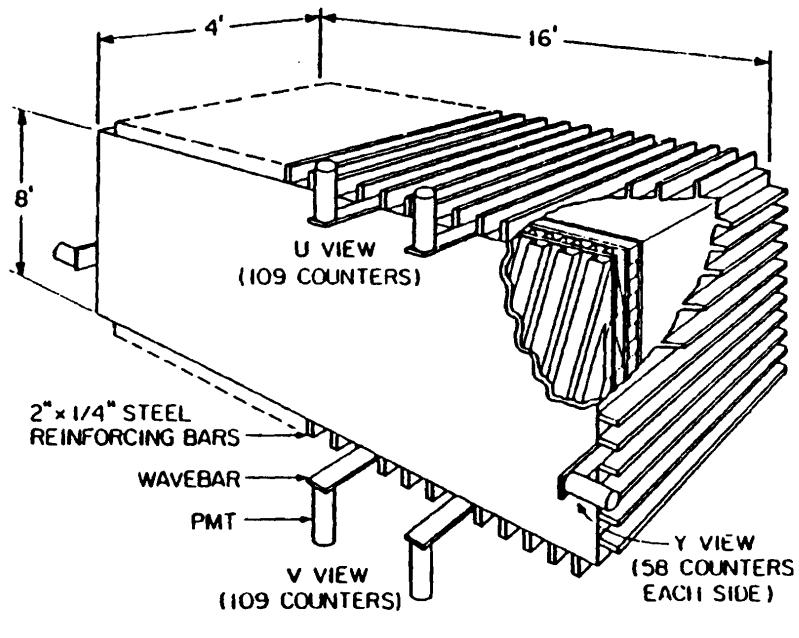
Cerenkov cuts the probability of misidentifying a pion as a kaon is about 5%, while the probability of misidentifying a kaon as a pion is about 30%.

3.6 The SLIC and the Pair Plane

The SLIC (where the acronym stands for "Segmented Liquid Ionization Calorimeter") is a finely segmented three-view electromagnetic calorimeter. Within a large tank, sixty layers of aluminum corrugations, lined with teflon, containing liquid scintillator (NE235A) alternate with teflon lined lead sheets. Light is transmitted by total internal reflection (since teflon has a lower index of refraction than scintillator) to wave shifters located on the top and bottom of the detector (or in the case of the Y view on the east and west sides of the tank). There are 109 channels in each of the three views. The U and V views are oriented at $\pm 20.5^0$ to the vertical. The scintillator channels are 1.25" wide in the central region and twice as wide in the less densely populated outer portions of the counter.

Waveshifter bars, which are made of lucite doped with BBQ, transform the scintillator light from the blue to green and integrate the electromagnetic shower along the longitudinal direction of the beam. 2" RCA 4902 phototubes are glued to the end of the waveshifter bars of the single width counters (while 3" RCA 4900 phototubes are used for the double width channels).

The SLIC is readout by LRS 2280 ADCs which provide automatic pedestal subtraction and 12 bit dynamic range. Calibration is performed



LEAD/LIQUID SCINTILLATOR SHOWER COUNTER (SLIC)
(SCHEMATIC)

Figure 3.9 The SLIC

Table 3.7 Detailed Properties of the SLIC

SLIC properties	distances in cm
Dimensions (y,z,x)	$243.84 \times 121.92 \times 487.68$
z position upstream	1839
z position downstream	1961
Number of Layers	60
Number of channels	334
Thickness of Pb layer	0.3175
Thickness of Al sandwich	0.01016
Thickness of scintillator layer	1.27
Single counter width	3.175
Radiation lengths	21.5
Interaction lengths*	2.1
Acceptance vertical	$\sim \pm 66$ mrad
Acceptance horizontal	$\sim \pm 133$ mrad

* This value is for nucleons.

during dedicated e^+e^- pair runs and using muons from the proton production target. Details of the procedure used can be found in [Ra87].

Typical electron showers deposit 60% of their energy in a single 1.25" counter width and are almost completely contained in 5 counter widths; hadron showers are roughly twice as wide. Electron showers deposit most of their energy in the 20 radiation lengths of the detector, whereas a significant fraction of the energy in a hadronic shower leaks out the back of the SLIC. Hadronic showers of a given energy produce sig-

nals which are about 0.71 times the size of signals produced by the same energy electromagnetic particles. Satellite showers produced by hadronic interactions often mimic low energy photons or neutrals and are a major source of background. Muons produce narrow ionization trails (they do not shower) and typically deposit only about 0.5 GeV, with a Landau tail.

The SLIC reconstruction begins by marking energy deposits which are due to charged tracks reconstructed in the drift chambers. Showers consistent with electrons and photons are distinguished from hadronic showers by using calculated E/p ratios and hadrometer pulse heights. A complex multiple regression fit to the observed shower energies is then performed to determine particle assignments and energies. The fitting procedure is discussed at length in [Su84].

After the first stage of SLIC analysis, the transverse SLIC pulse height distributions are compared with those expected from electromagnetic showers at the found energies and position. This is done by a set of subroutines which compare the observed showers to library showers generated by the EGS shower Monte Carlo. This technique helps to separate the noise from nearby hadronic showers and thus leads to improved energy resolution. The comparison with EGS showers is also used in the computation of the probability that the shower is of electromagnetic origin. The second stage of SLIC reconstruction is referred to as "The Afterburner".

The SLIC can resolve shower centroids to about 3 mm, and has a fractional energy resolution of about $21\%/\sqrt{E}$ (in GeV). Note that two photons from a 20 GeV π^0 decay will be separated by about 25 centimeters

at the front face of the SLIC.

In analyses of semileptonic charm decay modes, the SLIC is used for electron identification. An electron probability is determined using E/p ratios, shower widths, shower shapes, and by comparing energy depositions in the SLIC and hadrometer. By cutting on a electron probability variable (EMPROB2), it is then possible to obtain samples for which the electron identification efficiency (for electrons with $p > 12$ GeV) is 80% and the pion misidentification probability is 1%. Cleaner samples with an electron efficiency of 50% and a pion contamination of 0.2% can also be obtained with tighter cuts. Using this method to identify electrons, we are able to observe the exclusive charm decay modes $D^0 \rightarrow K^- e\nu$ and $D^+ \rightarrow K^- \pi^+ e^+ \nu$. By combining pairs of reconstructed photons, we are also able to observe clean $\pi^0 \rightarrow \gamma\gamma$, $\omega \rightarrow \pi^+ \pi^- \pi^0$, and $\eta \rightarrow \gamma\gamma$ signals. The typical reconstruction efficiency for a high energy π^0 in the charm decay mode $D^0 \rightarrow K^- \pi^+ \pi^0$ is about 15%.

An array of 19 shower counters, mounted on a shelf on the front face of the SLIC at a beam height, intercepts beam pairs and thus helps to reduce the confusion in the congested central region of the SLIC. The 9 central pairplane counters contained alternating layers of tungsten and lucite. The outer counters were somewhat wider and contained alternating layers of lead and lucite. Particles are detected by collecting the Cerenkov light emitted in the lucite by electrons that are produced by showers in the layers of lead (or tungsten). The shelf of counters presents 20 radiation lengths to incident particles. A wall of 10 radiation length lead bricks

behind the counters prevents any residual electromagnetic energy from leaking into the SLIC.

The counter pulse heights are digitized by 2249 ADCs. The pairplane is calibrated during dedicated e^+e^- runs, by comparing the drift chamber momenta to the counter pulse heights. Due to the congestion in this portion of the spectrometer, the information from the pairplane counters was not used in the calorimetric reconstruction. A summary of their characteristics is given in Table 3.8.

Table 3.8 Detailed Properties of Pairplane Counters

Pairplane properties	distances in cm
Dimensions (x,y)	174 × 12.5
Number of channels	19
Tungsten-Lucite counters	C counter C _{east} , C _{west} XE1-XE3, XW1-XW3
Lead-Lucite counters	XE4-XE8, XW4-XW8
Thickness of tungsten layers	2.54
Thickness of lead layers	5.1
Thickness of lead bricks	0.95
Single counter widths	6.35,12.7
Radiation lengths	30
Interaction lengths	1.1
z position upstream (cm)	1829
z position downstream (cm)	1839

3.7 The Hadrometer

A large area steel scintillator calorimeter located behind the SLIC is used to detect energy from hadronic showers initiated in the SLIC as well as energy deposited by muons. This counter is divided into an upstream and downstream module separated by a small gap. Each module contains 18 layers of 1" thick steel and 3/8" scintillator. The scintillator has two views X and Y. The views alternate in each layer. Each view is divided into 5.7" wide strips. The individual strips from 9 layers are integrated in the z direction and connected by a lucite light pipe to low cost 5" EMI 9791KB phototubes. The X strips are read out at the top of the counter, while the Y strips as in the SLIC are read out on the east and west sides of the counter. The hadrometer anode signals are digitized by LRS 2285 modules.

The most important role of the hadrometer is in the trigger. It is an essential component of two experimental triggers: the total hadronic cross section trigger (TAGH) and the transverse energy trigger (E_T). Both triggers will be described in more detail in section 3.11.

The fractional energy resolution of the hadrometer is about $75\% / \sqrt{E(\text{in GeV})}$, while the intrinsic position resolution is less than 2" [Ap86]. This position and energy resolution is not very useful because of the broad width and large fluctuations typical of hadronic showers. Although a K_L signal is present in the reconstructed data, due to its intrinsically poor energy resolution, the hadrometer's most important role in the reconstruction is not the identification of hadronic neutrals, but as a source of extra constraints

Table 3.9 Detailed Properties of the Hadrometer

Hadrometer properties	distances in cm
Dimensions (x,y)	270 × 490
Number of Layers	18
Number of channels	142
Thickness of steel layers	2.54
Thickness of scintillator layers	0.95
Thickness of steel (total)	91.4
Thickness of scintillator (total)	34.3
Single counter width	14.48
Radiation lengths	52.8
Interaction lengths	5.9
z position upstream (cm)	1962
z position downstream (cm)	2120

for the SLIC reconstruction. Since typically only a small fraction of the energy in an electromagnetic shower leaks out of the SLIC, large pulseheights in the hadrometer indicate the presence of a hadron. Similiarly narrow widths and small pulseheights in both modules of the hadrometer indicate the presence of a muon.

3.8 Muon Detection

A forty inch thick steel wall located behind the hadrometer ranges out most of the remaining hadrons as well as low energy muons. If a muon has a momentum above 5 GeV, it will generate a signal in a wall of large scintillation counters behind the steel. These counters are either 18" or 24"

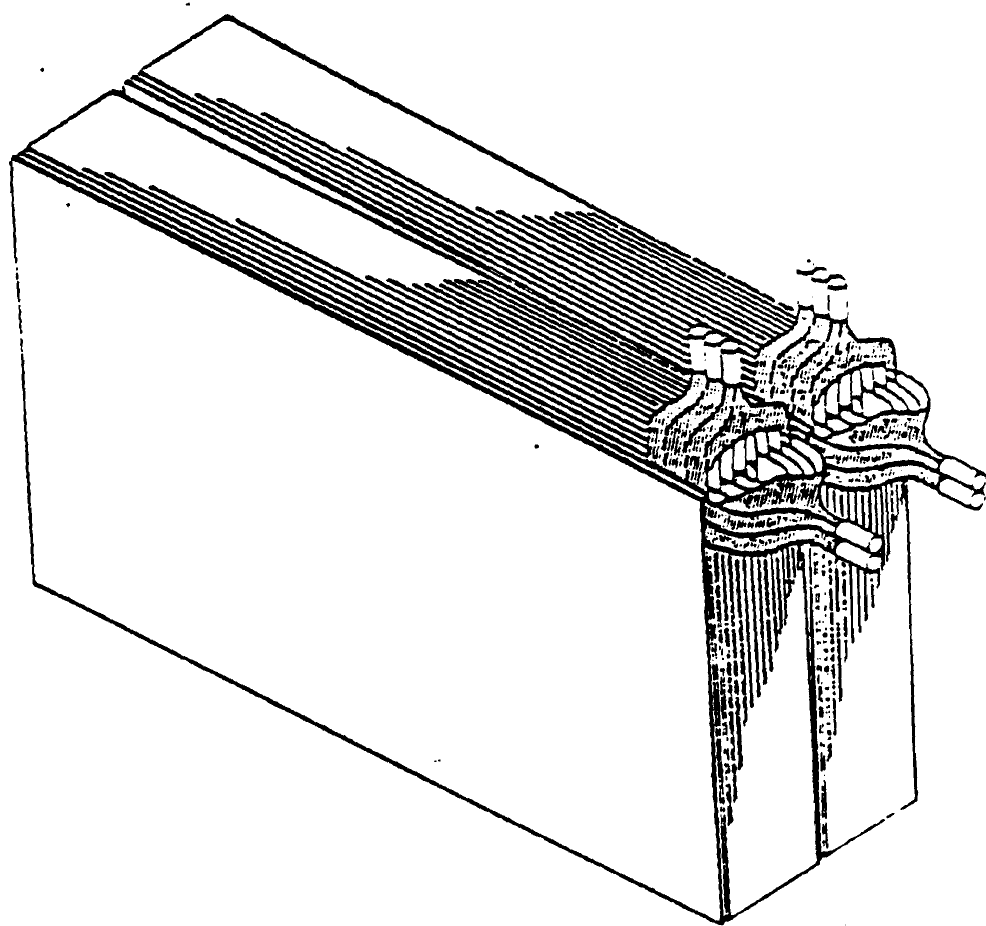


Figure 3.10 The Hadrometer

wide scintillator strips with an X measuring view only. The scintillators are connected by lucite light pipes to 5" EMI 9791KB phototubes. Each of the muon wall pulseheights is discriminated and then sets a latch. The arrival times of each of the discriminated pulses stops a TDC and are used offline to calculate the Y position of the muon. The muon wall is 94% efficient for high energy muons. Typical noise rates in the muon counters are around 1-2 MHz. The discriminated muon counter signals are also used in a dimuon trigger [Ra87].

Another set of large scintillation counters is located inside a concrete wall at the entrance to the spectrometer hall, about five meters upstream of the experimental Be target. These counters are used to veto muons which are produced at the upstream proton target.

3.9 The Trigger

In order to separate hadronic events from the low mass electromagnetic pair production events which are 1000 times more abundant, we must impose a fast hardware selection criteria or trigger. The two most important triggers in this experiment were the "TAGH" and E_T trigger. A dimuon trigger was used for studies of the decay mode $J/\psi \rightarrow \mu^+ \mu^-$ and is described in detail in [Me86]. Calibration triggers are described in [Ra87].

The TAGH trigger required that the total hadronic energy detected in the calorimeters H ($H \equiv$ hadrometer energy + slic energy weighted by 12dB) be above 40 GeV and the presence of a coincident signal above

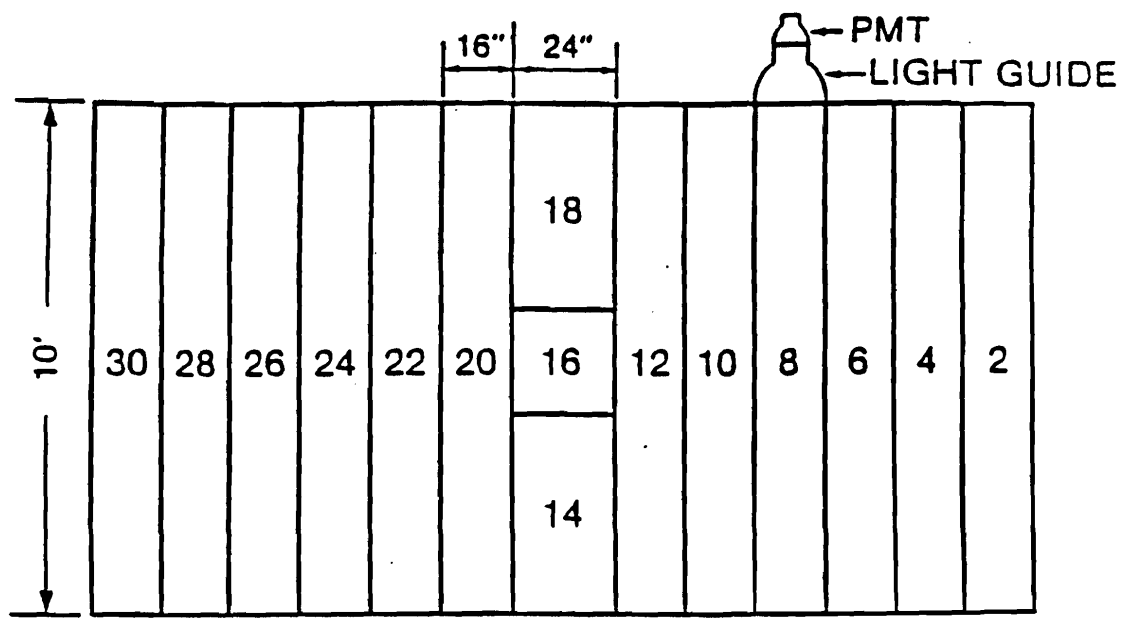


Figure 3.11 The Back Muon Wall

the level of a single minimum ionizing particle from the B counter (an interaction counter downstream of the target). We used this trigger to select an unbiased sample of hadronic interactions and to verify the proper functioning of the more complex E_T trigger. Roughly 10% of the data was recorded with the TAGH requirement.

Early Monte Carlo studies revealed that a trigger based on the total transverse energy observed in the calorimeters (E_T) could be used to separate charm events from other hadronic events which contain lighter quarks. For instance, the mean E_T of a sample of unbiased hadronic events is about 1.5 GeV compared to 4.5 GeV for charm events. The requirement $E_T > 2.2$ GeV actually used in E691 was found experimentally to reduce the hadronic background by a factor of three while retaining 80% of charm.

The E_T trigger was implemented using LRS 628 fan-in/fan-out modules. The dynodes of groups of eight adjacent phototubes were first summed and then weighted according to their perpendicular distance from the beam spot. The input weighting factor was chosen by soldering the appropriate resistor into an LRS module. We note that weighting factor was the same in the magnetic bend plane direction and in the direction perpendicular to that plane. The 500 MeV kick from the analysis magnets did not significantly degrade the effectiveness of this trigger.

Figure 3.12 shows a block diagram of the E_T trigger. At level 1, groups of eight channels were summed. At level 2, the outputs of the Level 1 modules were weighted. At level 4, the transverse energy signals from the SLIC and Hadrometer were combined. Once again, the SLIC signals were

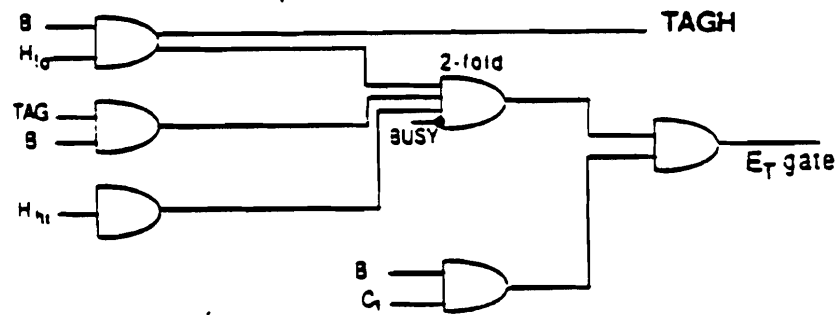
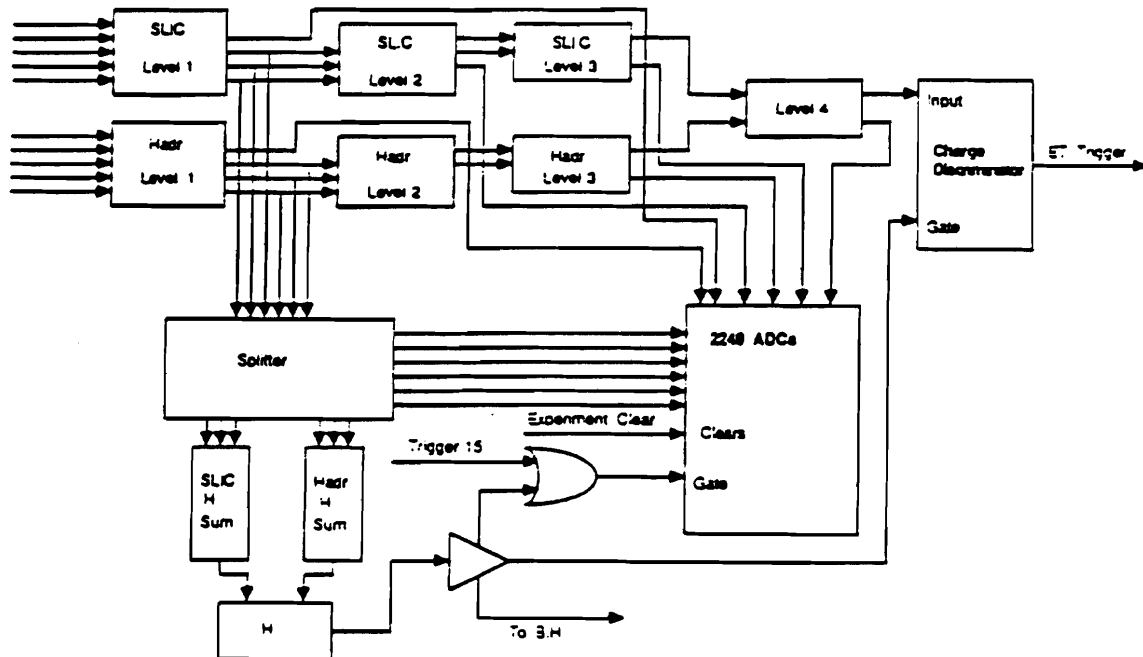


Figure 3.12 (a) A schematic of the E_T trigger (b) The gate for the E_T trigger

attenuated by 12dB; the value of the relative hadronic-electromagnetic calorimeter weighting factor was determined from runs with pion and electron beams [Pu85]. The small size of the input signal (2mV over a 0.5mV noise background), the very different temporal widths and large temporal spread of the inputs from the SLIC and from the hadrometer prohibited the use of a simple discriminator in the E_T trigger. Instead, we used a charge integrator module designed by C. Kerns which integrated the input signal during a 100 nsec gate and then discriminated the signal. In such a module, the noise will be time integrated to zero.

The gate to the E_T trigger is shown in Figure 3.12. It required a two fold coincidence of B and C_1 (denoted $B \bullet C_1$)* and one of the following: either TAGH or $TAG \bullet B$ or a hadronic energy deposit greater than 70 GeV (H_{hi}). The $B \bullet C_1$ requirement was designed to eliminate random triggers due to a high energy muon from a neighbouring beamline overlayed on a low energy interaction in the B counter. The H_{hi} requirement was imposed to allow the trigger to bypass the high energy cutoff (~ 220 GeV) of the tagging system acceptance.

The E_T trigger allowed us to enrich the charm content of the events recorded on tape by roughly a factor of three and reduced the contamination of electromagnetic events to a negligible level. Running with this trigger, we recorded 100 events/per sec on magnetic tape and operated with about 30% deadtime. The ultimate limit on the event rate was however imposed by our data acquisition system and the luminosity of the

* C_1 means that the pulseheight from the first Cerenkov counter was above threshold.

photon beam.

3.10 Properties of typical events

A typical online event display is shown in Figure 3.13 below. These displays were useful for quickly discovering problems in the trigger while taking data. Among the features worth remarking in this particular display are the high hit density upstream of the first bend magnet, and the decreasing hit densities in the second and third drift chamber stations (D2 and D3). We note that the average track multiplicity in this experiment is about 10. The two clusters with large pulse heights in the hadrometer but no signals in the SLIC are probably associated with charged hadrons. The cluster in the lower portion of the display which appears only in the SLIC may be due to an electron. Detailed displays of the vertex detector and other detectors were also available.

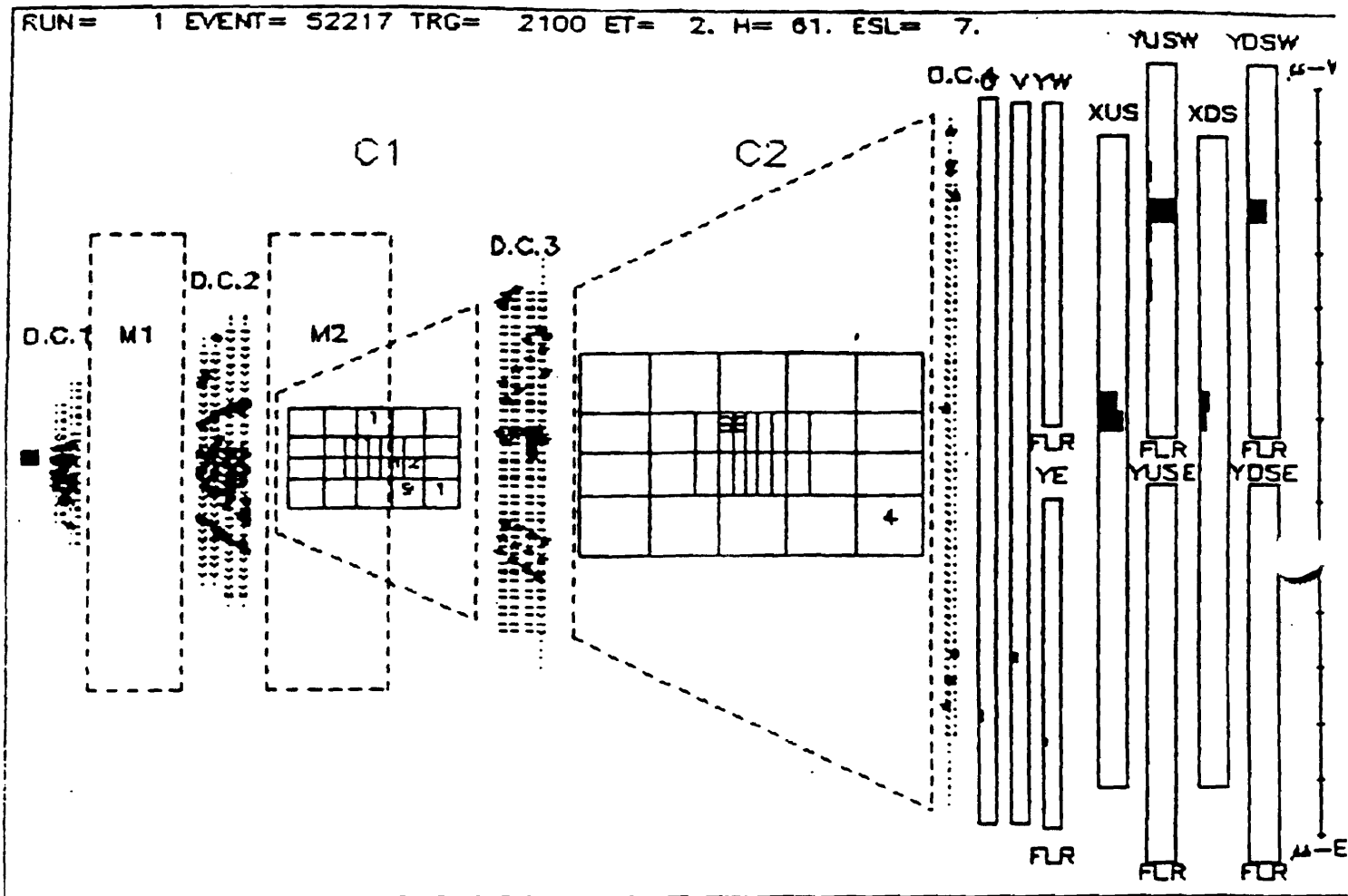


Figure 3.13 A typical online event display. Numbers in the Cerenkov counter cells indicate light levels. The rectangles labeled U, V, YW, and YE represent the U, V, west Y, and east Y views of the SLIC. The rectangles labeled XUS, YUSW, YUSE are the upstream X, west Y, and east Y views in the hadrometer. The heights of the darkened rectangles are the sizes of the signals.

4

The Data Reconstruction

4.1 Overview of the Reconstruction

To extract physics results from data, the raw digital information from the spectrometer must be converted into energy momentum four vectors of physical particles. This conversion is called the data reconstruction. The E691 reconstruction tasks were divided into two programs: PASS1 and PASS2. This partition was dictated by the memory space constraints of the CYBER 175 mainframe computer. The PASS1 program calculated the properties of charged particle trajectories. It produced as its output a list of momenta and intercepts for each charged particle trajectory in the three sections of the spectrometer. In units of CYBER 175 CPU time, PASS1 required about 670 msec per event. The PASS2 program performed calorimetry reconstruction, particle identification, and vertex reconstruction tasks. A typical reconstruction time for PASS2 is less than half the time required for PASS1 or about 300 msec per event. In the early period following the end of the experimental run we reconstructed about 15% of our data on the CYBER mainframes in order to verify the presence of charm signals. The limited computing power of the CYBER

mainframes, however, was not sufficient to reconstruct the full data sample in a timely manner and a more imaginative solution was required.

4.2 The Reconstruction Problem

The fractional charm content of photoproduced hadronic events is on the order of 1% and a typical reconstruction efficiency for a two body mode in which all the decay products are charged particles is about 10%. In an experiment with an open trigger, in order to study exclusive charm decays in detail, one must therefore accumulate large quantities of data. In E691, we collected 10^8 events which filled roughly 2000 6250bpi magnetic tapes. The fully optimized track and calorimetry reconstruction programs (PASS1 and PASS2) required roughly 1 sec of CPU time on a dedicated CYBER 175 mainframe or 7 sec on a VAX 11-780. To process the full data sample on a dedicated VAX would then require 35 years, or using a large fraction of the available mainframe computing power at FERMILAB, this time could at best be reduced to 3 years. Table I from a recent survey of computing in high energy physics[Gai87], shows that the computing requirements for E691 are larger than those of past experiments and are comparable to the requirements of several large colliding beam experiments planned for the near future.

4.3 Solutions

A simple solution to this computing problem is to devise some type of partial reconstruction algorithm which quickly selects charm events

Table 1. Computing Intensive Experiments

Experiment	Location	Events	VAX-sec/Event	VAX-yrs/CYr ^a
E691	Fermilab	10^8	7	35
UA1	CERN $p\bar{p}$	5×10^6	60	20
CDF	Fermilab $p\bar{p}$	10^7	200	50-100
L3	CERN LEP	4×10^6	120	48-60
SSC	?	10^7	1000	1220

a). This is the number of VAX CPU years per calendar year or per run.

and allows one to immediately discard the other hadronic events. Several attempts were made to devise such schemes - these approaches were ultimately rejected as it became apparent that a full track and vertex reconstruction is necessary before one can create a selection criteria with a reasonably high efficiency for charm.

As a stopgap measure we attempted to bring up a system of IBM 168 emulators based on a design by Kunz et al.[Ku76]. A 10 emulator system with a PDP host computer and associated peripherals, available to our collaborators at the University of Toronto, had the potential computing power of 10-15 VAX 11-780s. This system was sucessfully used for track reconstruction in E516, the preceding experiment. In E691, code is prepared for the emulators on the FERMILAB administrative IBM 4341 mainframe . A translator linker program converts the object code produced by the standard IBM fortran compiler into microcode suitable for the bit slice LSI processors of the 168Es. Unfortunately, this last re-

quirement means that the translator-linker program must be constantly updated to remain consistent with changes to the IBM Fortran compiler. Several instructions related to Fortran subroutine calls are not accepted by the current version of the translator linker. In addition, the 168E has only 192kbytes of memory space. To sucessfully fit the common blocks required for arrays and the program code into an emulator, both code and common blocks must be overlayed into five or six pieces. This means that immediately after any common block is no longer needed, it must be overwritten by another common block. The details of the overlays must be specified by the user. In addition, the 168E system was designed as a one of a kind installation at the LASS experiment and provides no facilities for debugging. For these and several other logistical reasons, as well as the availability of an alternative solution, we abandoned the 168Es.

The Advanced Computer Program (ACP)[Gai87], a parallel computing machine designed by a group at FERMILAB, was being tested at roughly the same time that we were making our last efforts on the emulators. The ACP consists of a set of single board computers based on 32 bit commercial VLSI processors such as the Motorola 68020 and the ATT32100 that can be programmed in ANSI standard FORTRAN-77. Each node consists of a module which contains a single processor, a floating point coprocessor for operations with real numbers, and 2 megabytes of RAM memory chips. The modules are designed to fit into a double width slot of a standard VME crate. Each VME crate of modules forms a branch. Branches are linked together by a high speed interface called

the branch bus connector (BBC). A DEC microvax controls the flow of physics events and code on the BBC through a Q bus interface.

The ACP system constructed at the FERMILAB computer center consists of a microvax, 1 input tapedrive, 2 output tapedrives, 120 nodes, and the necessary interface modules. The microvax controls the flow of events into and out of the nodes, stores calibration files, and processes dayfiles for production jobs.

Unlike the ACP, currently available supercomputers such as the CRAY and the CDC205, achieve their high speeds by taking advantage of the vectorial character of many computing problems. A trivial but illuminating example is the addition of two vectors. In this case, each component of the final result can be computed independently. Less trivial examples of problems that are optimized for such commercial supercomputers occur in aerodynamics and fluid mechanics. The code for reconstructing energy momentum 4-vectors in experimental high energy physics has been run on such supercomputers, with disappointing results in the majority of cases. In general, high energy physics code cannot be vectorized. By contrast, the ACP and other computing farms exploit the "trivial" and natural parallelism of the experimental high energy physics reconstruction problem to achieve performance comparable to a supercomputer; each event is produced by an independent interaction and therefore can be reconstructed independently and in parallel. Unlike other parallel computing farms that have been built in the past**, the ACP relies

** See [Gai87] for a detailed review of early efforts

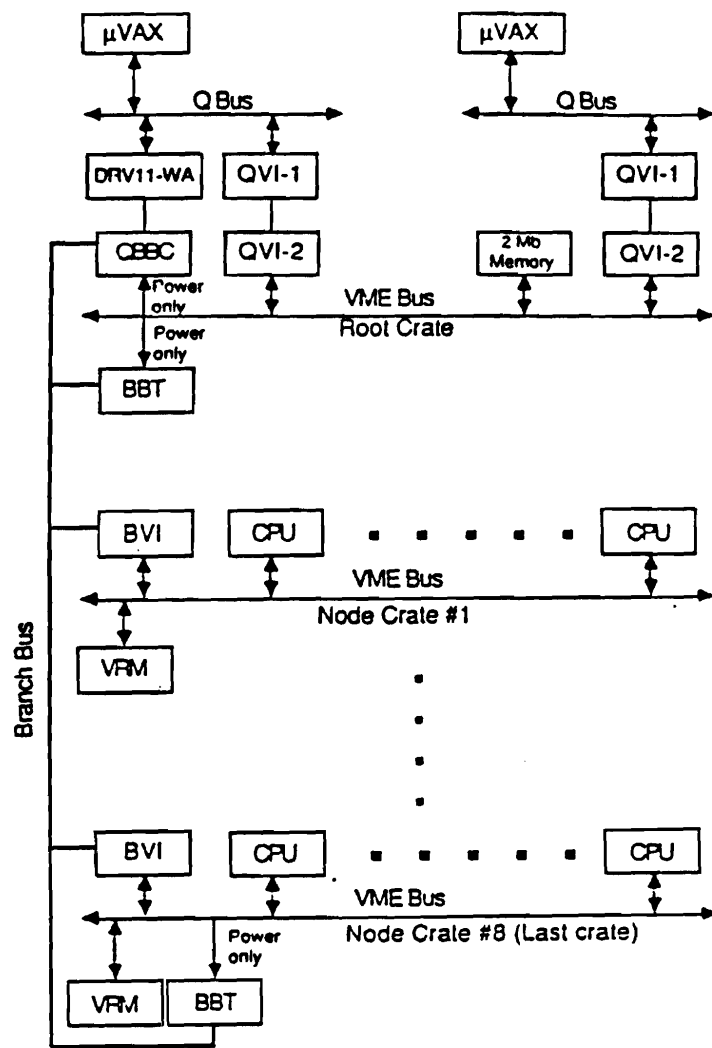


Figure 4.1 Block diagram of ACP processor hardware

on commercially available 32 bit single board computers, which can be programmed in FORTRAN-77. In contrast to the 168E and 3081E based computing farms, it is not wedded to a particular brand of chip and compiler or to a particular architecture [Gai87].

4.4 Code preparation

The first step in the preparation of track reconstruction code to run on the ACP is the conversion of code originally designed for the 60 bit word length of the CYBER 175 mainframe to the 32 bit word length characteristic of the VAX 11-780 and the ACP microprocessors. As a preliminary test at each stage of the conversion, we verify that our modified program can run and reproduce the same results on a VAX. One difficult aspect of the difference in the internal word length between machines is the conversion of data packing and unpacking subroutines which make explicit use of the word structure of the CYBER, VAX, or ACP. In addition, many common blocks in the original reconstruction program are forced by equivalence statements to share the same region of memory in order to fit into the limited memory space of the CYBER 175 (300000 octal words) and some subroutines which involve matrix inversions or other numerical computations can be sensitive to round off error. An additional complication was introduced by our earlier attempt to prepare the code for emulators. To conserve space, all the original integer arrays of PASS1 were converted to INTEGER*2 arrays. This conversion introduced several subtle errors in the alignment of common blocks and the addressing of sub-

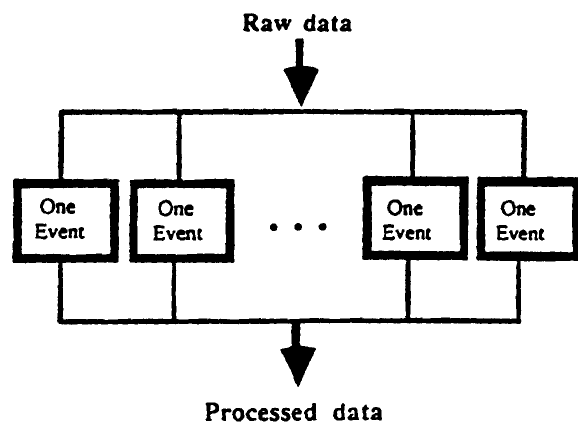


Figure 4.2 The trivial parallelism of the high energy physics reconstruction problem

routine calls. Other difficulties we encountered were due to uninitialized variables. On a CYBER, such variables are preset to easily recognizable forbidden values (using certain reserved bits of the 60 bit word), while on a VAX they are always set to zero. To make matters worse, such variables are not set to zero on the MC68020. After resolving all of the above problems, we retained all the final changes to the source code necessary for the conversion, on the CYBER, using the PATCHY source code maintenance facility. By setting a flag in a PATCHY procedure, we were then able to automatically produce a version of the code that was suitable for either a CYBER, VAX, MC68020 or ATT computer.

To run on the ACP, the user decomposes the reconstruction program into a host and node part; the host portion consists of initializations and input/output functions while the node portion contains the computation intensive kernel of the program. The host portion must be modified and integrated with the ACP system subroutines which provide relatively transparent utilities for broadcasting events to nodes and extracting events from nodes, as well as tape reading and writing.

An outline of our host program is described below. An ACP initialization subroutine is called to setup various conventions relevant to the system software and download the executable image of the node program. A system utility is called to open and mount tapes. The run number of the tape is determined and the appropriate calibration files are then read in from disk files on the microvax and broadcast to each of the nodes. Within the main event loop, buffers are read from tape. Events are ex-

tracted and transferred from the input buffer into an event array. The integrity of the event data structure is checked (i.e. presence and lengths of appropriate data types are verified by modified versions of subroutines from the CYBER monitor package) and the event is transferred directly to the output tape buffer if the event structure is defective or if it is a calibration event which requires no further processing. After the event reading is complete, the event is sent to an available node. The nodes are polled and if any node has completed processing of an event, an ACP utility is used to extract the event. The event is placed into an output tape buffer which will be written to an output tape when it is full. In E691 each input tape segment produces two tape segments of reconstructed data. After processing the first 25000 events of the first segment, the program waits until all the events on the last spill of this segment has been processed and then closes this tape segment and opens the second segment. (N.B. The reconstructed events are not in the same order as the events on the original data tapes, and the ordering of events within a spill, for instance, is not preserved. For some applications, the events must be sorted and reordered; this would introduce large overheads if carried out on the ACP. Instead, where correct event ordering is required, the sorting of events is carried out on in a separate pass on the CYBER.) After all processing has been completed, ACP SUMNODE is called to sum a histogram which contains statistics collected from all the nodes (i.e. number of tracks per event = number of tracks per event from node1 + number of tracks per event from node2...).

As an aide to this conversion process, a simulator was designed for the VAX 11-780. To run a program on the ACP simulator, the user selects a set of options in a user parameter file (UPF) file. An ACP utility (MULTICOMP) compiles the host and node programs and then splits them into a pair of communicating tasks within the VAX. Debugging a program on the simulator is sometimes helpful for programs in which the host node decomposition is subtle; in our case after running PASS1 as a standalone Fortran program on the VAX, the conversion to run on the simulator was trivial, requiring at most a few days of work.

It is important to remember that parallel computer farms such as the ACP require two executable images; one that is appropriate for the host computer and the other for the node computer. Otherwise, compilation and linking on real 68020 nodes is similiar to preparation for the simulator. The user invokes the MULTICOMP utility which recompiles or relinks only those parts of the program which have changed from previous compiling and linking passes. MULTICOMP copies the host and node program to a development microvax, compiles the host program using the VMS fortran compiler and then copies the node code to a dedicated compiler-linker Motorola node. The appropriate libraries are linked to the user object file by commands in LUNI, a UNIX like operating system which resides on the node. All the details of these processes are now hidden from the user (one simply types "ACP\$ MU program name"), although in the first few months of use, each of these steps was performed by hand. The resulting executable image of the node code is shipped back

to the user's VAX.

The compiler used on the 68020 was developed by the ABSOFT corporation and was certified as correct by the Department of Defense compiler verification program. Unfortunately, as we found by testing our 10000 line track reconstruction program, this compiler contained some serious bugs. In order to find the precise points in the code at which compiler bugs were located, we inserted printouts in the VAX and 68020 versions of the code - the 68020 allows for limited amounts of printout to disk files on the host microvax. After localizing the problem to a specific subroutine, we prepared two versions of the code, one to run on the versatile VAX debugger and one for the slow and limited ABSOFT debugger. We then laboriously single stepped through the code simultaneously on both machines - carefully comparing the values of all variables that were not stored in registers * until we found the compiler bugs. A typical example of a compiler bug is illustrative: If a type declaration of a variable is placed before an equivalence statement of that variable, very infrequently (i.e. every 1000 iterations) an incorrect instruction will be generated. Such a subtle compiler error is difficult to detect, since the majority of final results are correct and some small differences due to round-off error and different algorithms for operations with real numbers are expected. Several months of intensive work were required to find all the compiler bugs.

PASS1 was also brought up on ATT nodes. For these nodes, the

* The Abssoft debugger only allows the user to examine variables which are not stored in registers

Code Preparation

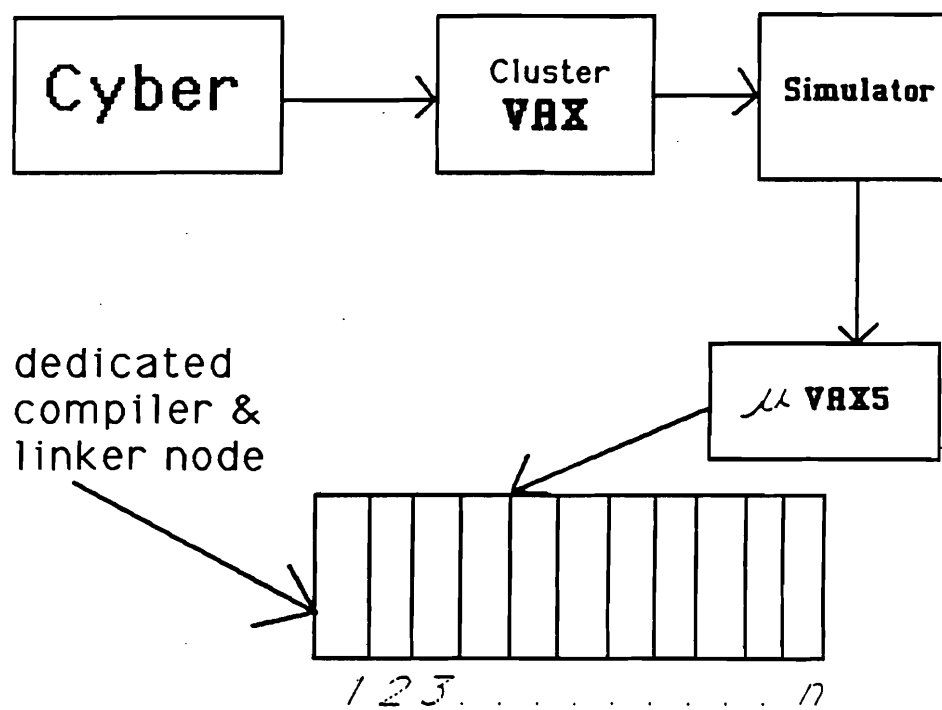


Figure 4.3 Block diagram of code preparation procedure

executable image was produced on a 3B2 ATT personal computer, using an ATT fortran compiler-linker, and shipped to the development microvax via a serial link. ATT does not furnish a debugger with their compiler. Fortunately, there were no significant bugs in this compiler. Some small modifications to the program were required in order to obey an ATT convention which forces equivalenced common variables to end on 4 byte word boundaries. The measured performance of ATT nodes was roughly comparable to the MC68020.

The conversion of PASS2- which contained the calorimetry, Cerenkov, and vertex reconstruction involved analogous problems. Small differences in the results for the SLIC reconstruction were traced, after much effort, to roundoff errors when converting from 60 bit to 32 bit precision in a power series expansion of an exponential attenuation function. Several new errors in the ABSOFT compiler were also detected.

Since the PASS2 reconstruction is at least twice as fast as PASS1, with a large 70 node system, we found that nodes often finished processing events before the microvax could deliver new events. To overcome this problem, we converted our host program to use the more complex LAYER2 system software subroutines, rather than the intuitively simpler LAYER1 routines. The former allow the user to directly manage the buffers which contain the events that go into and out of the nodes. The conversion to Layer 2 eliminated many of the overheads associated with copying physics events into the buffers of the system software and improved the system performance on PASS2 by nearly a factor of two. The

ultimate limit to ACP performance on very short programs is, however, determined by the I/O bandwidth of the Q bus interface between the microvax and the tape drive; this limit corresponds to about 0.5 Mbytes/sec (or about 25 events/sec for a single microvax system) [Na86].

After a working version of PASS1 was available, a batch job submission and production environment was set up in the FERMILAB computing center. Physicists on our experiment (every two weeks, a different member of the experiment held the position of "PRODUCTION CHIEF") submitted jobs via an interactive procedure on the "superhost" VAX 11-780. The tape mount requests were transmitted to an operator terminal and the executable images were copied to the host microvax while an operator mounted the necessary tapes. After the job finished processing events, the tapes were automatically dismounted, the dayfiles were converted to a compressed format ("VMS SAVE SETS"), sent to the superhost, and the next job request was relayed to the operators.

The quality of the reconstruction was monitored by the production chiefs who ran a procedure to extract the dayfiles from the VMS save set and read through the dayfiles produced by each ACP job. A summary table at the end of the dayfile listed physics statistics (e.g. average number of SMD hits, average number of tracks, etc.). Anomalies in these statistics were quickly investigated by the production chiefs. Including all overheads, the system delivered 0.7 VAXes/per node within the production environment. This benchmark could vary by $\pm 15\%$ depending on the average multiplicity of the events on the input tape.

Production running

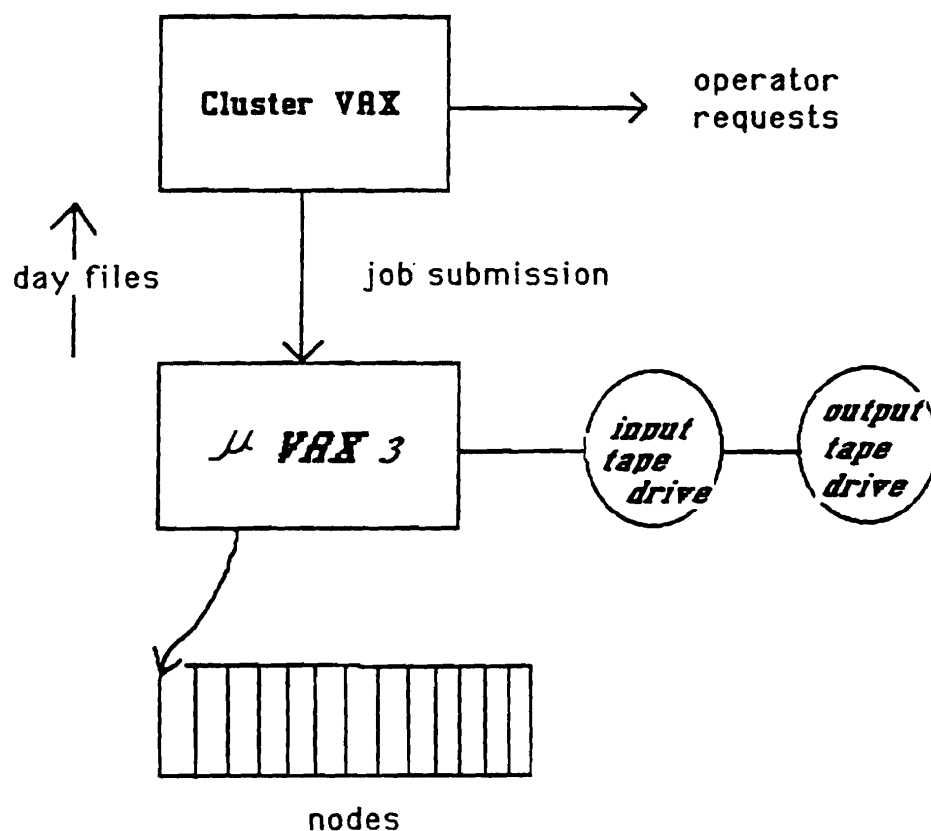


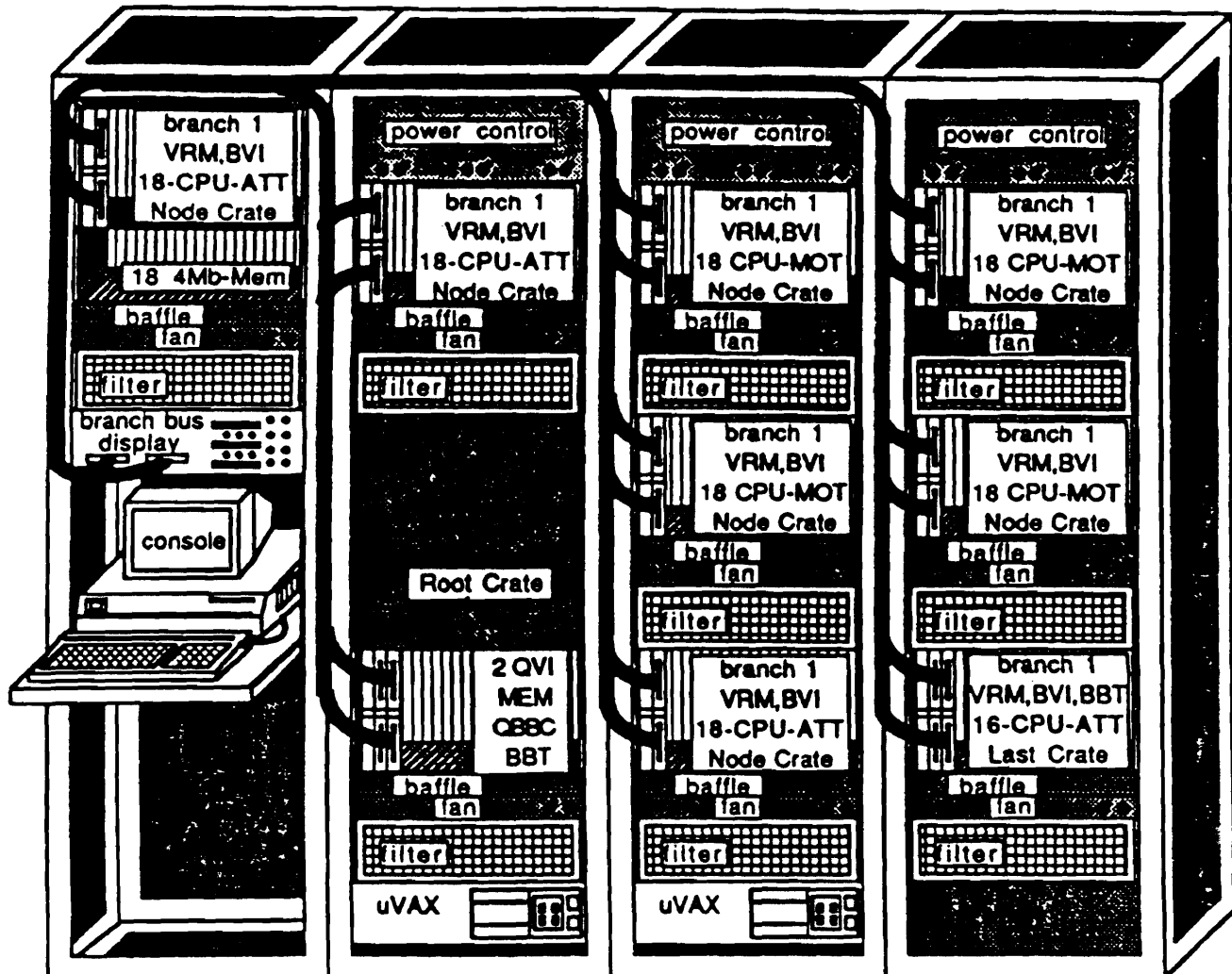
Figure 4.4 Block diagram of the production system

The primary sources of downtime in the production system were hardware problems with the conventional tapedrives, ACP developmental work, and poorly tested changes to the ACP system software. The ACP was used for all of the processing in the charged track reconstruction and for about 40% of the PASS2 reconstruction. If the full 120 node system had been available at the end of data taking for E691, the full reconstruction could have been completed in 3 months. In fact, due to the developmental difficulties associated with this new technology, the reconstruction took about a year.

4.5 Conclusion

The ACP is a cost effective solution to the large computing demands of experimental high energy physics. Future experiments can collect and then reconstruct the enormous amounts of data which are necessary to extend the search for very rare processes. Future versions of the ACP will use RISC* chips which possess the computing power of 5-10 VAXes and thus attain even higher speeds.

* The acronym stands for Reduced Instruction Set Computers



140 Node
Single Branch
2 uVAXs

Figure 4.5 Physical layout of the production system. During production running for E691, we employed a single branch, single MICROVAX version of the configuration shown above. The three tapedrives are not shown in this view.

5

Analysis

5.1 Introduction

In this chapter, we describe the selection criteria used to extract low background samples of events in two independent D^0 decay modes and the maximum likelihood fits used to measure the contributions from DCSD and mixing. We use the two decay chains $D^{*+} \rightarrow D^0\pi^+ \rightarrow [K^-\pi^+]\pi^+$ and $D^{*+} \rightarrow D^0\pi^+ \rightarrow [K^-\pi^+\pi^-\pi^+]\pi^+$ to evaluate the effectiveness of our selection criteria and to provide model independent normalizations for our measurements of mixing and DCSD. The charge of the slow pion is used to tag the charm quantum number of the D^0 meson at production. The analysis of mixing is complicated by the presence of DCSD decays which also give rise to wrong sign final states: $D^{*+} \rightarrow [D^0]\pi^- \rightarrow [K^-\pi^+]\pi^-$ is the signature for either mixing or DCSD. To separate these two physics processes, we use the decay time information from the silicon microstrip vertex detector.

5.2 Stripping and substripping

The first step in the analysis process is the reduction of 4000 recon-

structed data tapes to a handful of disk files which contain only pristine D^0 candidates. The original reconstructed data tapes which contain detailed information on the phototube pulse heights, widths of showers, wire numbers of hits on reconstructed tracks etc. were compressed into data summary tapes (DSTs) which retained only the most essential information from the reconstruction. The DST compression process reduced the number of the reconstructed data tapes by roughly a factor of ten.

After the DST compression, in order to facilitate a rapid selection of physics candidates, three additional programs were used to further reduce the volume of data and the number of candidates. The DST tapes were passed through a stripping program, a substripping program, and an analysis program. In each program, the selection criteria were made progressively more stringent. We will briefly discuss the stripping programs and substripping programs for the $K\pi$ mode and then the stripping programs and substripping programs for the $K\pi\pi\pi$ mode. The cuts that we used are given in tabular form in Appendix I.

A stripping program which selected $K\pi$ candidates began by requiring that the $K\pi$ invariant mass lie in the range [1.6-2.1] GeV/c^2 . In addition, the kaon-pion product probability as determined from the Cerenkov reconstruction had to be above the a priori level. Both the kaon and pion tracks had to be well constrained tracks that passed through the first magnet. Specifically, the number of degrees of freedom had to be greater than 11. In general, a track may have up to 39($= 44 - 5$) degrees of freedom, since there are 35 drift chamber planes, 9 SMD planes and 5

track parameters. No vertexing information was used at this stage.

The output tapes of the $K\pi$ stripping pass were then substripped to produce large disk files. The substripping program restricted the $K\pi$ mass to lie within a narrower range and then selected D^0 candidates using the reconstructed vertex information. We required that the kaon and pion tracks give an acceptable fit to a two track vertex and that there exist a primary vertex candidate with a good χ^2 per degree of freedom. The momentum vector of the D^0 candidate was computed and had to project back in the x-y plane to within $120\mu m$ of the primary vertex candidate (the transverse miss distance of the momentum vector is called DIP and thus this cut is called the DIP cut). We also calculated the longitudinal vertex separation Δz between the primary and secondary vertex and the error on this separation σ_z . Finally, we demanded that the ratio computed from these two quantities, $SDZ = \Delta z/\sigma_z$, be greater than 3. This SDZ cut is roughly equivalent to the requirement that the decay time be greater than 0.2 psec for fast D^0 s.

To select candidates for the $D^0 \rightarrow K\pi\pi\pi$ mode, a very general vertex strip developed by P. Karchin was used. This strip preferentially selected events with at least one two track vertex candidate in which both tracks passed through the two analysis magnets. It required SDZ , calculated with respect to the vertex which contains the most tracks, to be greater than 5. In addition, the reconstructed momentum vector of the tracks in this candidate secondary had to point back to within $200\mu m$ of the primary vertex. The vertex strip reduced the ~ 400 DST tapes

to a charm enriched sample of ~ 67 output tapes and thus significantly reduced the computing load of analysis programs on the CYBER. It also allowed substrips for multibody charm modes to be carried out easily.

The output tapes of the vertex strip were passed through a program which substrips for $D^0 \rightarrow K^-\pi^+\pi^+\pi^-$ candidates. This program searched for well constrained four track vertices in which each of the tracks had a momentum greater than 3 GeV and in which each track at least passed through the first magnet and D2. The four fold Cerenkov probability for the assignment $K\pi\pi\pi$ was required to be above the apriori peak. The line of the flight of the reconstructed D^0 momentum vector had to pass no more than $100\mu m$ from the primary vertex candidate. The event was rejected if SDZ, the significance of the separation of the primary and secondary vertex was less than 6. The event was also rejected if more than one extra track passed within $80\mu m$ of the secondary vertex. These cuts reduced the tapes of the vertex strip to eight large disk files.

5.3.1 Final Selection Criteria

To make the final event selection, the analysis program used the additional cuts described below, which were selected by maximizing the significance ($\sim S/\sqrt{B+S}$) of the right sign D^* signal.

In the $K\pi$ analysis job, both the kaon and pion tracks had to pass through the first magnet and D2. The pion track had to be inconsistent with an electron i.e. $\text{EMPROB2} < 90$. This cut was designed to eliminate backgrounds from the decay $D^0 \rightarrow K\epsilon\nu$ where the neutrino is soft. A

similar cut on muons was not used, because many pions give high muon probabilities. The D^0 momentum had to be in the range [35.,100.] GeV; this roughly matched the acceptance of the spectrometer although the lower cutoff did improve the significance of the signal.

The vertex cuts were further tightened. The D^0 momentum vector had to point back to within $80\mu m$ of the candidate primary vertex. To reduce backgrounds from D^0 's which combine with stray pions or other pions from the primary vertex, we required that either the slow pion be contained in the primary vertex or if it was not then the impact parameter of the slow pion with respect to the primary (RATPI) must be small. Another cut which reduced this source of background was the requirement that the distance of closest approach of the D^0 momentum vector and the extrapolated position of the slow pion track (DIP2) be less than $120\mu m$. The values for the last two cuts were determined by studying D^0 plus random pion events outside the D^* signal region on Monte Carlo $D^0 \rightarrow K^-\pi^+$ tapes.

To reduce the larger backgrounds from uncorrelated four body combinations and high multiplicity charm decays, the candidates for $D^0 \rightarrow K^-\pi^+\pi^-\pi^+$ decays were subjected to more stringent vertex cuts than the candidates in the $K\pi$ mode. For these candidates, the D^0 momentum vector had to point back to within $65\mu m$ of the primary vertex. The χ^2 per degree of freedom of the four prong secondary vertex had to be less than 3.5. We required the slow pion to pass through the primary vertex. The distance of closest approach of the D^0 momentum vector and the

slow pion had to be less than $150\mu m$. In addition, by imposing the requirement that no extra tracks pass within $80\mu m$ of the secondary vertex, we eliminated some contamination from higher multiplicity charm decays. We also included the less obvious requirement that the no track in the secondary vertex pass significantly closer to the primary vertex than to the secondary vertex. This cut eliminated events with ambiguous vertices. To implement this cut, we computed the maximum of the ratios of the transverse miss distance of each track in the secondary to the transverse miss distance of each track in the primary. More explicitly, we defined a variable $RATBIG = \max_{1 \leq i \leq 4} [DIP_i(\text{secondary})/DIP_i(\text{primary})]$ where the index i labels the tracks in the secondary vertex and then required that: $RATBIG < 1.5$. This "RAT cut" improved the significance of the signal, although it was biased against short lived events. It was also a powerful background reduction tool for analyses of other multibody charm decays such as $D_s^+ \rightarrow \pi^-\pi^+\pi^+$ or $D^+ \rightarrow K^-\pi^+\pi^+\pi^-\pi^+$ in which the signals cannot be clearly distinguished from the large backgrounds without this cut.

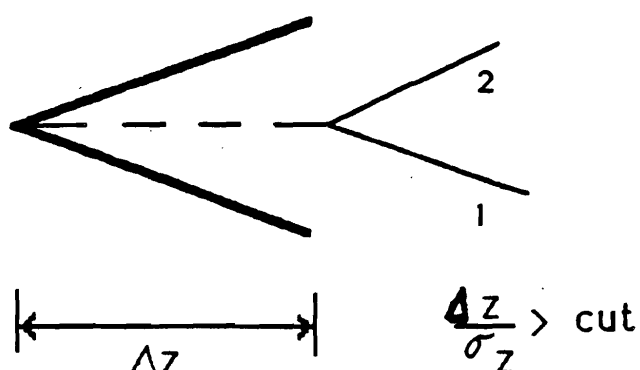
In the stripping, substripping, and analysis programs, some of the cuts such as the SDZ cut, the RAT cut, and the isolation cut, are time dependent and may have depleted the events at short times. To precisely determine how the time distributions of the signal were modified by these cuts and by effects due to the time dependent acceptance of the spectrometer, we fitted the time distributions of the right sign signals using the Monte Carlo. In all cases, our results were consistent with the

observed time dependence of the right sign signals. The maximum likelihood fit, which we used to extract the final result, took account of these modifications to the time distributions.

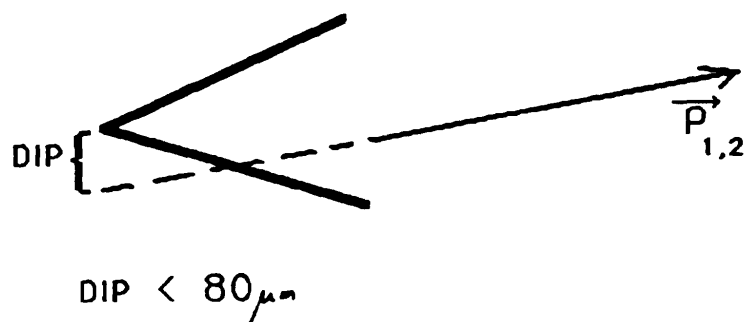
5.3.2 Backgrounds

For both of the modes in the mixing analysis, the dominant source of background contamination at long decay times is real D^0 s which combine with wrong sign pions in the event. In most cases, the wrong sign pion originates in the primary vertex. At shorter times, uncorrelated combinations of kaons and pions give backgrounds which are comparable to those produced by D^0 s which combine with random pions. Although the double misidentification probability is about 1%, right sign D^0 decays in which both a kaon and pion are misidentified (e.g. $D^0 \rightarrow K^-\pi^+$ misidentified as $D^0 \rightarrow K^+\pi^-$) yield a very small contribution to the background. In this experiment, the momenta of the decay products are relativistic; therefore when the particle identification assignments are inverted, the invariant mass will be shifted far outside the D^0 mass region unless the momenta of the pion and of the kaon are nearly equal [see figures 5.15 and 5.16 for an illustration of this effect]. Singly Cabibbo suppressed D^0 decays in which a single decay product is misidentified, for instance $D^0 \rightarrow K^-K^+$ with either the K^- or K^+ misidentified as a pion, do not contribute in the signal region. For such decays, the reflections are typically broad distributions which are well separated from the D^0 peak. For example, the upper edge of the reflection from misidentified $D^0 \rightarrow K^-K^+$

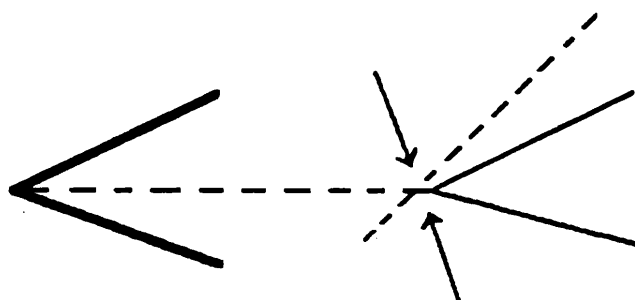
SDZ Cut



DIP Cut

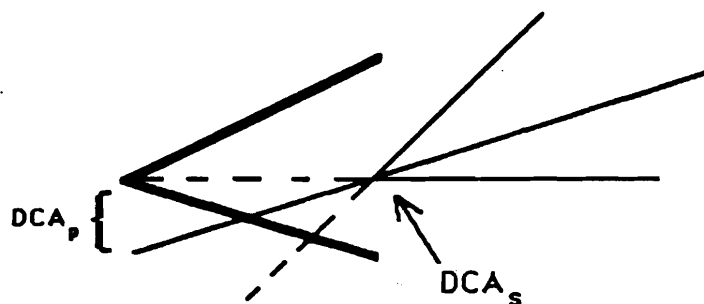
**Figure 5.1** The SDZ cut and DIP cut

Isolation Cut



DCA of extraneous tracks $> \sim 80$ microns

Rat Cut for multibody charm decay modes



$DCA_s < DCA_p$

for all tracks in the secondary vertex

Figure 5.2 The isolation cut and RAT cut

decays begins 60 MeV below the D^0 mass and extends down to low invariant masses. The invariant mass resolution at the D^0 mass is about 10 MeV, so for E691, in contrast to some e^+e^- experiments (especially those performed at the ψ'' where the D mesons are produced nearly at rest), this type of background is not a serious limitation.

There is an additional background due to real D^* decays in which one of the decay products is misidentified or not detected, which is only present in the right sign plots. This background appears in the Q value band of the D^* below the D mass, but does not contribute in the signal region. Estimates of possible contributions to this background are given in Table 5.1. We are able to roughly account for the magnitude of this background, as determined from the maximum likelihood fit. Decays with missing π^0 , for instance $D^0 \rightarrow K^-\pi^+\pi^0$ do not contribute to this background; these decays give reconstructed $K\pi$ masses which are shifted at least one π^0 mass below the D mass. Semileptonic decays may give a small contribution. Radiative D^0 decays such as $D^0 \rightarrow K^-\pi^+\gamma$ may also be present. We estimate the rate for such radiative D^0 decays, by extrapolating from the measured radiative $K^0 \rightarrow \pi^+\pi^-\gamma$ decay mode [Ta76]. The ratio of the rate for $D^0 \rightarrow K^-\pi^+\gamma$ to $D^0 \rightarrow K^-\pi^+$ can be calculated from first principles since it corresponds to the decay $D^0 \rightarrow K^-\pi^+$ followed by the bremsstrahlung production of a photon off either the pion or the kaon. For $K^0 \rightarrow \pi^+\pi^-\gamma$, one finds:

$$\frac{1}{\Gamma(K^0 \rightarrow \pi^+\pi^-)} \frac{d\Gamma(K^0 \rightarrow \pi^+\pi^-\gamma)}{dE_\gamma} \propto \frac{1+\beta^2}{\beta} \frac{\alpha}{E_\gamma} [\log(1+\beta)/\log(1-\beta)-1]$$

where $\beta = \sqrt{1 - (4m_\pi^2)/(m_K^2 - 2m_K E_\gamma)}$. The larger mass of the D meson implies that the branching ratio for $D^0 \rightarrow K^-\pi^+\gamma$ relative to $D^0 \rightarrow K^-\pi^+$ should be about 5.5 times larger than the corresponding ratio for the K_s . [The ratio is: $\frac{\Gamma(K_s \rightarrow \pi^+\pi^-\gamma)}{\Gamma(K_s \rightarrow \pi^+\pi^-)} \approx 2.7 \times 10^{-3}$ for $E_\gamma > 50$ MeV]. The events from these radiative decays should appear just below the D^0 mass and should exhibit a $1/E$ bremsstrahlung type spectrum in $K\pi$ mass. The possibility of $D^0 \rightarrow K^-\pi^+$ decays in which the pion generates a knock on electron and thus shifts the reconstructed invariant mass below the D^0 mass, is also estimated. This source of background is negligible.

Table 5.1 Possible contributions to the right sign D^* background for $K\pi$ mass in the band [1.75,1.84] GeV.

Mode	Branching ratio	Possible contamination
$D^0 \rightarrow K^-\mu^+\nu$	4%	~ 5
$D^0 \rightarrow K^-\epsilon^+\nu$	4%	~ 1.7
$D^0 \rightarrow K^-K^+$	0.6%	~ 15
$D^0 \rightarrow K^-\pi^+\gamma$	$\sim .07\%$	~ 10.5
$D^0 \rightarrow K^-\pi^+$ knock on		< 1

A scatter plot of $M(K\pi)$ versus Q value is shown in Figure 5.3(a),(b) for the final sample of right sign $K^-\pi^+\pi^+$ and wrong sign $K^-\pi^+\pi^-$ events with the selection $\tau > 0.22$ psec. The boxed signal region in the right sign scatter plot contains 611 events. In the vertical direction above the signal region, a band of events in which a D^0 has combined with a random pion is visible. This source of background, which does not peak in Q value,

contributes ~ 7 events at $t > 0.22$ psec. It becomes the largest source of background at long times. Events due to uncorrelated combinations of kaons and pions contribute ~ 5 events at $t > 0.22$ psec and are distributed over the entire plot. The events inside the boxed region of the wrong sign plot are consistent with background.

In the Q value band of the D^* below the D mass, there is an enhancement, which is present only in the right sign plot, due to real D^* events which do not decay to the $K\pi$ final state. The possible origin of this source of background was discussed at length in the previous section. We showed that we could roughly account for the magnitude of this background. It is worth remembering that this source of background does not contribute in the signal region.

As we discussed in the introduction, DCSD events have a time distribution $N_{\text{wrong}}(t) \propto \exp(-t/\tau_D)$, while decays from mixing follow a $t^2 \exp(-t/\tau_D)$ dependence which peaks at two D^0 lifetimes. Therefore, if we impose the additional selection $t > 0.88$ psec, we will retain roughly 68% of the mixing decays and only 14% of the DCSD decays. We will also reduce the combinatorial background to a negligible level. Figures 5.4(a),(b) show the corresponding scatter plots with the selection $t > 0.88$ psec or roughly two D^0 lifetimes. We expect 2.7 events with no mixing, of which 2.2 are due to D^0 's which combine with random pions and 0.5 due to uncorrelated combinatorial background. There is only one event in the signal box (and 3 events near the border of the box). If $r_M \sim 1\%$, there would be about 11 events at the D^* .

Figures 5.5(a),(b) show the analogous scatter plots for the $K\pi\pi\pi$ channel. A band of events in which D^0 's combine with random pions is again visible above the signal region. There is no significant enhancement to the left of the right sign signal box, in contrast to the $K\pi$ mode. There are 375 ± 18.5 events in the right sign signal box. The SDZ cut applied in the vertex strip and the RAT cut applied in the analysis job have depleted the events at short times. At long times i.e. $t > 0.88$ psec, when the cuts become fully efficient, and where we are most sensitive to mixing, the number of events in both modes are comparable. Thus, the $K\pi\pi\pi$ mode gives a measurement of mixing with the same sensitivity as the $K\pi$ mode. Figures 5.6(a),(b) show the same plots with the selection $t > 0.88$ psec. The two events in the signal box are again consistent with backgrounds. If $r_M \sim 1\%$, we would expect roughly 8.6 events at the D^* for $t > 0.88$ psec.

5.4.1 Maximum likelihood fits

Using all the available experimental information, we perform a maximum likelihood fit event by event as a function of three quantities: the invariant mass of the D^0 candidate, the Q value, and the decay time. We fit only events that lie in the range $1.75 \leq M(D^0) \leq 2.0$ GeV, $0.0 \leq Q \leq 30$ MeV, and $\tau > 0.22$ psec. We define the following quantities: $M(D^0) = M(K^-\pi^+)[M(K^-\pi^+\pi^-\pi^+)]$, $M(D^*) = M(K^-\pi^+\pi^+)[M(K^-\pi^+\pi^-\pi^+\pi^+)]$ and $Q = M(D^*) - M(D^0) - M(\pi)$. The proper time τ is the time measured from the production vertex to the

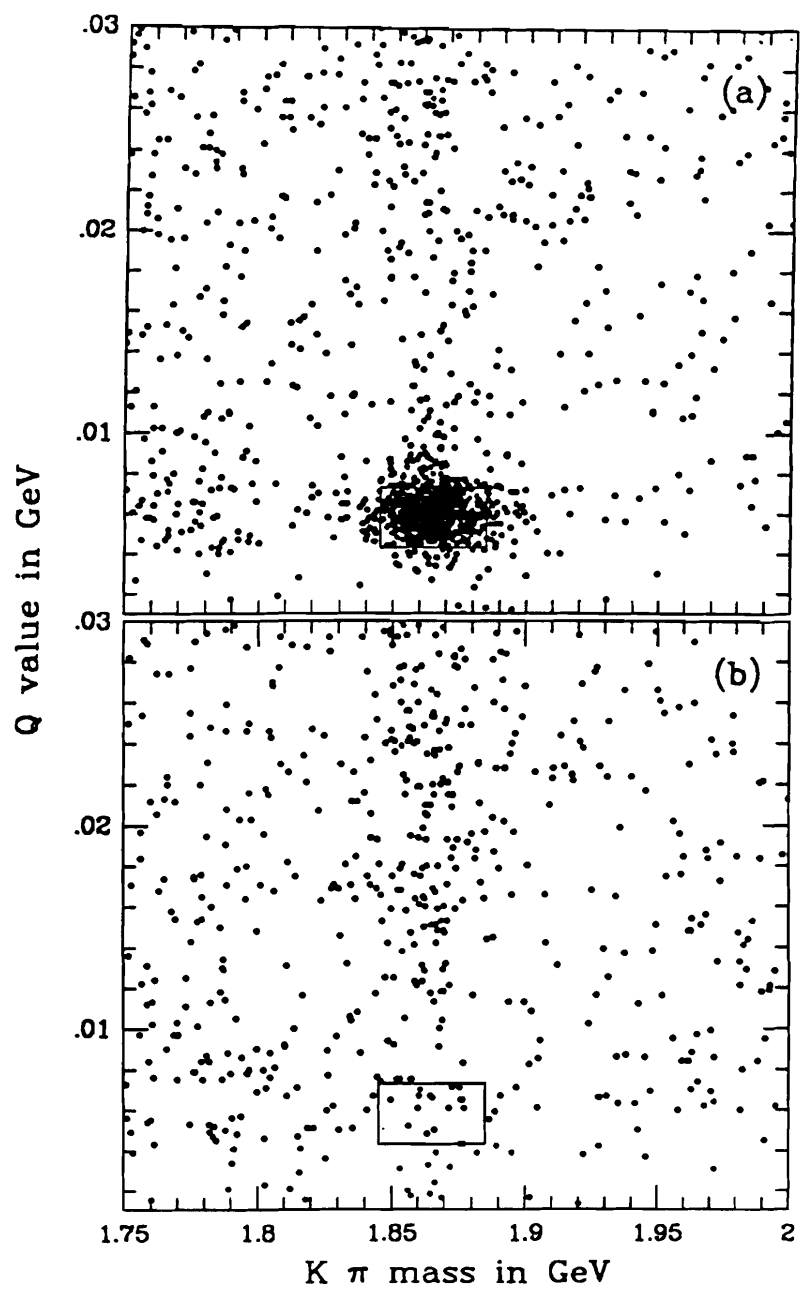


Figure 5.3 Scatter plot of $M(K\pi)$ versus Q value with the selection $t > 0.22$ psec for: (a) the right sign sample and (b) the wrong sign sample.

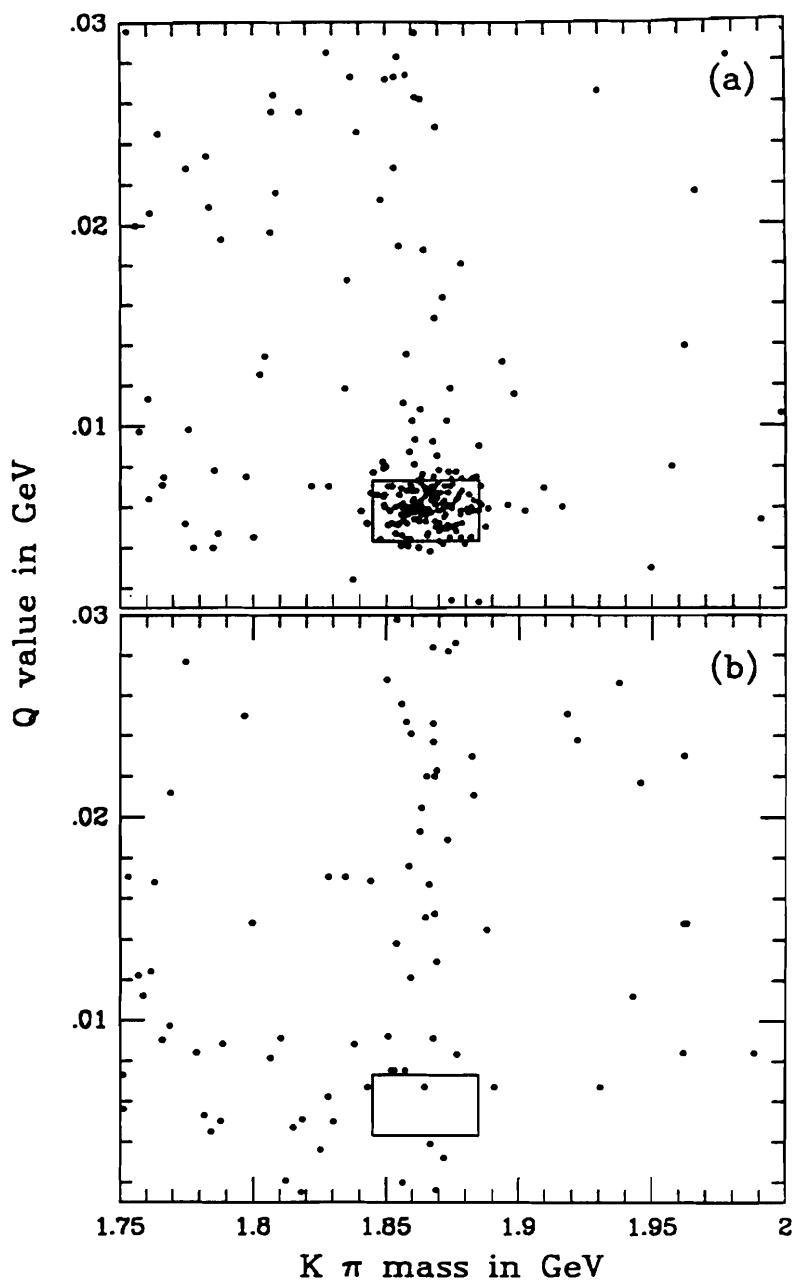


Figure 5.4 Scatter plots of $M(K\pi)$ versus Q value with the selection $t > 0.88$ psec for: (a) the right sign sample and (b) the wrong sign sample.

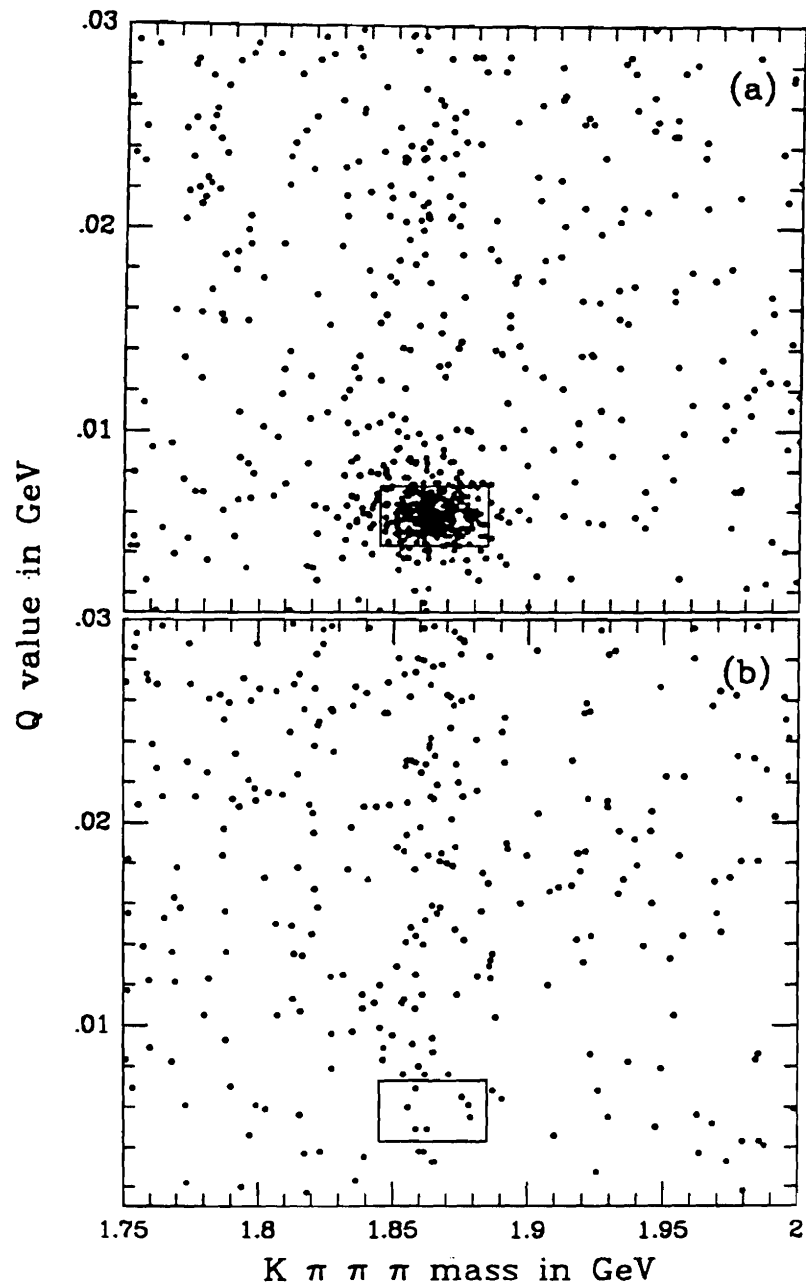


Figure 5.5 Scatter plots of $M(K\pi\pi\pi)$ versus Q value with the selection $t > 0.22$ psec for: (a) the right sign sample and (b) the wrong sign sample.

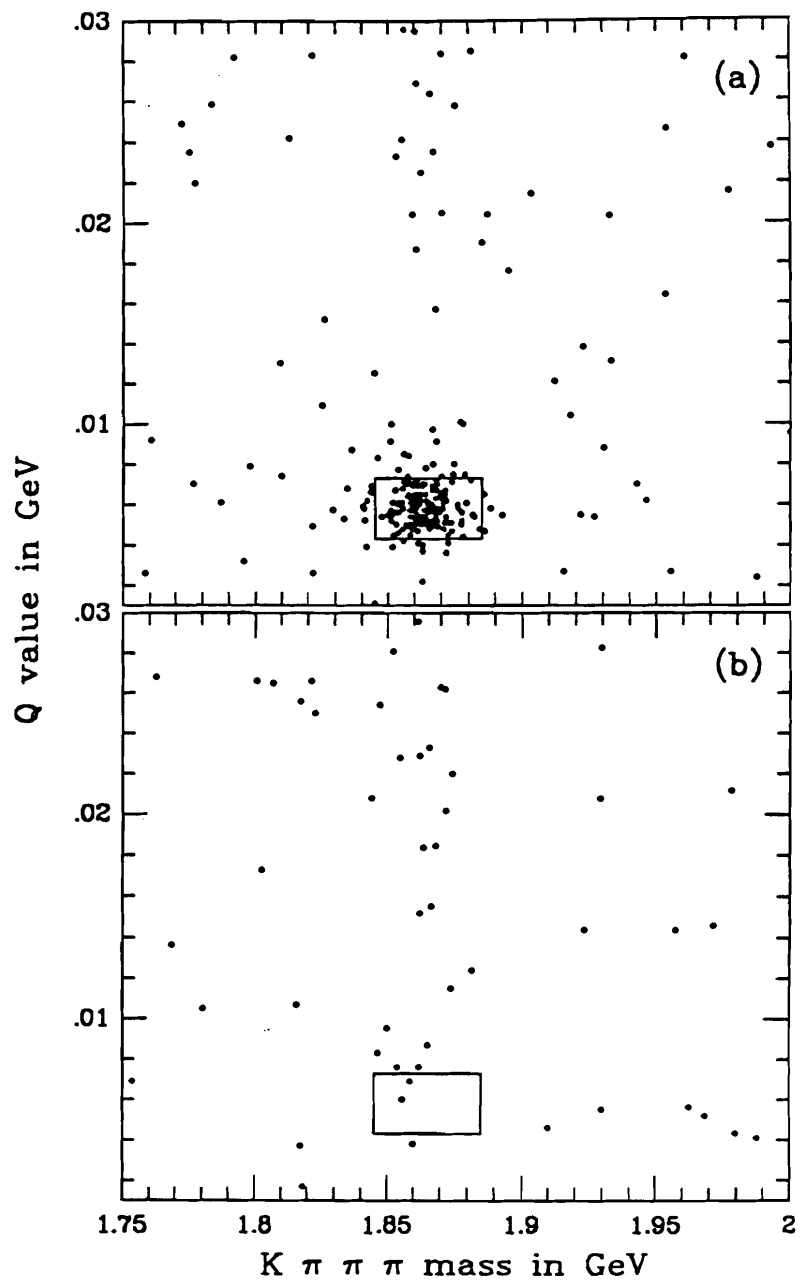


Figure 5.6 Scatter plots of $M(K\pi\pi\pi)$ versus Q value with the selection $t > 0.88$ psec for: (a) the right sign sample and (b) the wrong sign sample.

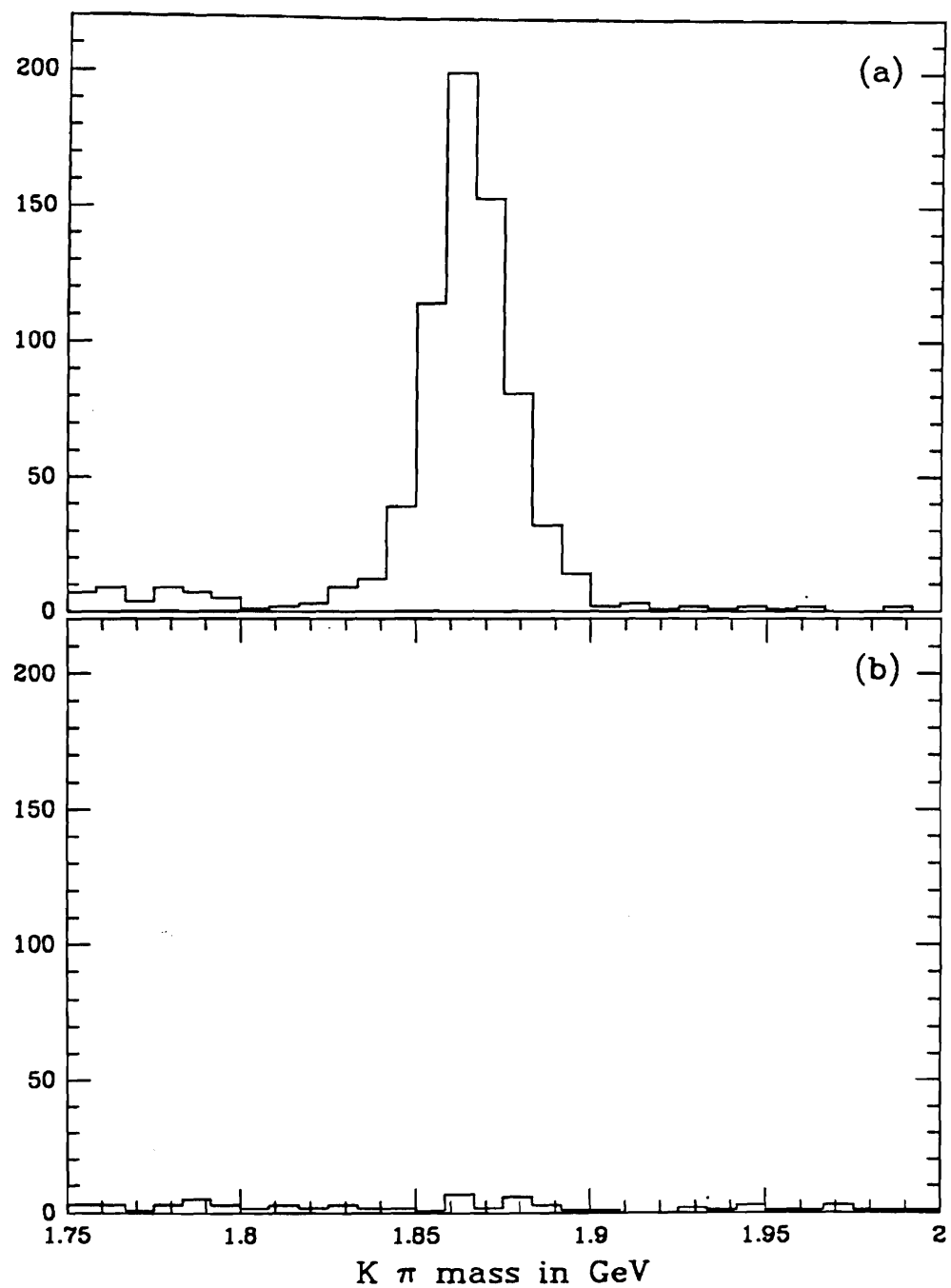


Figure 5.7 Projections of figures 5.3(a) and 5.3(b) onto $K\pi$ mass with the restriction $4.3 \leq Q \leq 7.3$ MeV

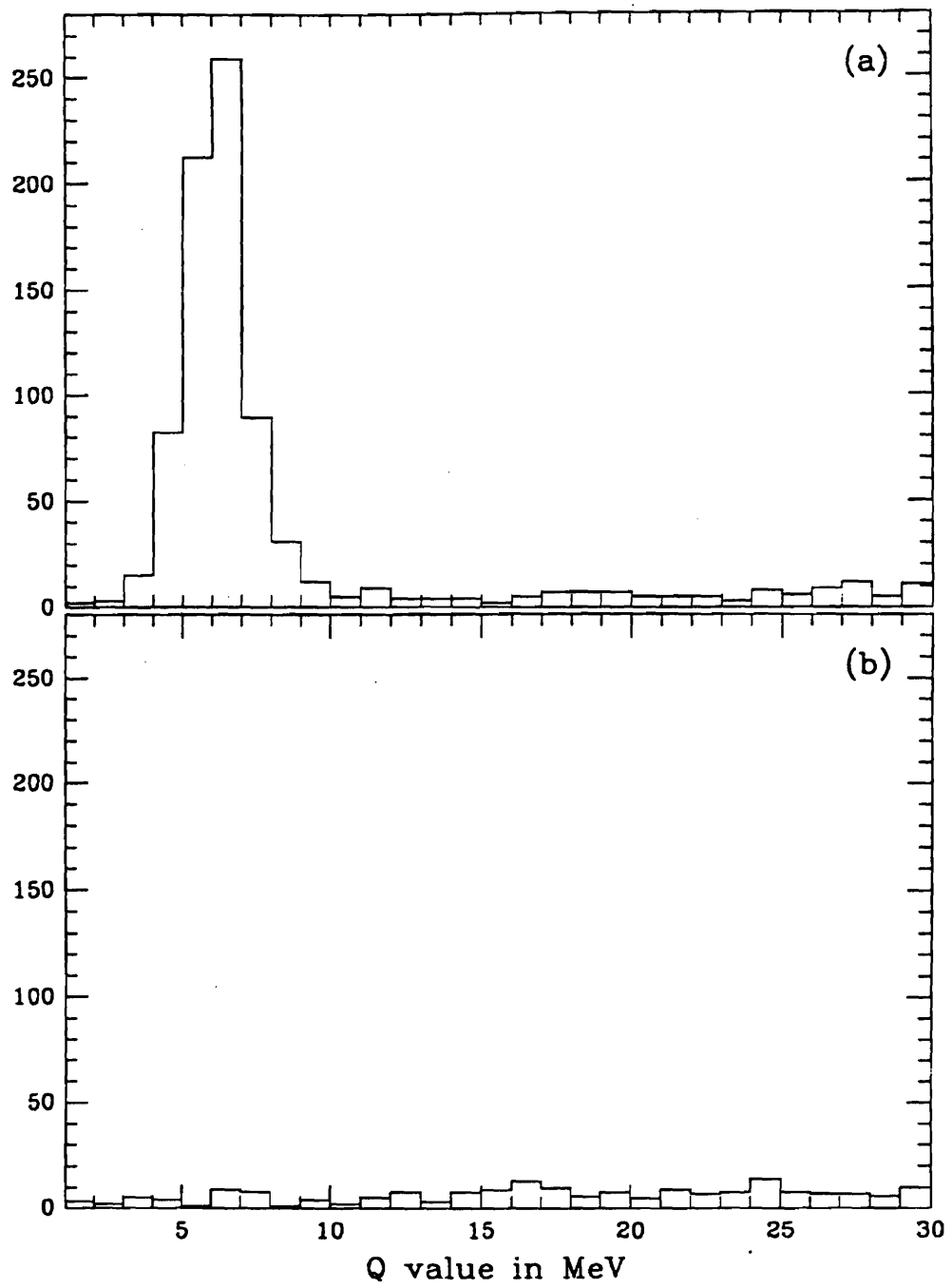


Figure 5.8 Projections of figures 5.3(a) and 5.3(b) onto Q value with the restriction $1.845 \leq M(K\pi) \leq 1.885$ GeV

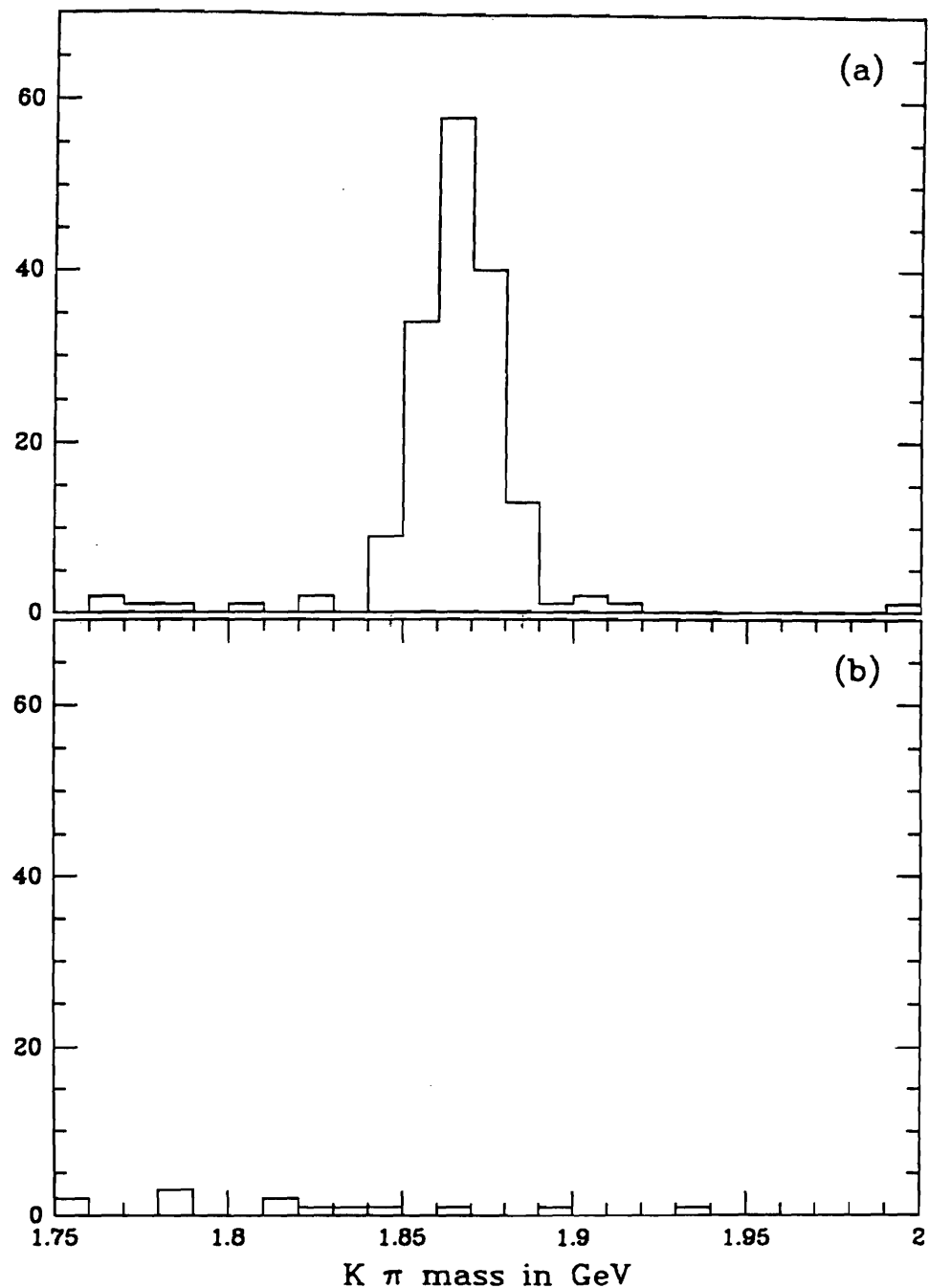


Figure 5.9 Projections of figures 5.4(a) and 5.4(b) onto $K\pi$ mass with the restriction $4.3 \leq Q \leq 7.3$ MeV

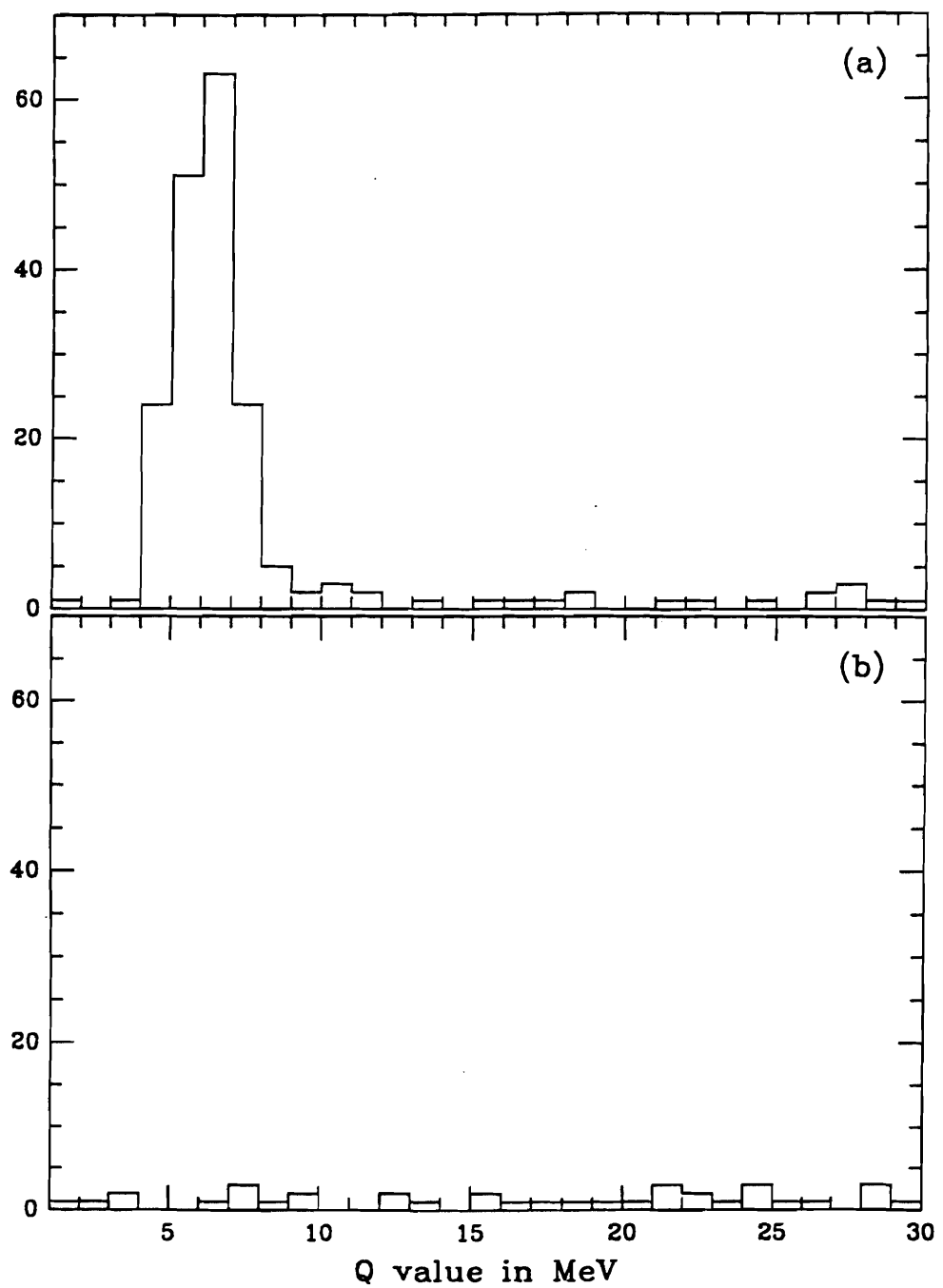


Figure 5.10 Projections of figures 5.4(a) and 5.4(b) onto Q value with the restriction $1.845 \leq M(K\pi) \leq 1.885$ GeV

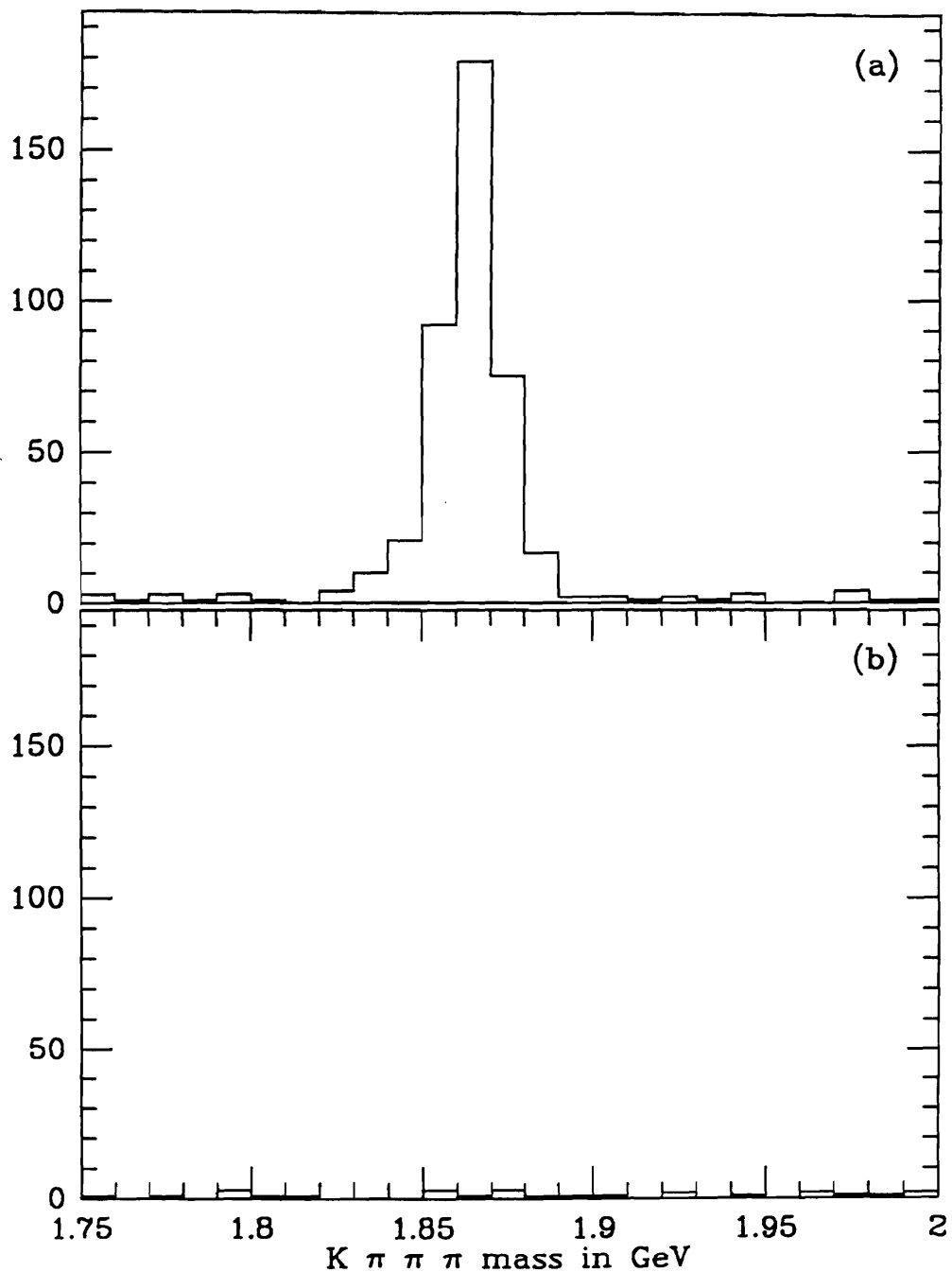


Figure 5.11 Projections of figures 5.5(a) and 5.5(b) onto $K\pi\pi\pi$ mass with the restriction $4.3 \leq Q \leq 7.3$ MeV

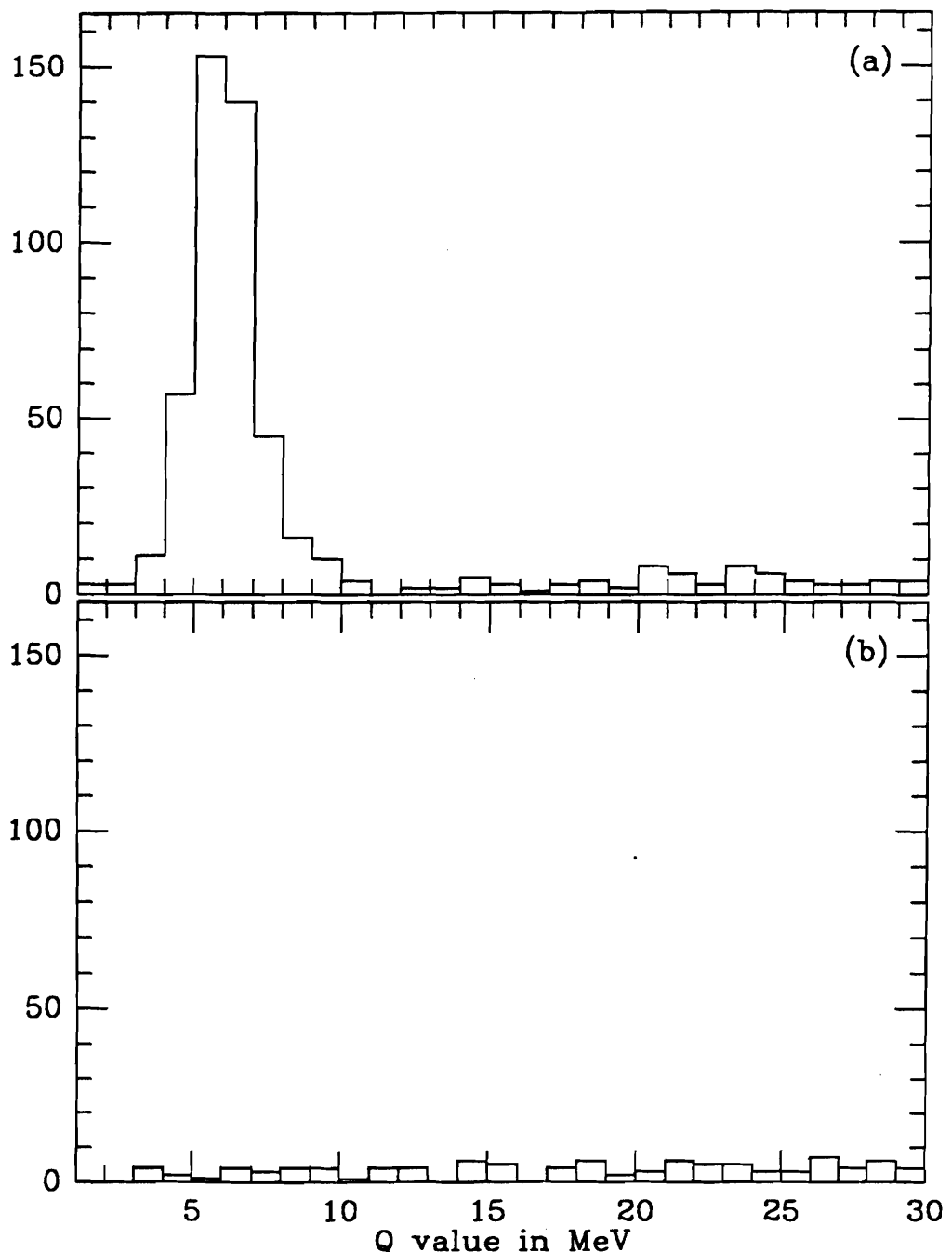


Figure 5.12 Projections of figures 5.5(a) and 5.5(b) onto Q value with the restriction $1.845 \leq M(K\pi\pi\pi) \leq 1.885$ GeV

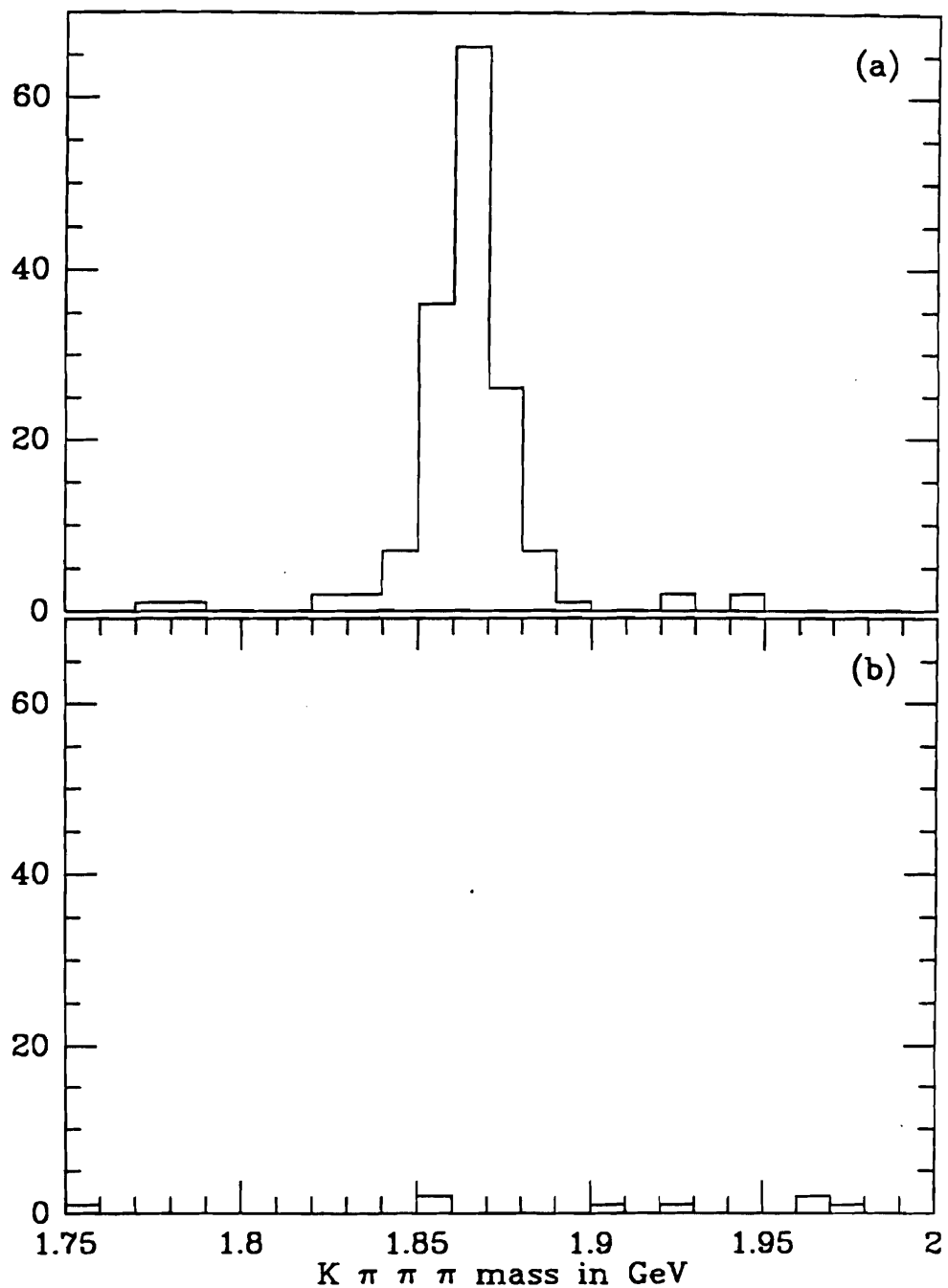


Figure 5.13 Projections of figures 5.6(a) and 5.6(b) onto $K\pi\pi\pi$ mass with the restriction $4.3 \leq Q \leq 7.3$ MeV

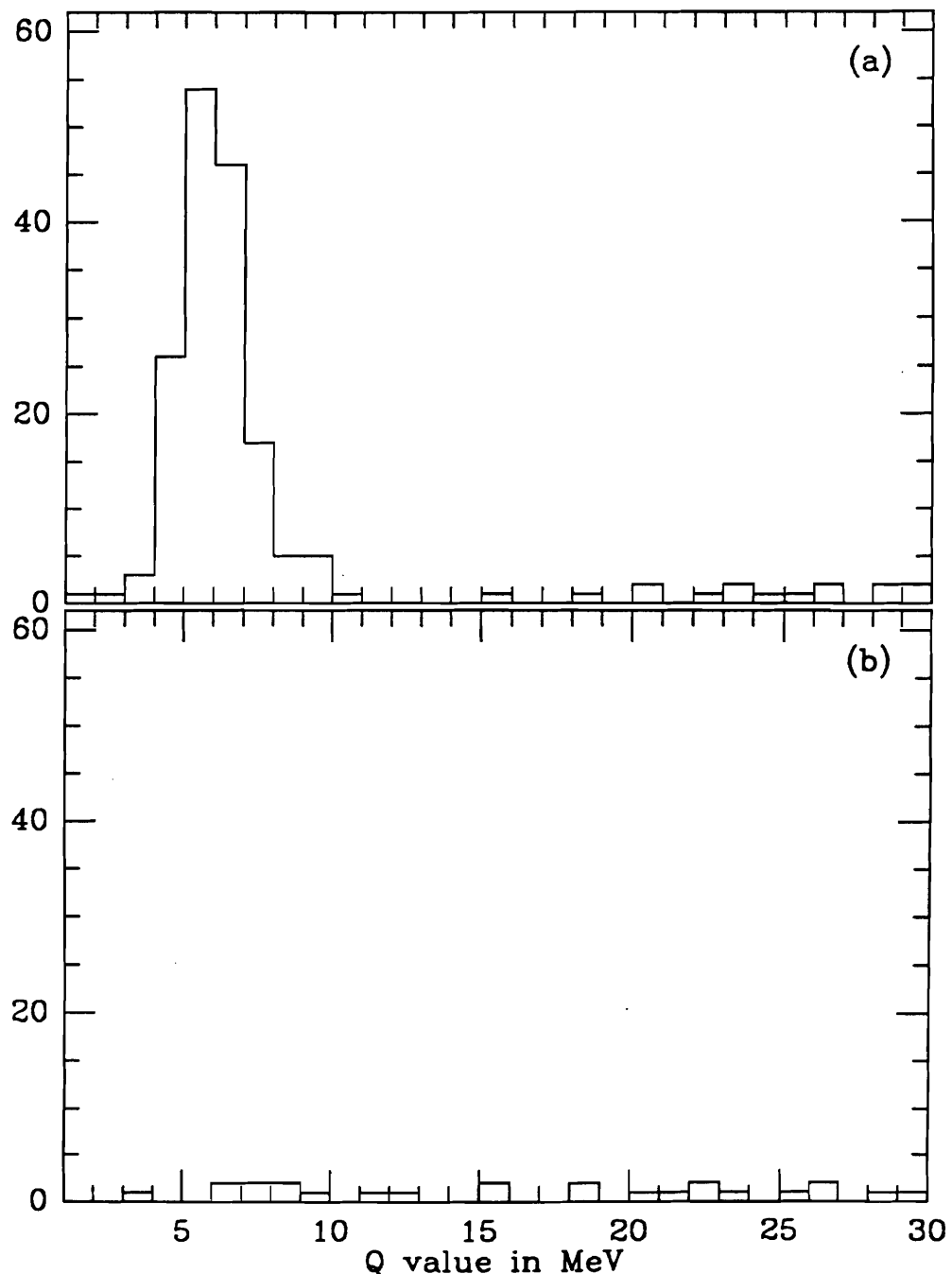


Figure 5.14 Projections of figures 5.6(a) and 5.6(b) onto Q value with the restriction $1.845 \leq M(K\pi\pi\pi) \leq 1.885$ GeV

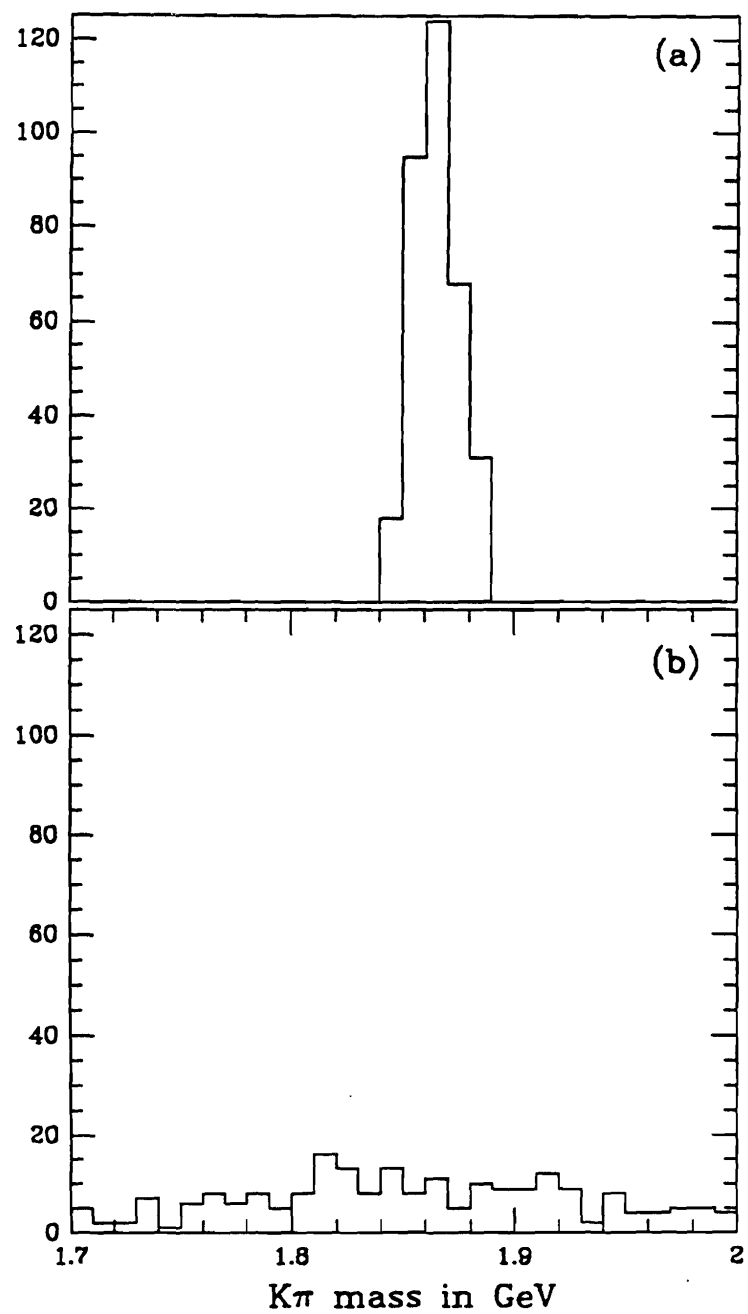


Figure 5.15 (a) Mass distribution for the $D^0 \rightarrow K^-\pi^+$ mode with the correct particle assignments (b) Mass distribution for the $D^0 \rightarrow K^-\pi^+$ mode with the kaon and the pion assignments inverted

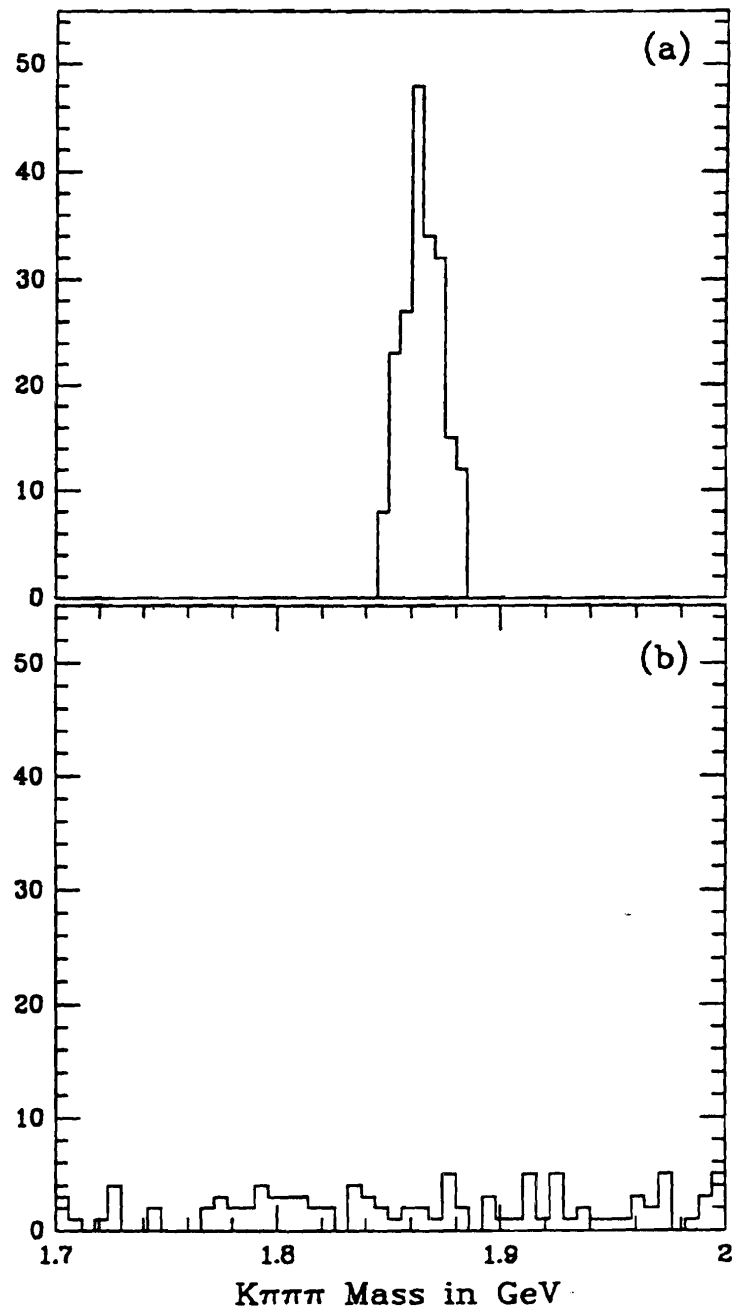


Figure 5.16 (a) Mass distribution for the $D^0 \rightarrow K^-\pi^+\pi^-\pi^+$ mode with the correct particle assignments (b) Mass distribution for the $D^0 \rightarrow K^-\pi^+\pi^-\pi^+$ mode with the particle assignments for the kaon and one of the oppositely charged pions interchanged.

decay vertex.

We compute a likelihood function $f(M, Q, t)$ for each measurement, which includes the known functional dependences of all the possible sources of signal and background on the three experimental variables. The generalised likelihood function for the entire distribution of events is given by [Fr84]:

$$L = \frac{e^{-N} N^n}{n!} \prod_{i=1}^n f'(M_i, Q_i, t_i).$$

Here n is the number of events observed, and N is the number of events expected. The function f is the probability of observing an event with $M(D^0) = M_i$, $Q = Q_i$, and $t = t_i$. The function $f'(\dots)$ is equal to the function f normalized over the interval in which the fit is performed. Using a variant of Newton's method from the CERN Minuit package, we minimize the logarithm of the likelihood function:

→ $\log L = N - \log n! - \sum_{i=1}^n \log(N f'(M_i, Q_i, t_i)).$

For the $K\pi$ mode, the right sign fitting function has the form:

$$f_{right} = f_{mix} + f_{comb} + f_{D^0+\pi} + f_{D^*} + f_{otherD^*}$$

The function f_{D^*} accounts for right sign D^* 's where the D^0 decays to the right sign $K^-\pi^+$ final state. It is a gaussian in Q value and a gaussian in $K\pi$ mass. The central value and width of the Q distribution are allowed to float. The central value of the $M(K\pi)$ distribution is taken from the Particle Data Group compilation, (which differs from our

mass scale by 0.5 MeV) while the width is allowed to float. The time distribution is given by:

$$f_{D^0}(t) \propto \exp(-t/\tau_D) f_{accept}(t)$$

$$f_{accept}(t) = (1 + at) \quad \text{if } 0.22 < t < 2.0 \text{ psec}$$

$$f_{accept}(t) = (1 + a \text{ 2.0 psec}) \quad \text{if } 2.0 \text{ psec} < t$$

The time dependent acceptance function has the same functional form as the one used in the D^0 lifetime analysis [Ra87]. The value of a is allowed to float in the right sign fit, with τ_D constrained to be 0.422 psec, as determined from the lifetime analysis [Ra87]. The Monte Carlo gives consistent results for a : $a_{MC} = 0.27 \pm 0.07$, $a_{data} = 0.22 \pm 0.12$. The final result is relatively insensitive to a : for instance changing a by ± 0.05 changes the number of mixed events by 0.15 events. The final limit is also insensitive to the $\sim 5\%$ uncertainty in the D^0 lifetime.

The function f_{mix} has a gaussian form in mass and in Q value. Its time dependence is proportional $t^2 \exp(-t/\tau)$ modified by an acceptance correction. In the right sign fit, this term is constrained to be zero. If we allow this term to float, we obtain results consistent with zero. This is a check for biases against mixing.

The function f_{comb} is linearly decreasing in $K\pi$ invariant mass and follows a phase space distribution in Q value. It is observed to follow a simple exponential time dependence with a lifetime $\tau_{comb} = (0.288 \pm 0.016) \times 10^{-12} \text{ sec.}$

The function $f_{D^0+\pi}$ is a gaussian centered at the D^0 in $K\pi$ invariant mass and follows a phase space distribution in Q value space. The

time dependence is identical to the right sign D^* events: a simple exponential modified by a factor to correct for time dependent reconstruction efficiency.

The function f_{otherD^*} is a gaussian in Q value. In $K\pi$ mass, it is well fit by a step function which is a constant from 1.75 GeV to 1.84 GeV and zero otherwise. It does not contribute to the right sign signal region. This term is not present in the wrong sign fit. Omitting this term from the fit does not effect the final result, since it does not contribute in the signal region. However, if it is omitted, the fit gives poorer agreement with the low mass background.

We use the following simple model for the phase space dependence on Q value in the f_{D^0} and f_{comb} terms. We assume that the number of states per unit interval of momentum is proportional to $p^2 d\Omega$ which implies $\frac{dN}{dQ} = Q^{\frac{1}{2}} + bQ^{\frac{3}{2}}$ where $b = \frac{-5}{4m_\pi} \sim -9.0$. The $Q^{\frac{3}{2}}$ term is the first order relativistic correction to the non-relativistic $Q^{\frac{1}{2}}$ model. We use the value of b determined from this phase space model in the fit. If b is allowed to float in the fit, we find a consistent result $b = -13.4 \pm 3.5$ (the difference may be due to the falling acceptance of the spectrometer at large Q value). Since the signal peaks at very small Q value, where all the parameterizations are nearly identical, the different possible parameterizations of the Q dependence of phase space have a negligible effect on the final result.

The wrong sign fitting function includes five terms:

$$f_{wrong} = f_{mix} + f_{comb} + f_{D^0\pi} + f_{2C} + f_{2misid}.$$

The first and fifth terms, f_{mix} and f_{2C} , account for possible contributions from mixing and DCSD. These terms have a gaussian dependence on $K\pi$ invariant mass and Q value. The mixing term has a time dependence proportional to $t^2 \exp(-t/\tau_D)$ modified by a correction for time dependent reconstruction efficiency. The DCSD term has a time dependence proportional to $\exp(-t/\tau_D)$ modified by the same acceptance correction.

The function f_{comb} has the same functional form as the corresponding term in the right sign fit. The slope of the $K\pi$ combinatorial background is determined from the fit to the right sign sample. The time dependence of this combinatorial background follows the same dependence as the combinatorial background in the right sign sample. The final result is not very sensitive to large variations in the parameterization of the background. (For instance, varying τ_{comb} in the wrong sign fit from 0.26 psec to 0.32 psec, changes N_{mix} by only 0.12 events).

The function f_{2misid} has a fixed normalization. This term accounts for double misidentification of $D^0 \rightarrow K^-\pi^+$ decays. It is approximated as a broad gaussian in $K\pi$ mass with a $\sigma = 50$ MeV, and is peaked in Q value like the D^* signal. It also follows the time dependence of the right sign D^* decays. The source of background contributes ~ 10.5 events to the full scatter plot with $t > 0.22$ psec. At most 2 events in the signal region at $t > 0.22$ psec are from this source of background. The final result is also insensitive to the precise form of this term. For instance, if the double misidentification probability is dramatically varied (from 0.8% to 1.6%), the number of mixed events changes by 4%, while the number

of DCSD events changes by 15%.

The results for the fit to the full scatter plot for $\tau > 0.22$ psec are given in tables 5.2 and 5.3.

Table 5.2 Results of a maximum likelihood fit to the right sign $K\pi$ mode.

N_{mix}	N_{comb}	$N_{D^0+\pi}$	N_{D^*}	N_{otherD^*}
0.0	427.8 ± 23.8	111 ± 15.5	708.9 ± 27.6	43.3 ± 8.4

Table 5.3 Results of a maximum likelihood fit to the wrong sign $K\pi$ mode.

N_{mix}	N_{comb}	$N_{D^0+\pi}$	$N_{2Cabibbo}$
1.2 ± 3.6	407 ± 22.2	130 ± 15.1	0.8 ± 6.0

To within statistical errors, the contributions of the $D^0+\pi$ term are the same in the right and wrong sign samples. This is consistent with the naive expectation that the probabilities of a D^0 or an anti- D^0 combining with a random pion should be roughly equal. For the $K\pi$ mode, after removing the contribution to the right sign background from D^* 's which do not decay to the $K\pi$ final state, the combinatorial backgrounds in both signs are comparable. There is no evidence for either mixing or strongly enhanced DCSD in the $K\pi$ mode.

We perform an analogous fit to the $D^0 \rightarrow K^-\pi^+\pi^-\pi^+$ mode. The right sign fit however does not include a contribution from four body decays to a non $K\pi\pi\pi$ final state. In this case, since the branching ratios

for five body semi-leptonic modes and for four body singly Cabibbo suppressed modes are small, the contribution of the misidentified reflections from such modes will also be small. This is consistent with observation; there is no significant enhancement to the left of the signal box in the right sign $K\pi\pi\pi$ scatter plot. The contribution from doubly misidentified decays is also negligible; the kinematics of the four body decay imply that less than 10% of the signal events with particle identification assignments inverted are consistent with the D^0 mass [see figure 5.14 for an illustration of this effect].

To account for the depletion of events at short times introduced by the vertex cuts, the pure exponential time distributions of the f_{D^*} term and $f_{2\text{Cabibbo}}$ term in the $D^0 \rightarrow K\pi\pi\pi$ mode are multiplied by a time dependent reconstruction efficiency function of the form $f_{\text{accept}}(t) = (1 - a e^{-bt})$. This form fits well the time distribution of both the data and Monte Carlo in the right sign. It has the property that, for large times, $f_{\text{accept}}(t)$ approaches 1.

The numerical values of a and b are determined from a fit to right sign Monte Carlo $D^* \rightarrow D^0\pi^+ \rightarrow [K^-\pi^+\pi^-\pi^+]\pi^+$ decays. We find $a_{MC} = 1.55 \pm 0.11$, $b_{MC} = 2.35 \pm 0.3$. This agrees with the result obtained by allowing a and b to float in the right sign fit : $a_{\text{data}} = 1.6 \pm 0.4$ and $b_{\text{data}} = 2.4 \pm 1.1$. The acceptance function does not turn on until $t \sim 1/b \sim 0.43$ psec. The same acceptance correction function is also included in the mixing term. The results of the fit to the scatter plot for the $K\pi\pi\pi$ mode are given in Tables 5.4 and 5.5.

Table 5.4 Results of a maximum likelihood fit to the right sign $K\pi\pi\pi$ mode.

N_{mix}	N_{comb}	$N_{D^0+\pi}$	N_{D^*}
0.0	315.5 ± 19.4	61.8 ± 11.7	434.7 ± 21.4

Table 5.5 Results of a maximum likelihood fit to the wrong sign $K\pi\pi\pi$ mode.

N_{mix}	N_{comb}	$N_{D^0+\pi}$	$N_{2Cabibbo}$
0.0 ± 3.3	243.6 ± 16.8	67.8 ± 11.0	1.6 ± 3.9

In the $K\pi\pi\pi$ mode, we also find that the numbers of D^0 's which combine with random pions are roughly equal in both signs. In contrast to the $K\pi$ mode, due to charge correlations, the combinatorial background is somewhat higher in the right sign sample. There is no evidence in this channel for either mixing or for an enhancement of DCSD.

5.4.2 Determination of Upper Limits

To determine the upper limits on mixing and DCSD, we follow the prescription of the Particle Data Group. For any parameter x which is described by a gaussian likelihood distribution with central value x_0 and width σ , and which is physically bounded by zero (e.g. in our case, the physical quantity is the number of events, which must be greater than or equal to zero.), the 90% confidence level upper limit is defined by the

integral equation:

$$\int_0^{x_{up}} G(x_0, \sigma) dx = 0.9 \int_0^{\infty} G(x_0, \sigma) dx.$$

Note that the integral is normalized over the physically allowed region. The implications of this definition are illustrated by a few examples. If the gaussian is centered at 0.0, then our prescription implies that the 90% confidence level is $x_0 + 1.64\sigma$. If the center is of the gaussian is far above zero i.e. $x_0/\sigma \gg 1$, then the 90% confidence level asymptotically approaches $x_0 + 1.28\sigma$. For a gaussian with negative central value, the upper limit will be greater than $x_0 + 1.64\sigma$.

The results of the maximum likelihood fit are for the region $t > 0.22$ psec, and must be corrected for the time dependence of the efficiency. The correction contains two components. First, we take account of losses due to the requirement $t > 0.22$ psec in the fit: only 59.3% of the pure exponential and 98% of a pure mixing decays present at $t = 0.0$ are retained by this requirement. In addition, the distribution of events for $t > 0.22$ psec in the scatter plot is reduced relative to a pure exponential by the vertex cuts. To correct for the latter effect, we must divide the detected number of D^* events by a factor F_{D^*} :

$$F_{D^*} = \frac{\int_{tcut}^{\infty} f_{accept}(t) e^{-t/\tau_D}}{\int_{tcut}^{\infty} e^{-t/\tau_D}}$$

where $f_{accept}(t)$ is the correctly normalized time dependent acceptance function and $tcut = 0.22$ psec. We apply a similar correction F_{mix} to the number of mixing events:

$$F_{mix} = \frac{\int_{tcut}^{\infty} f_{accept}(t) t^2 e^{-t/\tau_D}}{\int_{tcut}^{\infty} t^2 e^{-t/\tau_D}}$$

For the $K\pi$ mode, the correction for mixed events is small ($F_{mix} \sim 0.87$ while the correction factor to extrapolate from 0.22 psec to zero time is 0.98) and the total number is 1.4 ± 4.1 . The number of right sign D^* events is first corrected for reconstruction efficiency and then corrected from 0.22 psec to zero time. (The correction factor for reconstruction efficiency is $F_{D^*} \sim 0.77$. The correction from 0.22 psec to zero time is obtained by dividing by 0.593). Thus, the number of events corrected to zero time is 1554.1 ± 53.5 . The fraction of wrong sign decays due to mixing is then: $r_M = (1.4 \pm 4.1)/(1554.1 \pm 53.5) = .0009 \pm .0026$. The distribution for the number of mixed events is centered at 0.35σ , thus according to the PDG prescription the 90% confidence level limit is equal to $x_0 + 1.52\sigma$ which implies $r_M < 0.0050$ at the 90% confidence level. For DCSD, the fit gives 1.5 ± 11.5 events (at $t=0$) which corresponds to an upper limit of $r_{2C} < 1.5\%$ at the 90% confidence level, where r_{2C} is the ratio of wrong sign decays from the doubly Cabibbo-suppressed process to right sign decays.

In the $K\pi\pi\pi$ mode, the correction for reconstruction efficiency is much larger: here $F_{D^*} \sim 0.54$ and $F_{mix} \sim 0.83$. The final result corrected to zero time is 0.0 ± 4.0 mixed events and 1357 ± 67 right sign D^* decays. This corresponds to a limit of $r_M < .0048$ at the 90% confidence level. The fit finds 5.1 ± 12.2 DCSD events (at $t=0$), which corresponds to a limit of $r_{2C} < 1.8\%$ at the 90% confidence level.

Using the results of the fits to the two modes, we can derive a combined limit on mixing. If $r(K\pi) = r_1 \pm \sigma_1$ is the measurement of

mixing from the $K\pi$ mode and $r(K\pi\pi\pi) = r_2 \pm \sigma_2$ is the measurement of mixing from the fit to the $K\pi\pi\pi$ mode, then the correct weighted average of the mixing rate r_M is given by:

$$\frac{r_M}{\sigma^2} = \frac{r_1}{\sigma_1^2} + \frac{r_2}{\sigma_2^2}$$

where $\frac{1}{\sigma^2} = \frac{1}{\sigma_1^2} + \frac{1}{\sigma_2^2}$. We thus find $r_M = 0.0005 \pm .0020$ or $r_M < .0037$ at the 90% confidence level.

5.5 Fits with interference

As discussed in Chapter 1, there is the possibility of interference between the mixing amplitude and the DCSD amplitude. This interference introduces an additional term in the time dependence of wrong sign decays which is proportional to $\Delta\Gamma\rho te^{-t/\tau}$. If the product $\Delta\Gamma\rho > 0$, then this term will produce larger excesses at long times. Conversely, if $\Delta\Gamma\rho < 0$ and the strength of mixing and DCSD are precisely matched at $2\tau_{D^0}$, the interference term could cancel the mixing term and wipe out the excess of events at long times which is the signature of mixing [Figure 5.17 shows two examples of the possible scenarios with large interference].

In the limit of no CP violation, we found (see Chapter I, page 14) that the rate for wrong-sign decays had the following form:

(5.2)

$$I(D^0 \rightarrow K^+\pi^-) = e^{-\Gamma t} \left\{ \frac{t^2}{4} [(\Delta M)^2 + (\frac{1}{2}\Delta\Gamma)^2] + |\rho|^2 + t[\frac{1}{2}(\Delta\Gamma)\rho] \right\}.$$

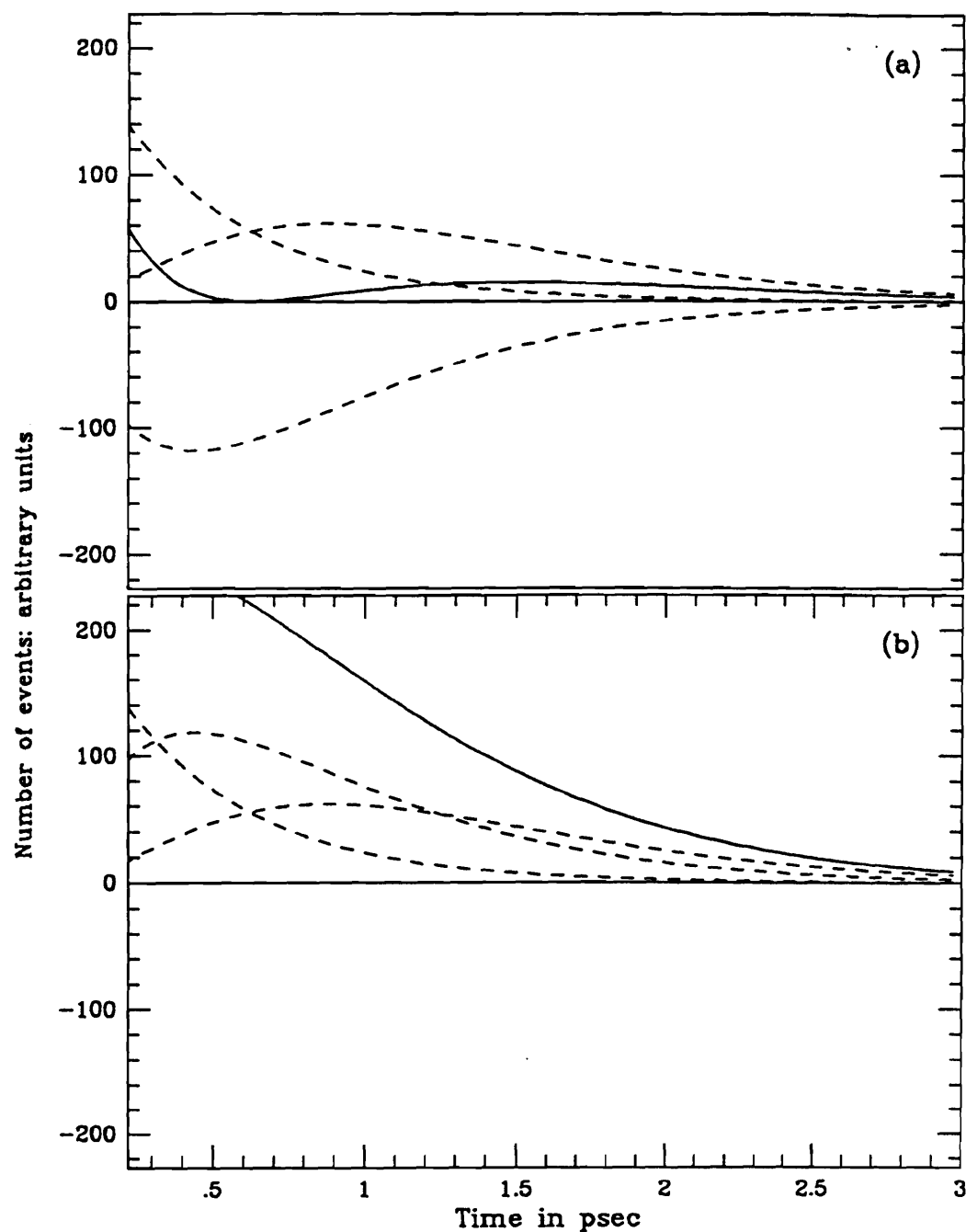


Figure 5.17 (a) $\Delta\Gamma\rho < 0$ maximal destructive interference with a large DCSD amplitude. (b) $\Delta\Gamma\rho > 0$ constructive interference with a large DCSD amplitude. The dotted lines represent the contributions of mixing, DCSD, and interference. The solid line represents the sum of these contributions.

This can be rewritten in a more transparent form if we use the definitions

$$N_{mix} = r_M \Gamma^2 / 2 = \frac{1}{4}(\Delta M)^2 + \frac{1}{4}(\Delta \Gamma)^2, \quad N_{2C} = r_{2C} \Gamma = |\rho|^2, \text{ and}$$

$$\cos \phi = \frac{\Delta \Gamma / 2}{\sqrt{(\Delta M)^2 + (\Delta \Gamma / 2)^2}} = \frac{y}{\sqrt{x^2 + y^2}}.$$

The strength of the interference term is thus proportional to $\sqrt{r_{2C}} \sqrt{r_M} \cos \phi$

and equation (5.2) can then be rewritten as:

$$I(D^0 \rightarrow K^+ \pi^-) = N_{mix} t^2 e^{-t/\tau} + N_{2C} e^{-t/\tau} + 2\sqrt{N_{mix}} \sqrt{N_{2C}} \cos \phi t e^{-t/\tau}.$$

In the full maximum likelihood fit, we must take into account the fact that the normalizations of the mixing and of the DCSD term fix the normalization of the interference term. Thus, the normalized likelihood function becomes:

$$f'_{wrong} = \frac{N_{mix}}{C_{mix}} f_{mix} + \frac{N_{2C}}{C_{2C}} f_{2C} + 2 \frac{\sqrt{N_{mix} N_{2C}}}{\sqrt{C_{mix} C_{2C}}} \cos \phi f_{accept}(t) t e^{-t/\tau}$$

where N_{mix}, N_{2C} are the numbers of mixing and DCSD events, respectively. The constants C_{mix}, C_{2C} are the normalizations for the mixing and DCSD terms, respectively.

The limits on r_M and r_{2C} are determined from the conservative non-parabolic maximum likelihood errors. The limits on r are derived from the 90% confidence contours on 2 dimensional plots of the likelihood as a function of the number of mixed events and the number of doubly Cabibbo suppressed events. The results of the fit for some representative values of the interference phase $\cos \phi$ are given in Tables 5.6 and 5.7.

In the $K\pi$ mode, large mixing and large DCSD with complete destructive interference are compatible with the data. For less than complete destructive interference, $r_M \sim 1\%$ can be ruled out. For the $K\pi\pi\pi$

Table 5.6 Limits on mixing in the case of interference for the $K\pi$ mode at the 90% C.L.

$\cos \phi$	r_M	r_{2C}	r
1.0	1.9%	4.9%	3.4%
0.5	0.6%	1.8%	1.8%
0.0	0.5%	1.5%	1.5%
-0.5	0.5%	1.6%	1.6%
-1.0	0.5%	1.6%	1.6%

Table 5.7 Limits on mixing in the case of interference for the $K\pi\pi\pi$ mode at the 90% C.L.

$\cos \phi$	r_{mix}	r_{2C}	r_{tot}
1.0	0.7%	3.3%	2.6%
0.5	0.6%	2.2%	2.2%
0.0	0.5%	1.8%	1.8%
-0.5	0.5%	1.8%	1.8%
-1.0	0.4%	1.8%	1.8%

channel, even in the most extreme case, r_M must be less than 0.7%. In the case of constructive interference, the limits become slightly better.

There are a number of reasons why a scenario with maximal destructive interference is unlikely. It would require a large $|\Delta\Gamma|$, but a small value of ΔM . Most predictions from the box diagram and from extensions of the Standard Model suggest that $\Delta M \gg \Delta\Gamma$, due to the large amount of phase space available for D^0 decays. Models with long

distance non-perturbative enhancements suggest that $\Delta M \sim \Delta \Gamma$. In addition, the sign of $\Delta \Gamma \rho$ must be negative, although a simple theoretical estimate (see Chapter 1) suggests that $\Delta \Gamma \rho$ is positive⁹. To properly mask the effect of mixing near $t \approx 2/\Gamma$, r_{2C} must be roughly a few percent, or $10 \tan^4 \theta_c$. This would be a surprising deviation from the standard picture of Cabibbo suppression, since it would suggest that the rate for doubly Cabibbo suppressed decays is comparable to rate for singly Cabibbo suppressed decays. Finally, this greatly enhanced r_{2C} would have to be the same in both modes, in contrast to the situation in the measured singly Cabibbo suppressed modes where some modes are enhanced while others are suppressed. Although some theoretical predictions (see [Bi87] and the last chapter of this thesis) suggest modest enhancements of DCSD in particular (PP) modes, these enhancements are offset by suppression in other modes (PV) modes, as expected from duality. Finally, we remark that other experiments which seek to constrain the strength of mixing by studying wrong sign hadronic D^0 modes without decay time information measure only $r = r_M + r_{int} + r_{2C}$ and are thus even less sensitive to mixing in this pathological case.

5.6 Summary

We observe no evidence of mixing in the $D^0 \rightarrow K\pi$ and $D^0 \rightarrow K\pi\pi\pi$ modes, and measure the parameter $r_M = .0005 \pm .0020$ corresponding to the limit $r_M < .0037$ at the 90% confidence level. This result is inconsistent with the result $r_M \sim 1\%$ suggested by the anomalous MarkIII

events. We also find limits on DCSD decays: $B(D^0 \rightarrow K^+ \pi^-) < 0.06\%$ and $B(D^0 \rightarrow K^+ \pi^- \pi^+ \pi^-) < 0.15\%$ at the 90% confidence level.

6

Conclusions

We have searched for $D^0 - \overline{D^0}$ mixing in two decay channels. We have found no evidence for either mixing or strongly enhanced DCSD. The combined limit on mixing from the two modes is $r_M < 0.37\%$. This rules out the value $r_M \sim 1\%$ suggested by the anomalous Mark III events. This limit is above the level expected in most estimates of long distance effects, but is below the theoretical upper limit (due to Wolfenstein) $r_M < 0.5\%$.

We have also performed an analysis of mixing allowing for the possibility of mixing dominated by $\Delta\Gamma$ and large interference effects. In the $K\pi$ mode, we found that except for $\cos\phi \sim 1.0$, we can rule out mixing at the 1% level. In the $K\pi\pi\pi$ mode, even this possibility can be ruled out for all choices of the interference phase. We have also presented an argument to show that a scenario with maximal destructive interference is unlikely.

In addition, we have found limits for DCSD decays: $B(D^0 \rightarrow (K^+\pi^-) < 0.06\%$ and $B(D^0 \rightarrow K^+\pi^-\pi^+\pi^-) < 0.15\%$ at the 90% confidence level. Using the Bauer-Stech formalism, Bigi has computed the rate for $D^0 \rightarrow K^+\pi^-$. This formalism gives a calculational procedure for determining all D meson branching ratios. It assumes a phenomeno-

logical Lagrangian form with two adjustable coefficients, which are determined from a fit to the measured D^0 branching ratios, and a factorization Ansatz [Bi87]. With these assumptions, one finds $r_{2C}(K\pi) \approx 2 \tan^4 \theta_c$ and $r_{2C}(K\pi\pi\pi) \approx 0.5 \tan^4 \theta_c$. Thus as we discussed in chapter 5, the Bauer-Stech formalism predicts that certain DCSD modes are enhanced, while others are suppressed. For comparison, our upper limit corresponds to $r_{2C}(K\pi) < 5 \tan^4 \theta_c$ and $r_{2C}(K\pi\pi\pi) < 6 \tan^4 \theta_c$. No predictions are yet available for the rate of $D^0 \rightarrow K^+ \pi^- \pi^+ \pi^-$. The limits for DCSD are thus consistent with estimates based on the Bauer-Stech formalism and still far above the level expected in the naive spectator model.

The limits on mixing that we have derived imply constraints on flavor changing neutral currents (FCNC) in non-standard models. For instance, a treatment by Bigi, Kopp, and Zerwas [Bi86] of models in which new vector bosons induce mixing or FCNC effects gives the following general result for D mixing:

$$\Delta M_D/M_D = \frac{2}{3} \frac{g_H^2}{m_H^2} [4\pi/\Lambda_H^2] R_D |f_D|^2.$$

Here g_H and m_H are the coupling and the mass of the new horizontal boson while Λ_H is the mass scale for the new boson. R_D is the bag constant and f_D is the D meson decay constant. Using reasonable guesses for R_D and f_D and our limit on mixing as the input for ΔM_D , one obtains the following model dependent limits on the mass of horizontal bosons:

$$m_H \geq 520 \text{ TeV} \times g_H, \quad \Lambda_H \geq 2 \times 10^3 \text{ TeV}$$

We are thus able to constrain new physics at an energy far beyond the

center of mass energy that is directly accessible at proton-antiproton colliders.

In four generation models, the mixing limit can also be used to constrain the masses of fourth generation quarks. For instance, the limit $r_M < 0.37\%$ in the four generation framework of Bjorken and Dunietz [Bj87] implies $m_{B^*} \leq 100 \text{ GeV}$, where m_{B^*} refers to the lower member of the hypothetical fourth quark doublet. In this model, the $D^0 - \overline{D^0}$ mixing limit is the only experimental constraint on the lower member of the fourth quark doublet.

Complementary studies which also seek to constrain extensions of the Standard model have been undertaken. These include searches for flavour changing neutral currents in purely leptonic decays. Examples of such decays include $D^0 \rightarrow \mu e$, $D^0 \rightarrow \mu^+ \mu^-$, $D^0 \rightarrow e^+ e^-$, $D^+ \rightarrow \pi^+ \mu^- e^+$ etc.. These FCNC decays may occur in technicolor models, models with additional Higgs doublets, models with horizontal gauge bosons, and some superstring motivated phenomenologies (e.g. $D^0 \rightarrow \mu e$ induced by lepto-quarks is favored in the latter speculations). Limits on FCNC in kaon decays are typically 10^4 times more stringent than the corresponding limits for rare D decays. It is nevertheless conceivable that FCNC could be enhanced for transitions between upper members of the weak doublets (especially if the couplings are mass dependent) and suppressed for the lower members [Bu86],[Buc86],[Kr88].

K. Sliwa has performed a search for the FCNC D decays listed above. Using half of the E691 data sample, he finds no evidence for any of

these modes and derives the 90% confidence level limits, which are given in table 6.1.

Table 6.1 Limits on rare D meson decays.

Decay mode	E-691 limit	existing limit
$D^0 \rightarrow e^+ e^-$	8×10^{-5}	none
$D^0 \rightarrow \mu^+ \mu^-$	1×10^{-4}	1.1×10^{-5} ^a
$D^0 \rightarrow \mu^+ e^-$	8×10^{-5}	1.5×10^{-4} ^{b,c,d}
$D^+ \rightarrow \pi^+ \mu^+ e^-$	2×10^{-4}	none

- (a) This limit is from Fermilab experiment E615
- (b) This limit is from the Mark III collaboration
- (c) The ACCMOR collaboration has derived a limit of 1.0×10^{-3} for this mode.
- (d) The Mark II collaboration has derived a limit of 2.1×10^{-3} for this mode.

The limits on the FCNC modes from E-691 are better than those from all previous experiments except for the $D^0 \rightarrow \mu^+ \mu^-$ mode for which the dedicated Fermilab di-muon experiment E615 has derived a better limit. The limits on these rare decays can again be used to derive model dependent constraints on the couplings and masses of hypothetical particles in theoretical extensions of the Standard Model [Bu86].

It should be noted that the purely leptonic decay modes discussed above, with the exception of $D^+ \rightarrow \mu^+ e^- \pi^+$, are helicity suppressed. At the present time, the limits on these decays are comparable to the limits on Standard Model allowed helicity suppressed decays such as $D^+ \rightarrow \mu \nu$.

In the near future, we plan to search for other non-helicity suppressed decays such as $D^0 \rightarrow \mu e \pi^+ \pi^-$, $D^0 \rightarrow e^+ e^- \pi^+ \pi^-$ and $D^0 \rightarrow \mu^+ \mu^- \pi^+ \pi^-$. Since we can apply the vertex cuts developed for multibody decay modes, we may be more sensitive to these decays. These decays should also have intrinsically higher branching ratios.

We also plan to search for evidence of enhanced DCSD in other decays, including the $D^+ \rightarrow K^+ \pi^- \pi^+$ mode. In this case, the signature of DCSD is unique; there is no mixing for charged D decays. In addition, we will attempt studies of wrong sign $D^0 \rightarrow K^- \pi^+ \pi^0$ decays. Although modes which contain π^0 's have much larger experimental backgrounds, a measurement of the $K\pi\pi^0$ mode could provide more direct comparisons with the Mark III results.

6.1 Prospects for future experiments

In this thesis we have introduced a new method for the study of mixing in charmed mesons. Using the fine grain decay time resolution of the SMDs, we are able to separate mixing from DCSD and from backgrounds. The method may be refined in future experiments, but it is still inherently limited by DCSD. If mixing is too small, it will be swamped by the long lived tail of the DCSD spectrum, even with the time separation. At two D^0 lifetimes, where we are most sensitive to mixing, roughly 14% of DCSD decays and 68% of mixing decays remain. Therefore, using this method, mixing below about the 0.05% level is probably unobservable. In principle, future experiments could attain even higher sensitivities by

studying mixing in semi-leptonic decay modes for which DCSD processes do not contribute. In practice, however, such modes also have higher backgrounds.

The dominant source of experimental backgrounds at long times, D^0 's which combine with random pions, may be reduced somewhat with finer vertex resolution. The majority of these random pions, however, originate in the primary vertex; increases in statistics can thus only improve the limit by $1/\sqrt{f}$, where f is the factor by which the number of events is increased.

Finally, we note that if a method of triggering on beauty mesons at fixed target and hadron collider experiments can be devised, then future experiments may apply the methods discussed in this thesis. Using reconstructed time information from silicon vertex detectors, one may separate B mixing from backgrounds.

Appendix I

In this appendix, we list the cuts used in the stripping, substripping, and analysis of mixing in tabular form. These cuts are discussed in Chapter 5.

The variable DOF is the number of degrees of freedom of a track. JCATSG is the category of the track - it is described in Chapter 3. The variable NVV is the number of vertices in the event. CPRB2 is the Cerenkov probability for a track, and ranges from 0 to 1 for each particle assignment. EMPROB2 is the electron probability. It may take on values between 0 and 100. Both CPRB2 and EMPROB2 are discussed in Chapter 3. χ^2_{primary} , $\chi^2_{\text{secondary}}$ are the χ^2 per degree of freedom for the primary and for the secondary vertex as determined in the vertex reconstruction. DIP is the transverse miss distance of the D^0 momentum vector with respect to the primary vertex. RATPI is the transverse miss distance of the slow pion with respect to the primary. DIP2 is the distance of closest approach of the slow pion and the D^0 momentum vector. The cuts on the z position of the primary vertex simply require the primary vertex to lie inside the target.

Table a.1 Cuts used in the $K\pi$ strip

Type of Cut	Acceptable range
DOF per track	> 11.5
JCATSG for kaon and pion tracks	[3,15]
$K\pi$ product Cerenkov probability	≥ 0.3
momentum of each track	< 250 GeV
$K\pi$ invariant mass	[1.6,2.1] GeV
Q value	none
Vertex cuts	none

Table a.2 Cuts used in the $K\pi$ substripper

Type of Cut	Acceptable range
DOF per track	11.5
JCATSG for kaon and pion tracks	[3,15]
$K\pi$ product Cerenkov probability	≥ 0.3
$K\pi$ invariant mass	[1.7,2.1] GeV
Vertex cuts	
SDZ	> 3.0
$\chi^2_{primary}$	< 3.0
$\chi^2_{secondary}$	$< 10.$
DIP	$< 120\mu m$

Table a.3 Cuts used in the $K\pi\pi\pi$ substrip

Type of Cut	Acceptable range
DOF per track	11.5
JCATSG for kaon and pion tracks	[5,15]
$K\pi\pi\pi$ product Cerenkov probability	≥ 0.2
momentum of each track	[3, 250] GeV
$K\pi\pi\pi$ invariant mass	[1.75,2.0] GeV
Q value	none
Vertex cuts	
SDZ	> 6.0
DIP	$< 100\mu m$
Extra tracks	No more than 1 within $80\mu m$
$\chi^2_{primary}$	< 3.0
Z position of the primary	[-7.0, 1.5] cm
$\chi^2_{secondary}$	< 4.5

Table a.4 Cuts used in the $K\pi$ analysis job

Type of Cut	Acceptable range
Momentum for tracks	[3.0,250.] GeV
JCATSG for kaon and pion tracks	[5,15]
EMPROB2 for the kaon	< 90.
$K\pi$ product Cerenkov probability	≥ 0.3
$K\pi$ invariant mass	[1.75,2.0] GeV
D^0 momentum	[35.,100.] GeV
JCATSG for slow pion	[3,15]
CPRB2 for slow pion	0.4
Q value	[0.0,30.0] MeV
Vertex cuts	
τ	> 0.22 psec
$\chi^2_{primary}$	< 3.0
$\chi^2_{secondary}$	< 3.5
DIP	< $80\mu m$
DIP2	< $120\mu m$
RATPI	< $250\mu m$
NVV	< 7
$Z_{primary}$	[-6.,-0.5] cm

Table a.5 Cuts used in the $K\pi\pi\pi$ analysis job

Type of Cut	Acceptable range
$K\pi\pi\pi$ product Cerenkov probability	≥ 0.3
$K\pi\pi\pi$ invariant mass	[1.75,2.0] GeV
p_{D^0}	> 43 GeV
DOF slow pion	> 11.5
JCATSG slow pion	[3,15]
CPRB2 slow pion	> 0.3
Q value	[0.,30.] MeV
Vertex cuts	
Slow pion passes through the primary	
τ	> 0.22
DIP	$< 65\mu m$
Extra tracks	None within $80\mu m$
RATBIG	< 1.5
NVV	< 9
Z position of the primary	[-6.0, 1.0] cm
$\chi^2_{secondary}$	< 3.5

Appendix II

In this appendix, we derive the full time dependence of wrong sign hadronic D^0 decays.

For a state which is initially all D^0 at $t = 0$,

$$\psi_+(t) = f_+(t)|D^0\rangle + \alpha f_-(t)|\overline{D^0}\rangle$$

where

$$f_{\pm}(t) = \frac{1}{2} e^{-\gamma_1 t/2} e^{-im_1 t} [1 \pm e^{-\Delta\Gamma t/2} e^{-i\Delta m t}].$$

The rate of wrong sign $D^0 \rightarrow K^+ \pi^-$ decays is given by the overlap integral $| \langle K^+ \pi^- | \psi_+(t) \rangle |^2$. This overlap integral can be rewritten in terms of the amplitudes $\langle K^+ \pi^- | D^0 \rangle$, $\langle K^+ \pi^- | \overline{D^0} \rangle$ and then simplified. We find:

$$I[D^0 \rightarrow K^+ \pi^-](t) = | \langle K^+ \pi^- | D^0 \rangle f_+(t) + f_-(t) \langle K^+ \pi^- | \overline{D^0} \rangle |^2$$

$$= | \langle K^+ \pi^- | \overline{D^0} \rangle |^2 \left| \frac{\langle K^+ \pi^- | D^0 \rangle}{\langle K^+ \pi^- | \overline{D^0} \rangle} f_+(t) + \alpha f_-(t) \right|^2$$

If we choose units in which $\langle K^+ \pi^- | D^0 \rangle = 1$ and define $\frac{\langle K^+ \pi^- | D^0 \rangle}{\langle K^+ \pi^- | \overline{D^0} \rangle} =$

$\tan^2 \theta_c \hat{\rho}_f$ then:

$$\begin{aligned}
 I[D^0 \rightarrow K^+ \pi^-](t) &= |\tan^2 \theta_c \hat{\rho}_f f_+(t) + \alpha f_-(t)|^2 \\
 &= \{ \tan^4 \theta_c |\hat{\rho}_f|^2 f_+(t) f_+^*(t) + \alpha \tan^2 \theta_c \hat{\rho}_f f_-(t) f_+^*(t) \\
 &\quad + \alpha^* \tan^2 \theta_c \hat{\rho}_f f_+(t) f_-^*(t) + \alpha^2 f_-(t) f_-^*(t) \}
 \end{aligned}$$

In order to obtain the final result, we need to compute four quantities. These quantities are $f_+(t) f_+^*(t)$, $f_-(t) f_+^*(t)$, $f_+(t) f_-^*(t)$ and $f_-(t) f_-^*(t)$. The approximation that $\frac{\Delta M}{\Gamma}$, $\frac{\Delta \Gamma}{\Gamma} \ll 1$ will be used, since D mixing is much less than maximal. We will also assume that $|\hat{\rho}_f|^2 \tan^4 \theta_c \ll 1$ and then retain all terms up to second order in small quantities.

$$\begin{aligned}
 f_+(t) f_+^*(t) &= \frac{1}{4} e^{-\gamma_1 t} (1 + e^{-\Delta \Gamma t/2} e^{-i \Delta m t}) (1 + e^{-\Delta \Gamma t/2} e^{i \Delta m t}) \\
 &= \frac{1}{4} e^{-\gamma_1 t} \{ 1 + e^{-\Delta \Gamma t/2} (e^{i \Delta m t} + e^{-i \Delta m t}) + e^{-\Delta \Gamma t} \} \\
 &\approx \frac{1}{4} e^{-\gamma_1 t} \{ 1 + (1 - \Delta \Gamma t/2 + \frac{1}{2} \frac{1}{4} (\Delta \Gamma t)^2) 2 (1 - \frac{1}{2} (\Delta m t)^2) \\
 &\quad + (1 - \Delta \Gamma t + \frac{1}{2} (\Delta \Gamma t)^2) \} \\
 &\approx \frac{1}{4} e^{-\gamma_1 t} (4 - \Delta \Gamma t - \Delta \Gamma t + \frac{3}{4} (\Delta \Gamma t)^2 - (\Delta m t)^2) \\
 &\approx \frac{1}{4} e^{-\gamma_1 t} (4 - 2 \Delta \Gamma t)
 \end{aligned}$$

Since $f_+(t) f_+^*(t)$ is multiplied by $\tan^4 \theta_c$, at the last step we retain only terms which are linear in Δm and $\Delta \Gamma$.

$$\begin{aligned}
f_-(t)f_-^*(t) &= \frac{1}{4}e^{-\gamma_1 t}(1 - e^{-\Delta\Gamma t/2}e^{-i\Delta m t})(1 - e^{-\Delta\Gamma t/2}e^{i\Delta m t}) \\
&= \frac{1}{4}e^{-\gamma_1 t}\{1 - e^{-\Delta\Gamma t/2}(e^{i\Delta m t} + e^{-i\Delta m t}) + e^{-\Delta\Gamma t}\} \\
&\approx \frac{1}{4}e^{-\gamma_1 t}\{1 - (1 - \Delta\Gamma t/2 + \frac{1}{2}\frac{1}{4}(\Delta\Gamma t)^2)2(1 - \frac{1}{2}(\Delta m t)^2) \\
&\quad + (1 - \Delta\Gamma t + \frac{1}{2}(\Delta\Gamma t)^2)\} \\
&\approx \frac{1}{4}e^{-\gamma_1 t}(1 - 2 + 1 - \Delta\Gamma t + \Delta\Gamma t + \frac{1}{4}(\Delta\Gamma t)^2 + (\Delta m t)^2) \\
&\approx \frac{1}{4}e^{-\gamma_1 t}((\Delta m t)^2 + \frac{1}{4}(\Delta\Gamma t)^2)
\end{aligned}$$

$$\begin{aligned}
f_+(t)f_-^*(t) &= \frac{1}{4}e^{-\gamma_1 t}(1 + e^{-\Delta\Gamma t/2}e^{-i\Delta m t})(1 - e^{-\Delta\Gamma t/2}e^{i\Delta m t}) \\
&= \frac{1}{4}e^{-\gamma_1 t}\{1 - e^{-\Delta\Gamma t/2}(e^{i\Delta m t} - e^{-i\Delta m t}) - e^{-\Delta\Gamma t}\} \\
&\approx \frac{1}{4}e^{-\gamma_1 t}\{1 - (1 - \Delta\Gamma t/2 + \frac{1}{2}\frac{1}{4}(\Delta\Gamma t)^2)(2i\Delta m t) \\
&\quad - (1 - \Delta\Gamma t + \frac{1}{2}(\Delta\Gamma t)^2)\} \\
&\approx \frac{1}{4}e^{-\gamma_1 t}(\Delta\Gamma t - \frac{1}{2}(\Delta\Gamma t)^2 - 2i(\Delta m t)) \\
&\approx \frac{1}{4}e^{-\gamma_1 t}(\Delta\Gamma t - 2i\Delta m t)
\end{aligned}$$

At the last step, we dropped second order terms proportional to $(\Delta\Gamma)^2\hat{\rho}_f \tan^2 \theta_c$ and $\Delta\Gamma \Delta m \hat{\rho}_f \tan^2 \theta_c$.

$$\begin{aligned}
f_-(t)f_+^*(t) &= \frac{1}{4}e^{-\gamma_1 t}(1 - e^{-\Delta\Gamma t/2}e^{-i\Delta m t})(1 + e^{-\Delta\Gamma t/2}e^{i\Delta m t}) \\
&= \frac{1}{4}e^{-\gamma_1 t}\{1 - e^{-\Delta\Gamma t/2}(e^{i\Delta m t} - e^{-i\Delta m t}) - e^{-\Delta\Gamma t}\} \\
&\approx \frac{1}{4}e^{-\gamma_1 t}\{\Delta\Gamma t - \frac{1}{2}(\Delta\Gamma t)^2 + 2i(\Delta m t)\} \\
&\approx \frac{1}{4}e^{-\gamma_1 t}\{\Delta\Gamma t + 2i(\Delta m t)\}
\end{aligned}$$

Combining these results, we have:

$$\begin{aligned}
 I[D^0 \rightarrow K^+ \pi^-](t) &= \frac{1}{4} e^{-\gamma_1 t} \{ \tan^4 \theta_c |\rho_f|^2 (4 - 2\Delta\Gamma t) \\
 &\quad + \tan^2 \theta_c \hat{\rho}_f \alpha (\Delta\Gamma t + 2i(\Delta m t)) \\
 &\quad + \tan^2 \theta_c \hat{\rho}_f^* \alpha^* (\Delta\Gamma t - 2i(\Delta m t)) \\
 &\quad + |\alpha|^2 ((\Delta m t)^2 + \frac{1}{4} (\Delta\Gamma t)^2) \} \\
 &= \frac{1}{4} e^{-\gamma_1 t} \{ \tan^4 \theta_c |\hat{\rho}_f|^2 (4 - 2\Delta\Gamma t) \\
 &\quad + |\alpha|^2 ((\Delta m t)^2 + \frac{1}{4} (\Delta\Gamma t)^2) \\
 &\quad + \tan^2 \theta_c (\hat{\rho}_f \alpha + \hat{\rho}_f^* \alpha^*) (\Delta\Gamma t) \\
 &\quad + \tan^2 \theta_c (\hat{\rho}_f \alpha - \hat{\rho}_f^* \alpha) 2i(\Delta m t) \}
 \end{aligned}$$

Now we use the identities: $\text{Re } \alpha = \frac{\alpha + \alpha^*}{2}$ and $\text{Im } \alpha = \frac{\alpha - \alpha^*}{2i}$ to

obtain:

$$\begin{aligned}
 I[D^0 \rightarrow K^+ \pi^-](t) &= \frac{1}{4} e^{-\gamma_1 t} \{ 4 \tan^4 \theta_c |\hat{\rho}_f|^2 \\
 &\quad + |\alpha|^2 ((\Delta m t)^2 + \frac{1}{4} (\Delta\Gamma t)^2) \\
 &\quad + 2 \tan^2 \theta_c \text{Re}(\hat{\rho}_f \alpha) \Delta\Gamma t \\
 &\quad - 4 \tan^2 \theta_c \text{Im}(\hat{\rho}_f \alpha) \Delta m t \}
 \end{aligned}$$

Note that we have dropped the term proportional to $\Delta\Gamma \tan^4 \theta_c$ which is third order in a small quantity. If we repeat this exercise with a wave function which is initially a pure $\overline{D^0}$ state at zero time, the last term (proportional to $\Delta m t$) changes sign. Thus we obtain the desired result.

REFERENCES

Ab86 S.Abachi et al., ANL-HEP-PR-86-100, July (1986).

Al84 W.Altohoff et al., *Phys. Lett.* **138B**, (1984), 317.

Al87 H. Albrecht et al., *Phys. Lett.* **199B**, (1987), 447.

An82 P. D'Angelo et al., *Nucl. Instr. Meth.*, **193**, (1982), 533.

An85 A.A. Anselm, J.L. Chkareuli, N.G. Uralstev, T.A. Zhukovskaya *Phys. Lett.* **156B**, (1980) 1,2.

Ap86 J.Appel,P.Mantsch,M.Streetman,R.Robertson, *Nucl. Instr. Meth.* **A243**, (1986), 361.

Au81 J.J.Aubert et al., *Phys. Lett.* **106B**, (1981), 419.

Av80 P.Avery et al., *Phys. Rev. Lett.* **44**, (1980), 1309.

Ba82 V.Barger,W.Y.Keung,R.J.N.Phillips, *Phys. Rev.* **D25**, (1982), 1803.

Ba83 R.Bailey et al., *Phys. Lett.* **132B**, (1983), 237.

Ba85 M.Bauer,B.Stech, *Phys. Lett.* **152B**, (1985), 380.

Ba86 D.Bartlett et al., *Performance of the Čerenkov Counters in the Fermilab Tagged Photon Facility*, preprint Colo-HEP-121, (1986).

Ba87 G. Barber et al., *Nucl Instr. Meth.* **A253**, (1987), 530

Bar86 I. Bars, *Tests for Composite Quarks and Leptons*, Proceedings of the XXIII International Conference on High Energy Physics, World Scientific (1987).

Be73 G. Bellini et. al., *Nucl. Instr Meth.* **107**, (1973), 85.

Be85 A.Benvenuti et al., *Phys. Lett.* **158B**, (1985), 531.

Be86 A.Bean, *Limits on $B^0\overline{B^0}$ Mixing and τ_{B^0}/τ_{B^+}* , Ph.D. Thesis, Carnegie-Mellon University(1987).

Bh78 V.Bharadwaj et al., *Nucl. Instr. Meth.* **155**, (1978), 411.

Bh84 S.Bhadra, *Inclusive Distributions of Diffractively Produced Neutral Kaons, Lambdas and Anti-Lambdas, and Upper Limits on Λ_c^+ Production in High Energy γp interactions*, Ph.D. thesis, University of Colorado at Boulder, (1984).

Bh85 V.Bharadwaj et al., *Nucl. Instr. Meth.* **228**, (1985), 283.

Bi81 I.I.Bigi, A.I.Sanda, *Nucl. Phys. B193*, (1981), 85.

Bi85 I.Bigi, A.I.Sanda, *Phys. Lett. 171B*, (1985), 320.

Bi86 I.I.Bigi, G. Kopp, P.M. Zerwas *Phys. Lett. 166B*, (1986), 2.

Bi87 I.I.Bigi, *On Charm Decays - Present Status and Future Goals*, preprint SLAC-Pub-4349 (June 1987) to appear in the Proceedings of the Beijing Charm Physics Symposium.

Bj86 J.D.Bjorken, *The Future of Charm and Bottom Physics*, to appear in the Proceedings of the Cinvestav Conference in Mexico City, (1986).

Bj87 J.D.Bjorken,I.Dunietz, *Rephasing-Invariant Parametrizations of Generalised Kobayashi-Maskawa Matrices*, preprint, FERMILAB-Pub-2025 (May 1987) to appear in Physical Review D.

Bo82 A.Bodek et al., *Phys. Lett. 113B*, (1982) 82.

Bu85 H.Burkhardt et al., CERN-EP 85-191 (1985).

Bu86 W.Buchmuller,D.Wyler, *Phys. Lett. 177B*, (1986) 377.

Buc86 W.Buchmuller,D.Wyler, *Nucl. Phys. 268B*, (1986) 621.

Ca80 R.Cahn,H.Harari, *Nucl. Phys. 268B*, (1986) 1135.

Ch83 L.L.Chau, *Phys. Rep. 95*, (1983), 1.

Ch84 D.Christian,J.Slaughter (organizers) et al., *Proceedings of the Conference on Vertex Detectors: Charm and Beauty I*, FNAL (1984).

Co83 E.D. Commins,P.H. Bucksbaum, *Weak Interactions of Leptons and Quarks*, The University of Cambridge Press, (1983).

Cr87 L.Cremaldi, *E-691 Internal Memo on Mass Resolution* (1987).

Cu87 J.R.Cudell, *Experimental Challenges to the Standard Model: A Re-evaluation*, Ph.D. thesis, University of Wisconsin, (1987) MAD-PH-359

Da85 A.Datta, *Phys. Lett. 154B* (1985), 287.

De83 B.Denby, *Inelastic and Elastic Photoproduction of J/ψ (3097)*, Ph.D. thesis, UC Santa Barbara, (1983).

Do86 J.F.Donoghue,E.Golowich,B.R.Holstein,J.Trampetic, *Phys. Rev. D33*, (1986), 179.

Du82 A.Duncan, *Characteristics of Hadronic States in High Energy Diffractive Photoproduction in Hydrogen*, Ph.D. thesis, University of Colorado at Boulder, (1982).

Ea71 W.Eadie,D.Drijard,F.James,M.Roos,B.Sadoulet, *Statistical Methods in Experimental Physics*, North-Holland/American Elsevier, (1971).

Ed85 H.T.Edwards, *Annual Review of Nuclear and Particle Science*, Vol. 35, (1985), 605.

Ei86 E.Eichten,I.Hinchliffe,K.D.Lane,C.Quigg, *Phys. Rev. D*34, (1986) 1547.

Es86 P.Estabrooks, *Aging Effects in a Large Driftchamber in the Fermilab Tagged Photon Spectrometer*, preprint IPP/Ottawa-Carlton, 1986.

Fr79 A.G.Frodesen,O.Skjeggestad,H.Tøfte, *Probability and Statistics in Particle Physics*, Universitetsforlaget, Oslo, 1979.

Ga75 M.K.Gaillard,B.W.Lee,J.L.Rosner, *Rev. Mod. Phys.* 47, (1975), 277.

Gai87 I.Gaines and T.Nash, *Annual Review of Nuclear and Particle Science*, Vol.37, (1987), 177.

Ge84 H.Georgi, *Weak Interactions and Modern Particle Theory*, Benjamin-Cummings, 1984, p. 143.

Gl85 G.Gladding, *Physics in Collision 5: Proceedings*, edited by B.Aubert and L.Montanet, Editions Frontieres, Gif sur Yvette, France (1986).

Gl88 G.Gladding, $D^0 - \overline{D^0}$ Mixing: *The Experimental Situation*, to appear in the Proceedings of the International Symposium on Production and Decay of Heavy of Flavors, Stanford, (1988).

Gl70 S.L.Glashow, J.Iliopoulos, L.Maiani, *Phys.Rev. D*2, (1970), 1285.

Ha84 F.Halzen, A.D. Martin, *Quarks and Leptons: An Introductory Course in Modern Particle Physics*, Wiley (1984).

Ha85 A.Hadeed,B.Holdom, *Phys.Lett.* 159B, (1985) 379.

Hei80 E.H.M.Heijne,P.Jarron et al., *Nucl. Instr. Meth.* 178, (1980), 331.

Hei81 E.Heijne, *Proceedings of a Workshop on Silicon Detectors for High Energy Physics*, FNAL, 1981.

He85 X.G.He,S.Pakvasa, *Phys.Lett* 156B, (1985) 3,4.

Ho85 S.D.Holmes,W. Lee,J.E. Wiss, *High Energy Photoproduction*, Annual Review of Nuclear and Particle Science (1985).

Ja84 P.Jarron,M.Goyot, *Nucl. Instr. Meth.* **226** (1980), 156.

Jo78 L.Jones,H.Wyld, *Phys. Rev. D* **17**, (1978), 759.

Ka85 P.Karchin et.al., *IEEE NS-32*, (1985), 612.

Ke80 J.Kemmer, *Nucl. Instr. Meth.* **169**, (1980) 499.

Ki75 R.L.Kingsley, S.B.Treiman,F.Wilczek,A.Zee, *Phys. Rev. D* **11** (1975), 1919

Ki76 R.L. Kingsley, *Phys. Lett. 63B*, (1976), 3.

Kl86 K.Kleinknecht, *Detectors for Particle Radiation*, Cambridge University Press, Cambridge, (1986).

Kr88 P.Krawczyk,S.Pokorski, *Phys. Rev. Lett.* **60**, (1988), 182.

Ku86 P.F.Kunz, *Nucl. Instr. Meth.* **135**, (1976) 435.

Kum86 B.R.Kumar, *Proceedings of the Workshop on Vertex Detectors: State of the Art and Perspectives*, Erice, Italy, September 1986.

Lo86 W.C.Louis et al., *Phys. Rev. Lett.* **56**, 1027 (1986).

Me86 S.Menary, *A Study of Transverse Momentum Distributions of Photoproduced Charged and Neutral D-mesons*, Master's Thesis, University of Toronto, (1986).

Na86 T.Nash et al., *Proceedings of the XXIII Int'l Conference on High Energy Physics*, Berkeley CA, (1986).

Pu85 M.Purohit, *E-691 Internal Memo on the E_T trigger* (1985).

Or82 J.Orear, *Notes on Statistics for Physicists (revised)*, (1982), preprint FNAL-48924.

Or87 M.Oregalia, *Production of Same-Sign Dimuons by 0-800 GeV Neutrinos and AntiNeutrinos*, Proceedings of the Salt Lake City Meeting, Salt Lake City, Utah, 1987.

Ra87 J.R.Raab, *Lifetime Measurements of the Three Charmed Pseudoscalar D-Mesons*, Ph.D. thesis, University of California at Santa Barbara, 1987.

Ra88 J.R.Raab et al., *Measurement of the D^0 , D^+ , and D_s Lifetimes*, preprint Fermilab-Pub-87-144,to appear in Physical Review D.

Ri86 G.de Rijk, *Lifetime Measurements of Charmed Mesons with High Resolution Silicon Detectors*, Ph.D. thesis, University of Amsterdam, 1986.

Re86 S.Reucroft, *Charm Hadroproduction*, Proceedings of the 6th International Conference on Physics in Collision, Chicago (1986), (World Scientific).

So86 M.Sokoloff et al., *Phys. Rev. Lett.* 57, (1986), 3003.

Sa76 J.R.Sanford, *Annual Review of Nuclear Science*, Vol.26, (1976), 151.

Su84 D.J.Summers, *A Study of the Decay $D^0 \rightarrow K^-\pi^+\pi^0$ in High Energy Photoproduction*, Ph.D. thesis, UC Santa Barbara, (1984).

Su85 D.J.Summers, *Nucl. Instr. Meth.* 228, (1985), 290.

Ta76 H.Taureg et al., *Phys. Lett.* 65B, (1976), 92.

Ts74 Y.Tsai, *Rev. Mod. Phys.* 46, (1974), 815.
Errata, *Rev. Mod. Phys.* 49, (1977), 421.

Wo85 L.Wolfenstein, *Phys. Lett.* 164B, 170 (1985).

Ya85 H.Yamamoto et al., *Phys. Rev. Lett.* 54, 522 (1985).

Yam85 H.Yamamoto, *D Meson Production in e^+e^- Annihilation at 29 GeV Center of Mass Energy*, Ph. D. thesis, California Institute of Technology, 1985.

Yu60 L.C.L. Yuan, *Proceedings of the International Conference on Instrumentation for High Energy Physics*, Berkeley, CA.(1960) p.177 .